

Ginzburg-Landau theory of complex spherical packing
phases in soft condensed matter

Ginzburg-Landau theory of complex spherical packing phases in soft condensed matter

Sarah Dawson, B. Sc. (Honours)

A Thesis Submitted to the School of Graduate Studies in Partial Fulfillment of the Requirements
for the Degree of Doctorate of Science

McMaster University

McMaster University

Ph.D. Science (2021)

Hamilton, Ontario (Physics & Astronomy)

TITLE: Ginzburg-Landau theory of complex spherical packing
phases in soft condensed matter

AUTHOR: Sarah Dawson

SUPERVISOR: Dr. An-Chang Shi

NUMBER OF PAGES: vii, 1000

Lay Abstract

Soft condensed matter physics is the study of soft, deformable materials, such as soap bubbles, foams, and plastics. Many different soft matter systems undergo a fascinating phenomenon known as self-assembly, wherein the constituent particles spontaneously arrange themselves to form various ordered structures. In particular, the spherical packing phases appear when the particles first cluster into spherical aggregates, which then pack into larger arrangements. This sort of self-assembly is interesting because many different spherical arrangements are observed, including the complex spherical packing phases (also known as the Frank-Kasper phases). The fact that these complex phases appear in many different types of materials is not well understood. In this thesis we use a model known as the Ginzburg-Landau theory to ask which of these arrangements will form in a given system, and why. We uncover generic features of the Ginzburg-Landau theory that control which spherical packing phases appear, and we connect these features to several specific systems. These results provide insight into the mechanisms behind the formation of the complex spherical packing phases in a diverse range of systems.

Abstract

Stable Frank-Kasper spherical packing phases have been observed in a wide variety of soft-condensed matter systems, but the universality of these phases is not well understood. Recently, it was shown that the Frank-Kasper σ and A15 phases are stable in the well-known Landau-Brazovskii (LB) model. In this work we consider the σ and A15 phases, as well as the Laves C14 and C15 phases, and show that none of these is stable in the Ohta-Kawasaki (OK) model, which is another widely studied Ginzburg-Landau theory. The LB and OK models differ only in their quadratic coefficients. We conduct a thorough investigation of the role that this coefficient plays in stabilizing the complex phases. We uncover generic principles linking the functional form of the coefficient in reciprocal space with the stability of the complex phases. A Ginzburg-Landau theory for a diblock copolymer system with a conformational asymmetry parameter is derived, but the complex phases are not found to be stable in this model. We also consider a Ginzburg-Landau theory for a system of hard spheres interacting via a pairwise short-range attractive, long-range repulsive (SALR) potential, and use our framework to demonstrate how the parameters in the potential influence the stability of the Frank-Kasper phases. Taken together, these results provide insight into the universal mechanisms that underlie the formation of the complex spherical packing phases in soft condensed matter.

Acknowledgements

First I need to thank my supervisor, Dr. An-Chang Shi, for all of the support that you have provided me with during the six years we have worked together. I have benefited immensely from your knowledge and also your patience and compassion. Completing a PhD is never an easy task, and I could not have done it without you. I also want to thank the other students in the group (current and former), Duncan McClenegan, Tom Lai, Jiayu Xie, and Cameron Burns, my collaborator Kai Jiang, and my committee members, Dr. Kari Dalnoki-Veress and Dr. Sung-Sik Lee, for your valuable insights into the work as I was completing it. This input made the project what it is, and also made the process much more enjoyable!

Lastly I want to thank my friends and family, especially Carmen, Anton, my Mum and Dad, Beth, Kat, Leslie, Nick, and my partner James, for all your patience, love and emotional support through this process, and for letting me talk at you about physics for all these years. You're the best!

Declaration of Academic Achievement

All of the phase diagrams in this work except for those in the Introduction and those in figure 4.14 are the results of calculations conducted by me. The phase diagrams in figure 4.14 was constructed by Jiayu Xie and Cameron Burns. The derivation of the modified Leibler theory was done by me, following the procedure developed by Leibler, as indicated in the text. The rest of the analysis is also mine. The thesis was written entirely by me. Dr. An-Chang Shi, Jiayu Xie, and Cameron Burns assisted with editing the manuscript. My colleague Duncan McClenegan provided early consultation on the Ohta-Kawasaki calculation, and Kai Jiang provided numerical verification of the final Ohta-Kawasaki phase diagram. Dr. Shi provided much input into the analysis.

Contents

1	Introduction	1
1.1	What is soft condensed matter?	1
1.2	Spherical packing phases	2
1.2.1	Hard sphere packing	2
1.2.2	The Frank-Kasper phases	5
1.2.3	Soft sphere packing	6
1.2.4	Spherical packing phases in soft condensed matter	8
1.2.5	Spherical packing phases in diblock copolymers	8
1.3	Ginzburg-Landau theory	11
1.3.1	Frank-Kasper phases in the Landau-Brazovskii model	13
1.4	Density functional theory of spherical packing phases	15
1.5	The organization of this thesis	16
2	Generic Landau theory	17

2.1	Form of the free energy functional	18
2.2	Ohta-Kawasaki and piecewise models	21
2.3	Modified Leibler theory	22
2.4	SALR potential theories	26
2.4.1	The double-Gaussian potential	27
2.4.2	The step potential	29
3	Numerical methods	32
3.1	Phase optimization	33
3.1.1	Initialization	34
3.1.2	Free energy optimization	37
3.1.3	Unit cell optimization	38
3.2	Constructing phase diagrams	39
4	Results and discussion	43
4.1	The Ohta-Kawasaki model	43
4.2	The piecewise interpolation model	45
4.2.1	Effect of the long wavelength modes	45
4.2.2	Effect of the short wavelength modes	50
4.3	Modified Leibler theory	56
4.4	The SALR potentials	57

4.4.1	The double-Gaussian potential	58
4.4.2	The step potential	60
4.4.3	DFT results	62
5	Conclusion	65
A	Modified Leibler theory	68
A.1	Series expansion of the free energy functional	68
A.2	Ideal chain correlation functions	72
A.3	Random phase approximation	77
B	Numerical details	80
B.1	Initializations	80
B.1.1	Spherical phases	80
B.2	Field optimization algorithm	87
B.3	Unit cell optimization algorithm	89

Chapter 1

Introduction

1.1 What is soft condensed matter?

Soft condensed matter (or soft matter) refers broadly to a class of materials that can be mechanically or structurally deformed by thermal fluctuations or external forces – in other words, materials that are soft. Some examples are polymers, surfactants, colloids, and liquid crystals. In his beginner-friendly text on the subject, *Soft Condensed Matter* [1], R. A. L. Jones lists three common features of these materials. The first is the importance of the so-called *mesoscopic* molecular length scales, which range from 1 nm to 1 μm . The molecules that make up soft matter are much larger than their constituent atoms, meaning they are well described by coarse grained models. This results in *universality*; similar phenomena appear across multiple systems even though they appear very different from a molecular standpoint. The softness is also a consequence of particle size. Daan Frenkel makes a rough argument for this using dimensional analysis [2]. Consider that the elastic modulus has units of [energy/volume]. The energetic interactions between soft matter particles are weaker than those between atoms, and the length scales are 10 to 100 times larger, meaning the particles are at least 10^3 to 10^6 times *softer* than atomic or hard condensed matter systems. The second important feature that Jones lists is the relevance of thermal fluctuations and Brownian motion. By setting the upper limit of the length scales to $\sim 1\mu\text{m}$, we ensure

that the soft matter systems are well described by statistical mechanics. Together with the softness this means that thermal fluctuations are sufficient to deform the system, so we should visualize soft matter as being in a state of constant flux. The final important feature is the phenomenon of *equilibrium self-assembly*. This refers to the spontaneous formation of equilibrium ordered structures. The same or similar self-assembled patterns appear in a wide variety of soft matter systems [3]. Understanding and guiding the formation of self-assembled structures is an active research area of soft condensed matter physics.

1.2 Spherical packing phases

The current work concerns a subset of the possible self-assembled structures that appear when the molecules in a material are driven to form spherical assemblies such as micelles. Under correct conditions these micelles will form dense arrangements referred to as the *spherical packing phases*. As we will soon discuss, these phases are very common in soft matter. They appear in block copolymers, surfactants, liquid crystals, colloidal solutions, and many other systems. There are many different spherical packing phases associated with the different possible arrangements of these micelles, which mimic the structures observed in hard condensed matter [4, 5]. Our objective is to understand the principles governing the formation of these phases and determining which packing will be favoured for a given system.

1.2.1 Hard sphere packing

In order to understand the complexity of this problem it is informative to first consider the packing of hard, non-interacting spheres. For identical hard spheres the largest possible *periodic* packing fraction (the fraction of available volume that is occupied by the spheres) is $\pi/(3\sqrt{2}) \approx 0.74$. This was proved by Carl Friedrich Gauss in 1831 [6]. It is the packing fraction achieved by both the face-centered cubic (fcc also known as cubic close packed) and hexagonally close packed (hcp) arrangements. Both of these arrangements are made up of stacked layers of spheres arranged in hexagonal close packed configurations, and differ only in the alignments of successive layers, as illustrated in figure 1.1.

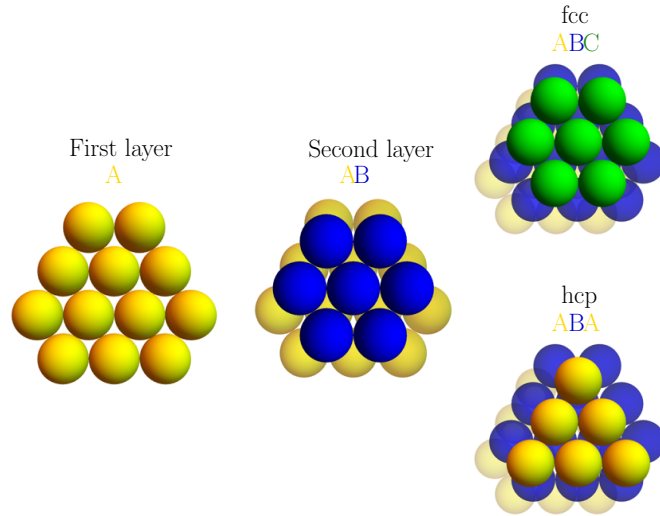


Figure 1.1: Illustration of how the fcc and hcp arrangements are constructed from successive layers of hexagonally close packed spheres.

The statement that this is the largest possible packing fraction among *all* possible arrangements of uniform spheres (including random packings) came to be known as the Kepler conjecture after it was proposed by Johannes Kepler in a 1611 paper titled “On the six-cornered snowflake” [7]. Though it may seem intuitive, the Kepler conjecture was not proven until 1998 when Thomas Hales conducted a proof by exhaustion, which involved numerically checking a sufficiently large number of cases [8]. Numerical calculations show the maximum packing fraction that can be obtained by randomly close-packed (rcp) spheres is approximately 0.64 [9].

In the 1950s and 60s statistical physicists were interested in the following question: will a system of hard spheres spontaneously order? It is clear from purely geometric considerations that they must if the packing fraction is above the 0.64 threshold for random packing, but could this transition occur at lower packing fractions? In one anecdote, the physicist George Uhlenbeck posed this question at a symposium on many body physics in 1959 in Hoboken New Jersey. He told the audience that he had held the question to a vote at a discussion in Seattle and that the final count was tied. The same vote in Hoboken once again ended in a tie [10]. To understand why his question caused such disagreement, consider a system

of uniform hard spheres with diameter σ . The interaction energy between any pair of such spheres is given as a function of the separation distance between their centres, r , by

$$u(r) = \begin{cases} \infty & r < \sigma \\ 0 & r > \sigma \end{cases} . \quad (1.1)$$

The equilibrium state will be the one that minimizes the Helmholtz free-energy:

$$F = E - TS \quad (1.2)$$

where E is the internal energy, S is the entropy, and T is the temperature. Equation (1.1) tells us that all allowed microstates of this system have the same energy and thus the equilibrium phase will be the one that maximizes entropy, regardless of the temperature. We often think of the order-disorder phase transition as energy-driven; the lost of translational entropy in the ordered state is offset by a decrease in energy of the system at sufficiently low temperatures. That cannot occur here. Can a transition to the apparently more ordered periodic structure be driven entirely by the principle of maximum entropy? Monte Carlo simulations done by Alder and Wainwright [11] and by Wood and Jacobson [12] in 1957 showed that a system of hard spheres would undergo a phase transition to a close-packed (fcc or hcp) structure when the volume fraction of spheres was increased above a fraction of ~ 0.49 , well below the packing density of rcp spheres. The experimental verification was more challenging to obtain, owing to the difficulty in producing non-interacting spherical particles of uniform radius. The ordering of hard spheres was observed experimentally by Pusey and Van Meegen in 1986 for a system of colloidal particles with a very short-ranged repulsive interaction [13]. Additionally, detailed numerical calculations by Bolhuis et. al. showed that the fcc phase is actually slightly favoured over the hcp phase at room temperature, with an energy difference of only $10^{-3}k_B T$ per mol [14].

So how is this possible? The argument requires us to accept that our intuitive notion of randomness does not always correspond to the maximal entropy. When hard spheres order the loss of long-range translational entropy is offset by some gain in local configurational entropy. Each sphere has more space to explore when it maintains equal distance from each of its neighbours, a situation which corresponds to a regular packing arrangement. See articles by Bruce Ackerson [15] and Daan Frenkel [16] for a more detailed intuitive explanation of entropy driven ordering in hard spheres.

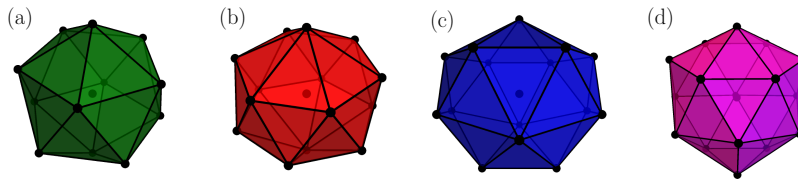


Figure 1.2: The four Frank-Kasper polyhedra, (a) CN12 (the icosahedron), (b) CN14, (c) CN15, and (d) CN16

1.2.2 The Frank-Kasper phases

We have seen that a system of uniform spheres will order into the close-packed fcc phase when their volume fraction is sufficiently large. As it turns out, the hard sphere model is a good description of atomic metals. The atoms in a metal will crystallize into structures that maximize electron density by finding configurations with the largest packing fraction. This can be achieved via structures with a coordination number (CN) of 12, where coordination number refers to the number of nearest neighbour atoms at each lattice site. There are three possible structures that can be formed with CN12: the fcc and hcp structures and the tetrahedron. In a paper published in 1952 [17], Sir F. C. Frank demonstrated that a collection of 13 atoms interacting via a simple Lennard-Jones pair potential has a free-energy minimum when arranged in the icosahedral configuration. He argued that this was due to the tetrahedral interstitial spaces of this shape. In atomic metal such as copper or iron, however, only the fcc and hcp phases appear because these are *space filling* crystal structures. Icosahedra alone cannot be packed together to fill space without gaps. However when we ease the requirement that the spheres have uniform size, as we must if we wish to consider metallic alloys, then the optimal spherical packing arrangement becomes more complex. In a pair of papers published in 1958 and 1959 Frank and Kasper described how the icosahedral configuration could be incorporated into a space filling crystal lattice when paired with three other tetrahedra known as the Frank-Kasper polyhedra [18, 19]. As previously stated the icosahedron has coordination number 12 (CN12). The three other polyhedra Frank and Kasper used are made up of spheres of slightly different sizes, and have coordination numbers 14 (CN14), 15 (CN15), and 16 (CN16). The four Frank-Kasper polyhedra are shown in figure 1.2.

Because the Frank-Kasper phases are close-packed structures, they were predicted to be the most energetically favourable way for spheres to pack when size differences between the spheres were present. At least 20 different Frank-Kasper phases have been observed in metal alloys [20]. In this work we are particularly interested in the σ , A15, C14 and C15 phases which, as we will see, are the most relevant for soft condensed matter systems. The unit cells for these four phases are shown in figure 1.3. These phases are sometimes referred to as the *complex spherical packing phases* due to their larger unit cells. We use the terms Frank-Kasper phase and complex phase interchangeably throughout this thesis. A detailed description of the Frank-Kasper crystal structures can be found in Marc De Graef and Michael E. McHenry's text [21].

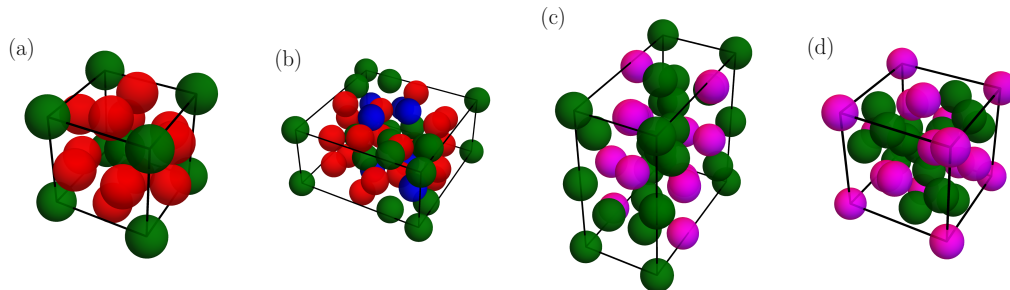


Figure 1.3: Unit cells for four different Frank-Kasper phases, (a) the A15 phase, (b) the σ phase, (c) the C14 phase, and (d) the C15 phase. Sphere colours indicate which of the polyhedra depicted in figure 1.2 sits at each site.

1.2.3 Soft sphere packing

We must now contend with the fact that soft matter micelles are, by their very definition, not hard spheres. To understand the packing behaviour of soft spheres we next consider the other extreme case, when the spheres are so soft that there is *no* free-energy cost to deform them. In this case the problem becomes one of minimizing the area of contact. We might imagine that we are dealing with something like a collection of soap bubbles arranged into a foam. After the last section the reader should not be surprised to learn that figuring out the optimal way to arrange soap bubbles of equal volume into a lattice structure is not trivial. This problem was notably studied in the 1800s by Joseph Plateau [22] and by Lord

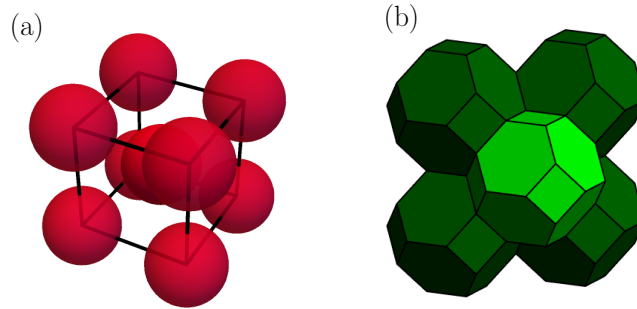


Figure 1.4: (a) Unit cell and (b) Voronoi cell shapes for body-centred cubic (bcc) lattice.

Kelvin [23], who hypothesized that a foam with no gas in the interstitial sites could have zero modulus and thus might be an interesting mechanical model for the ether through which light was then thought to propagate. To describe the crystal structures formed by foams, we should introduce the concept of a Voronoi cell. For a given set of points, the Voronoi cells are the volumes associated with each point that are constructed by taking the loci of points in the space that are closer to the point of interest than to any other point in the original set. The spherical bubbles in an ideal foam are deformed to fill space and their final, distorted shapes are Voronoi cells for an underlying lattice structure. Lord Kelvin proposed that the optimal packing for such soft spheres was one in which the bubbles deformed into a shape he called the tetrakaidecahedron, and which then packed into a body-centred cubic (bcc) lattice. A single unit cell for the bcc lattice is shown in figure 1.4 (a), together corresponding shapes of the deformed bubbles, (b).

The bcc structure was the best-known solution to the Kelvin problem until 1993 when Denis Weaire and Robert Phelan discovered a more efficient solution, now known as the Weaire-Phelan structure [24]. This structure is made up of two different polyhedral Voronoi cells with the same volume, packed into a lattice that has the Frank-Kasper A15 symmetry. The A15 unit cell is shown in figure 1.3 (a). The Weaire-Phelan structure is the current best-known solution to the Kelvin problem, but there is still no proof that it is optimal.

1.2.4 Spherical packing phases in soft condensed matter

Having considered the two extreme cases, we return now to the original problem: the packing of soft spherical micelles. Here the physics is governed by space filling constraints and surface area minimization just like the spherical bubbles of the Kelvin problem. However, unlike soap bubbles, these spheres have non-zero elastic moduli and so they resist deformation. In the limit of very large elastic moduli we recover the hard sphere case. The tension between the need to fill space and the resistance to deformation leads to the complexity of spherical packing phases observed in soft matter systems. These systems are *frustrated*, with competing effects leading to phase diagrams that are both highly diverse and extremely sensitive to fine tuning. The Frank-Kasper spherical packing phases appear in many soft matter systems as a consequence of this frustration. Experimentalists have observed the σ and A15 phases in liquid crystalline dendrimers [25, 26] and in linear tetrablock copolymer melts [27, 28], the σ , C14 and C15 phases in diblock copolymer melts [29, 30, 31], the A15 phase in linear dendron block copolymer melts [32] and amphiphilic nanotetrahedral surfactants [33, 34], the C14 phase in monodisperse functionalized nanoparticles [35], and the σ , A15, C14 and C15 phases in concentrated ionic surfactants [36, 37], to name a few.

1.2.5 Spherical packing phases in diblock copolymers

The phase behaviour of block copolymers has been studied in detail. They provide a good illustration of how the competition between factors in the packing of soft spheres can lead to the formation of the Frank-Kasper phases [38]. Block copolymers are heterogeneous polymers created by bonding two or more chemically distinct sub-chains together. This chain architecture results in a system where frustration emerges between chain connectivity effects that favour mixing of the different species and enthalpic effects that prefer phase separation. Block copolymer structures can be fine-tuned to enable a wide range of phase behaviours [39, 29]. A recent overview by Dorfman discusses many of the mechanisms known to stabilize the complex phases in block copolymers [40]. Here we will discuss the simplest example, the diblock copolymer, which is made of two polymers joined together as illustrated in figure 1.5 (a). The immiscibility of the two species causes micelles to form at low temperatures in order to reduce the contact between chains of unlike species, see

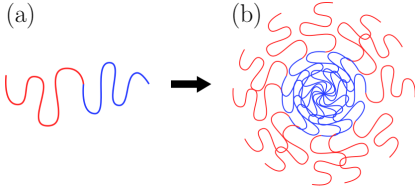


Figure 1.5: (a) Diblock copolymer molecules are composed of two unlike chains (red and blue) that are bonded together. The immiscibility of the chains causes them to phase separate. Depending on the geometry of the chain this process may result in the formation of a spherical micelle, like the one shown in (b).

figure 1.5 (b). We visualize the spherical micelle formed in a diblock melt as consisting of an inner core and an outer corona, The balance between entropic and enthalpic effects that stabilizes complex phases in diblock systems is illustrated by a model called the diblock foam model (DFM), first described by Milner and Olmstead [41, 42]. In this model, packed micelles are assumed to deform in order to fill space, much like the bubbles described in the Kelvin problem. The resulting shapes are called quasi-spherical domains (qSD). It is further assumed that the inner core of the micelles is deformed so that it forms an affinely shrunk copy of the Voronoi cell shape. This is illustrated in figure 1.6, which is reproduced from [5]. Unlike in the Kelvin problem there is a free energy cost to this deformation. The immiscibility of the chains means there is also a cost associated with the surface of contact between the core and the corona. In the DFM these free energies are taken to be functions of the geometry of the Voronoi cells. This geometrical interpretation can help us see how the complex phases appear in systems with physics that is partway between the soft and hard sphere models described in previous sections. For illustration purposes we will sketch the arguments of the DFM here, following reference [5].

To compute the free-energy we begin by choosing a particular lattice packing, \mathcal{X} , that is required to be space filling. \mathcal{X} consists of a collection of Voronoi cells (for example, a set of Frank-Kasper polyhedra) that can be tiled to create a space-filling lattice. The free-energy per chain, f , for a given choice of \mathcal{X} is:

$$f(\mathcal{X}) = \gamma \frac{\mathcal{A}(\mathcal{X})}{R_0} + \frac{\kappa}{2} \mathcal{I}(\mathcal{X}) R_0^2. \quad (1.3)$$

Here R_0 is the radius of a sphere which has volume equal to the mean volume of the Voronoi

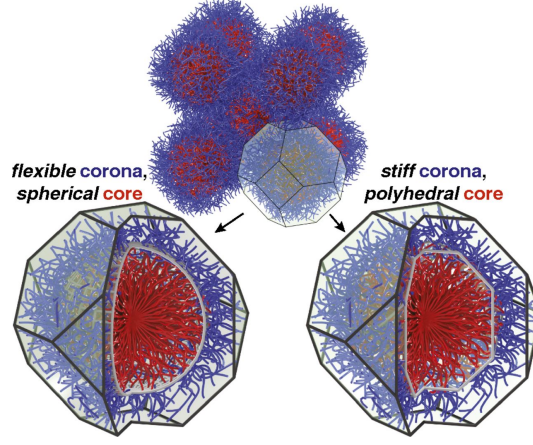


Figure 1.6: Illustration of how the core shape may differ from the shape of the Voronoi cell. The sphere on the left corresponds to the case when the corona polymer is stretched, the sphere on the right to when the core is stretched. The DFM assumes the latter. Figure reproduced from reference [5].

cells in \mathcal{X} , i.e.,

$$\frac{4}{3}\pi R_0^3 = \frac{1}{N_{\mathcal{X}}} \sum_i v_i, \quad (1.4)$$

where the sum is over all cells in \mathcal{X} , v_i is the volume of the i^{th} cell, and $N_{\mathcal{X}}$ is the number of cells. The first term in equation (1.3) measures the unfavourable interaction energy between the core of each micelle and its corona. The coefficient γ is positive and measures the immiscibility of the two components, it can be thought of as a sort of surface tension. $\mathcal{A}(\mathcal{X})$ is the dimensionless ratio between the average interfacial area per chain and the area of a perfectly spherical micelle with radius R_0 :

$$\mathcal{A}(\mathcal{X}) = \frac{N_{\mathcal{X}}^{-1} \sum_i a_i}{4\pi R_0^2}, \quad (1.5)$$

where again the sum is over all cells in \mathcal{X} and A_i is the area per chain in the i^{th} cell. If it were possible to construct a space filling set of perfectly spherical Voronoi cells, we would find $\mathcal{A}(\mathcal{X}) = 1$. This term is minimized when the core-corona interface is small, and so drives the system to favour Voronoi cells with high sphericity.

The second term in (1.3) is a measure of the entropic cost of stretching the chains inside the core. κ is a measure of the chain stiffness and \mathcal{I} is a dimensionless stretching moment:

$$\mathcal{I}(\mathcal{X}) = \frac{N_{\mathcal{X}}^{-1} \sum_i I_i}{\frac{4}{5}\pi R_0^5}, \quad (1.6)$$

where I_i is the second moment of the i^{th} Voronoi cell, which is centred at \mathbf{x}_i :

$$I_i = \int_{V_i} d\mathbf{x} |\mathbf{x} - \mathbf{x}_i|^2. \quad (1.7)$$

The free energy in (1.3) can be computed for each candidate lattice structure \mathcal{X} , and it can be supposed that the structure which minimizes $f(\mathcal{X})$ is preferred. The model was used by Milner and Olmstead to demonstrate that the Frank-Kasper A15 phase can be favoured over the fcc and bcc phases [42]. In their paper [5], Reddy et. al. relax the requirement that the cells have equal volume and use the DFM to analyse 11 Frank-Kasper phases, as well as the bcc and fcc phases. The authors find that the DFM predicts the Frank-Kasper σ phase as the stable phase of the system for diblock copolymers formed from two highly *asymmetric* species, consistent with results from experiment and self-consistent field theory (SCFT). The model also accurately describes the relative free energies of the complex phases when compared with the results from a SCFT calculation of the same system [43, 30]. We can therefore trust that this is a useful intuitive picture of the factors governing the formation of FK phases in diblock copolymers. The frustration that arises between the space-filling constraint and the resistance to deformation is likely also at play in other systems of soft spheres.

We now have a picture of micelles as intermediate between hard and soft spheres. We also have a description of how this intermediate behaviour leads to the appearance of the Frank-Kasper phases. Beyond providing us with some good intuition, however, the DFM cannot be extended to other soft matter systems where the complex phases are known to be stable.

1.3 Ginzburg-Landau theory

In the previous section we saw how the formation and relative stability of the spherical packing phases is described in various systems of spheres, and we presented a detailed discussion of the interplay between factors that leads to the stability of the Frank-Kasper phases in diblock copolymer systems. We now remind the reader of the fact that the complex phases appear in a wider range of systems. The ubiquity of these phases indicates that some more general mechanisms must be at play. Ginzburg-Landau (GL) theories provide us with

a framework to understand the phase behaviour of self-assembled systems in a generic way.

Lev Landau first developed his general theory of phase transitions in a pair of papers published in 1937 [44, 45]. Landau theory relies on the choice of an *order parameter*, ϕ , to capture the phase behaviour of the system. The order parameter must satisfy the condition that $\phi = 0$ in the high symmetry (disordered) phase and is small but non zero in the ordered phase close to the transition point. If ϕ is chosen so that it doesn't become too large in the low symmetry (ordered) phase, then we can expand the free-energy of the system as a polynomial function of ϕ . Only terms that reflect the symmetry of the underlying Hamiltonian are included in this expansion. Thus Landau theory allows us to understand universality classes of phase transitions – close to the transition point the nature of the transition is determined by the symmetry of the system rather than any particular atomic or molecular interactions. In order to describe crystallization it is necessary to consider a spatially varying order parameter $\phi(\mathbf{x})$ that satisfies $\phi(\mathbf{x}) = 0$ everywhere in the disordered state. The generalization of the Landau theory to an order parameter field is known as the Ginzburg-Landau theory. Notable early work in the use of a GL theory to study the formation of ordered phases was done by Brazovskii [46] and by Alexander and McTague [47]. Papers by Leibler [48], Friedrickson and Helfand [49], and Ohta and Kawasaki [50] developed theories that connected the polynomial coefficients with molecular parameters of diblock copolymers. E. I. Katz et. al. [51] developed the theory for liquid crystal systems. GL theory has also been used to describe the phase behaviour of colloidal systems [52]. Seul and Andelman [3] worked on the use of GL theory to describe the formation of ordered phases in a generic system where competing interactions pick out a particular length scale. Though the theory has been used extensively to study self assembly, the Frank Kasper phases were largely ignored until the thesis work by Duncan McClenegan, supervised by Dr. An-Chang Shi [53], which will be discussed in some detail in the next section.

The GL theories considered in this work all have the following form,

$$F[\phi] = F_{local}[\phi] + F_{nl}[\phi], \quad (1.8)$$

where ϕ is an appropriate order parameter field. The local part is given by a quartic polynomial:

$$F_{local}[\phi] = \int d\mathbf{x} \left\{ \frac{\tau}{2} \phi(\mathbf{x})^2 - \frac{\gamma}{3!} \phi(\mathbf{x})^3 + \frac{1}{4!} \phi(\mathbf{x})^4 \right\}, \quad (1.9)$$

where τ and γ are constants. It is significant that a cubic term appears in this theory; the presence of this term means that the phase transitions will be first order. The non-local term in equation (1.8) is a quadratic functional,

$$F_{nl}[\phi] = \frac{1}{2} \int \frac{d\mathbf{q}}{(2\pi)^3} \Gamma(q) \tilde{\phi}(\mathbf{q}) \tilde{\phi}(-\mathbf{q}). \quad (1.10)$$

Here $\tilde{\phi}(\mathbf{q})$ is the Fourier transform of $\phi(\mathbf{x})$:

$$\tilde{\phi}(\mathbf{q}) = \int d\mathbf{x} \phi(\mathbf{x}) e^{-i\mathbf{q}\cdot\mathbf{x}}. \quad (1.11)$$

The formation of periodic ordered phases in these models is due to the coefficient $\Gamma(q)$. We assume that $\Gamma(q)$ has at least one minimum at some finite, non-zero q , and the theory is scaled so that this minimum occurs at $q = 1$. This means that equation (1.8) is minimized by order parameters that have density modulations with wavevectors $|\mathbf{q}| = 1$. As noted by Alexander and McTague [47] and others, the set of vectors with $|\mathbf{q}| = 1$ forms a spherical shell in reciprocal space so there are multiple periodic phases that minimize F_{nl} . We may also see the solutions with additional non-zero modes, $|\mathbf{q}| \neq 1$, provided these offer a sufficient decrease in the local part of the free energy.

1.3.1 Frank-Kasper phases in the Landau-Brazovskii model

As was mentioned above, the question of whether the Frank-Kasper phases might be stable in a GL theory was investigated by McClenegan and Shi [53]. In that work the authors considered a particular form of equation (1.8) known as the Landau-Brazovskii (LB) model [46]. The free energy of this model is given by:

$$F_{LB}[\phi] = \int d\mathbf{x}' \left\{ \frac{\xi^2}{8q_0^2} (\nabla^2 \phi' - q_0^2 \phi')^2 + \frac{\tau'}{2} \phi'(\mathbf{x})^2 - \frac{\gamma'}{3!} \phi'(\mathbf{x})^3 + \frac{u}{4!} \phi'(\mathbf{x})^4 \right\}. \quad (1.12)$$

Here $2\pi/q_0$ is the principal length scale of the theory and ξ^2 , τ' , γ' and u' are all constants. The authors showed that the free energy can be rescaled to match equation (1.8) with,

$$\Gamma_{LB}(q) = \frac{1}{2} (q^2 - 1)^2. \quad (1.13)$$

Their work showed that the Frank-Kasper σ and A15 phases were stable in the LB model in a region between the bcc and fcc phases. The phase diagram shown in figure 1.7 is a reconstruction of the one computed in that work. Minor differences are the result of a different numerical algorithm.

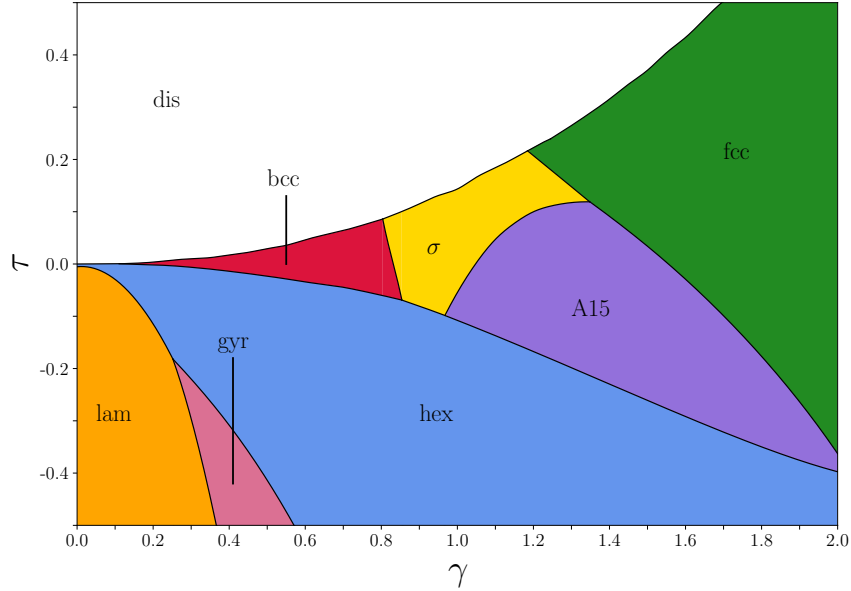


Figure 1.7: Phase diagram for the Landau-Brazovskii model, showing stable regions for the Frank Kasper σ and A15 phases. This diagram closely matches the one constructed by McClenegan and Shi [53].

The LB free energy functional appears frequently in discussions of self-assembly in the GL theory. Any quadratic coefficient $\Gamma(q)$ that depends on the square of the wavevector, q^2 , and has a minimum at $q_0 \neq 0$ can be approximated to quadratic order by the LB model:

$$\Gamma(q_0^2) \approx \frac{1}{2} \Gamma''(q_0^2) (q^2 - q_0^2)^2. \quad (1.14)$$

If we suppose that only those wavevectors close to q_0 contribute to the free energy then this should be a good approximation. Thus the quadratic term in a GL theory is often *assumed* to have the form of equation (1.13). The ubiquity of the LB model underscores the importance of McClenegan’s result; their updated phase diagram has consequences for any work that models the formation of ordered phases using a GL theory. It also raises several new questions: do the complex phases still appear if we change the form of $\Gamma(q)$? If not, then what factors control their stability? Lastly, what does this mean for any work that uses the GL theory to approximate the free-energy functional of a soft matter system? These questions are the focus of this work.

1.4 Density functional theory of spherical packing phases

We will now mention another theoretical framework that has been used to study self-assembly of soft condensed matter, the density functional theory (DFT). In particular we are interested in the use of DFT to study the formation of ordered phases in a system of hard-core spherical particles that interact via a short-range attractive, long-range repulsive (SALR) potential (sometimes also called a mermaid potential because of its attractive head and repulsive tail). Such potentials can be realized experimentally and with a high degree of control in colloid polymer mixtures [54, 55, 56, 57]. This makes them an exciting focus for theoretical work. DFT calculations reveal that a range of ordered phases are stable in SALR systems. In particular we highlight the work of Davide Pini and Alberto Parola [58], whose phase diagram is reprinted here in figure 1.8, and of Yuan Zhuang and Patrick Charbonneau [59]. Both authors detected the bcc and hcp spherical packing phases in their respective models.

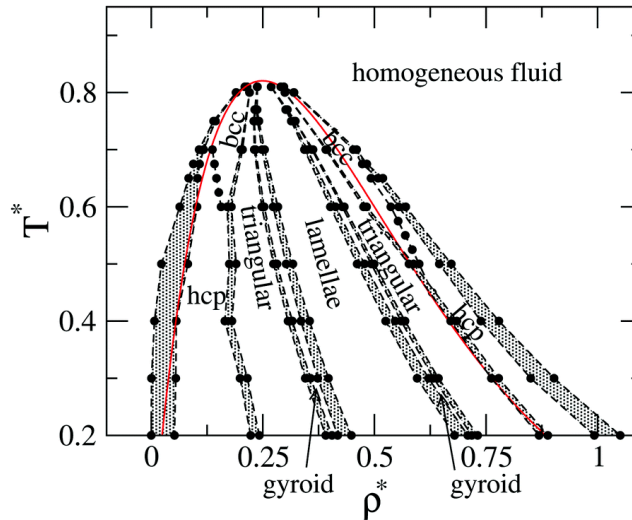


Figure 1.8: Phase diagram computed by D. Pini and A. Parola for a SALR potential using the DFT. Reprinted from [58]. The authors discovered regions of stability of the hcp and bcc spherical packing phases in the model that they considered.

The appearance of the bcc and hcp phases means that the SALR models are interesting candidates for the appearance of complex phases. No one had investigated the stability of

any of the complex phases in an SALR system until quite recently when our collaborators Jiayu Xie and Cameron Burns did a calculation that detected the Frank-Kasper σ and A15 phases [60]. Those results are highly relevant to our work. They will be discussed in more detail in chapter 4 where they can be compared with the main conclusions of this thesis.

1.5 The organization of this thesis

We have seen that the Frank-Kasper phases appear in many soft condensed matter systems. Their formation is a consequence of the packing of soft spherical assemblies. In section 1.3.1 we highlighted a result showing that the complex phases are stable in the Landau-Brazovskii model. The remainder of this work is dedicated to investigating the stability of the complex phases in other Ginzburg-Landau theories. The thesis is structured as follows. In chapter 2 we will describe in detail the Ginzburg-Landau theories considered in this work. The numerical methods we used to obtain our results will be explained in chapter 3. Chapter 4 contains a description and discussion of the results obtained. Chapter 5 gives a summary and contextualization of the work.

Chapter 2

Generic Landau theory

In chapter 1 we described the context for this research and introduced the generic form of the free energy functionals used in this work, equations (1.8), (1.9), and (1.10). In the first part of this chapter we will explain this expression. We will then present the specific theories that are analysed in later chapters. In section 2.2 we discuss the Ginzburg-Landau theory that was created by T. Ohta and K. Kawasaki in 1986 [50], and which is known as the Ohta-Kawasaki (OK) model. Like the Landau-Brazovskii (LB) model, it is widely used to describe the formation of ordered phases. We also create a model that interpolates between the LB and OK models, which we will use later to understand the difference between their respective phase behaviours. In section 2.3 we discuss the theory that was first derived by Ludwik Leibler in 1980 [48], which we will refer to as the Leibler model throughout this work. We rederive the Leibler model with a modification that is expected to influence the stability of the complex phases, and we refer to this result as the modified Leibler (ML) model. In the final section, 2.4, we discuss how a Ginzburg-Landau theory can be derived from DFT models with SALR potentials, and present a couple examples.

2.1 Form of the free energy functional

In this section we will first explain how the truncated series expansion for the free energy functional is obtained and then we will describe how it can be rescaled so that we can make comparisons between different theories. The scaling of the free energy functional that we describe here was first derived by Duncan McClenegan and An-Chang Shi [53].

We begin with an order parameter $\phi'(\mathbf{x})$ which is a scalar field that measures the thermal average of deviations of the system away from the disordered phase. Thus ϕ' is zero everywhere in the disordered phase: $\phi'_{\text{dis}}(\mathbf{x}) = 0$. For many soft condensed matter systems a natural choice of ϕ' is the deviation of the density of material away from the average density. Throughout this thesis we work in the canonical ensemble, which means that our order parameter is conserved within the volume occupied by our system. This results in the following constraint on ϕ' :

$$\int d\mathbf{x} \phi'(\mathbf{x}) = 0. \quad (2.1)$$

We write our free energy functional as a series expanded about the disordered phase:

$$F'[\phi'] = \sum_{n=2}^{\infty} \frac{1}{n!} \int d\mathbf{x}'_1 \cdots d\mathbf{x}'_n G_n(\mathbf{x}'_1, \cdots, \mathbf{x}'_n) \phi'(\mathbf{x}'_1) \cdots \phi'(\mathbf{x}'_n). \quad (2.2)$$

Here the free energy in the disordered state is taken as the reference point ($F'[\phi'_{\text{dis}}] = 0$), which we can always guarantee by shifting the free energy by a constant value. There is no linear term in the series because we assume that the disordered state is a local minimum on the free energy landscape.

In this work our focus is the *simplest* theories that are useful for describing crystallization. To this end we assume that the cubic and quartic coefficients are both constant with respect to position and we label them as $\gamma' = -G_3(\mathbf{x}_1, \mathbf{x}_2, \mathbf{x}_3)$ and $u = G_4(\mathbf{x}_1, \cdots, \mathbf{x}_4)$ to signify this fact. We assume that $\phi'(\mathbf{x})$ is small so that we can truncate the series at quartic order without significant loss of accuracy. This truncation requires that u is always positive, otherwise our system will be driven towards the unphysical solutions $\phi' \rightarrow \pm\infty$. With these assumptions we are left with the following expression for the free energy functional:

$$F'[\phi'] = F_2[\phi'] + \int d\mathbf{x}' \left\{ -\frac{\gamma'}{3!} \phi'(\mathbf{x}')^3 + \frac{1}{4!} \phi'(\mathbf{x}')^4 \right\}, \quad (2.3)$$

where $F_2[\phi']$ is still the most general form for the quadratic term:

$$F_2[\phi'] = \frac{1}{2} \int d\mathbf{x}'_1 d\mathbf{x}'_2 G_2(\mathbf{x}'_1, \mathbf{x}'_2) \phi'(\mathbf{x}'_1) \phi'(\mathbf{x}'_2). \quad (2.4)$$

We assume the disordered phase is translation invariant, which means

$$G_2(\mathbf{x}_1, \mathbf{x}_2) = G_2(\mathbf{x}_1 + \mathbf{y}, \mathbf{x}_2 + \mathbf{y}) \quad (2.5)$$

for any vector \mathbf{y} . In particular, choosing $\mathbf{y} = -\mathbf{x}_2$, we have $G_2(\mathbf{x}_1, \mathbf{x}_2) = G_2(\mathbf{x}_1 - \mathbf{x}_2, 0)$.

Therefore if we define $G(\mathbf{x}) = G_2(\mathbf{x}, 0)$ then the translation invariance of the system lets us write

$$F_2[\phi'] = \frac{1}{2} \int d\mathbf{x}'_1 d\mathbf{x}'_2 G(\mathbf{x}'_1 - \mathbf{x}'_2) \phi'(\mathbf{x}'_1) \phi'(\mathbf{x}'_2). \quad (2.6)$$

We will replace $G(\mathbf{x}_1 - \mathbf{x}_2)$ with an integral over Fourier modes:

$$G(\mathbf{x}'_1 - \mathbf{x}'_2) = \int \frac{d\mathbf{q}'}{(2\pi)^3} \tilde{G}(\mathbf{q}') e^{i\mathbf{q}' \cdot (\mathbf{x}'_1 - \mathbf{x}'_2)}. \quad (2.7)$$

Putting this back into equation 2.6 and rearranging:

$$\begin{aligned} F_2[\phi'] &= \frac{1}{2} \int d\mathbf{x}'_1 d\mathbf{x}'_2 \int \frac{d\mathbf{q}'}{(2\pi)^3} \tilde{G}(\mathbf{q}') e^{i\mathbf{q}' \cdot (\mathbf{x}'_1 - \mathbf{x}'_2)} \phi'(\mathbf{x}'_1) \phi'(\mathbf{x}'_2) \\ &= \frac{1}{2} \int \frac{d\mathbf{q}'}{(2\pi)^3} \tilde{G}(\mathbf{q}') \int d\mathbf{x}'_1 \phi'(\mathbf{x}'_1) e^{i\mathbf{q}' \cdot \mathbf{x}'_1} \int d\mathbf{x}'_2 \phi'(\mathbf{x}'_2) e^{-i\mathbf{q}' \cdot \mathbf{x}'_2}. \end{aligned} \quad (2.8)$$

The integrals over \mathbf{x}'_1 and \mathbf{x}'_2 give the Fourier transforms of the order parameter field:

$$\tilde{\phi}'(\mathbf{q}) = \int d\mathbf{x}_i \phi'(\mathbf{x}_i) e^{-i\mathbf{q} \cdot \mathbf{x}_i}. \quad (2.9)$$

We are left with

$$F_2[\phi'] = \frac{1}{2} \int \frac{d\mathbf{q}'}{(2\pi)^3} \tilde{G}(\mathbf{q}') \tilde{\phi}'(\mathbf{q}') \tilde{\phi}'(-\mathbf{q}'). \quad (2.10)$$

We assume that the system is isotropic, so that the quadratic coefficient in equation (2.10)

only depends on the magnitude of its argument, $q = |\mathbf{q}|$, so we have that $\tilde{G}(\mathbf{q}) = \tilde{G}(q)$.

In order to describe the formation of ordered phases $\tilde{G}(q)$ must have one or more minima

at some $q_i \neq 0$, i.e. $\left(\frac{d\tilde{G}(q)}{dq} \right)_{q=q_i} = 0$. We call the first minimum q_0 . We can rewrite

equation (2.3) in terms of the scaled length $\mathbf{x} = q_0 \mathbf{x}'$ and $\mathbf{q} = \mathbf{q}'/q_0$. Note that the Fourier

modes pick up a factor of q_0^3 : $\tilde{\phi}'(\mathbf{q}') \rightarrow q_0^3 \tilde{\phi}'(q_0 \mathbf{q})$. The free energy becomes

$$F'[\phi'] = \frac{1}{2q_0^3} \int \frac{d\mathbf{q}}{(2\pi)^3} \tilde{G}(q_0 q) \tilde{\phi}'(q_0 \mathbf{q}) \tilde{\phi}'(-q_0 \mathbf{q}) + \frac{1}{q_0^3} \int d\mathbf{x} \left\{ -\frac{\gamma'}{3!} \phi'(\mathbf{x}/q_0)^3 + \frac{u}{4!} \phi'(\mathbf{x}/q_0)^4 \right\}. \quad (2.11)$$

Our goal is to standardize the functional form of the quadratic coefficient so that we can make comparisons between theories. To this end we will define a new function $\Gamma(q)$ in terms of $\tilde{G}(q)$ so that it has its first minimum at $q = 1$, is shifted vertically so $\Gamma(1) = 0$, and is scaled so that its second derivative at that minimum satisfies $\Gamma''(1) = 8$. Note that each of these conditions is satisfied by the scaled LB model used by McClenegan and Shi, equation (1.13). The new function $\Gamma(q)$ has the following form:

$$\Gamma(q) = \frac{1}{\alpha} \left(\tilde{G}(q_0 q) - \tilde{G}(q_0) \right), \quad (2.12)$$

where $\alpha = q_0^2 \tilde{G}''(q_0)/8$. Rewriting equation (2.11) in terms of $\Gamma(q)$:

$$\begin{aligned} q_0^3 F'[\phi'] &= \frac{1}{2} \int \frac{d\mathbf{q}}{(2\pi)^3} \left(\alpha \Gamma(q) + \tilde{G}(q_0) \right) \tilde{\phi}'(q_0 \mathbf{q}) \tilde{\phi}'(-q_0 \mathbf{q}) + \int d\mathbf{x} \left\{ -\frac{\gamma'}{3!} \phi'(\mathbf{x}/q_0)^3 + \frac{u}{4!} \phi'(\mathbf{x}/q_0)^4 \right\} \\ &= \frac{\alpha}{2} \int \frac{d\mathbf{q}}{(2\pi)^3} \Gamma(q) \tilde{\phi}'(q_0 \mathbf{q}) \tilde{\phi}'(-q_0 \mathbf{q}) \cdots \\ &\quad + \int d\mathbf{x} \left\{ \frac{\tau'}{2} \phi'(\mathbf{x}/q_0)^2 - \frac{\gamma'}{3!} \phi'(\mathbf{x}/q_0)^3 + \frac{u}{4!} \phi'(\mathbf{x}/q_0)^4 \right\}, \end{aligned} \quad (2.13)$$

where in the second line we have transformed the constant part of the quadratic term into real space and defined $\tau' = \tilde{G}(q_0)$. Now we rewrite the free-energy in terms of the scaled order parameter $c\phi(\mathbf{x}) = \phi'(\mathbf{x}/q_0)$, where c is a constant that will be defined shortly:

$$q_0^3 F'[c\phi] = \frac{\alpha c^2}{2} \int \frac{d\mathbf{q}}{(2\pi)^3} \Gamma(q) \tilde{\phi}(\mathbf{q}) \tilde{\phi}(-\mathbf{q}) + \int d\mathbf{x} \left\{ \frac{\tau' c^2}{2} \phi(\mathbf{x})^2 - \frac{\gamma' c^3}{3!} \phi(\mathbf{x}) + \frac{u c^4}{4!} \phi(\mathbf{x})^4 \right\}. \quad (2.14)$$

Next the entire free energy can be rescaled by $u c^4$, so that the quartic coefficient is $1/4!$:

$$\frac{q_0^3}{u c^4} F'[c\phi] = \frac{\alpha}{2 c^2 u} \int \frac{d\mathbf{q}}{(2\pi)^3} \Gamma(q) \tilde{\phi}(\mathbf{q}) \tilde{\phi}(-\mathbf{q}) + \int d\mathbf{x} \left\{ \frac{\tau'}{2 c^2 u} \phi(\mathbf{x})^2 - \frac{\gamma'}{3! c u} \phi(\mathbf{x}) + \frac{1}{4!} \phi(\mathbf{x})^4 \right\}. \quad (2.15)$$

Finally we choose c so that the first quadratic coefficient is equal to $1/2$: $c = \sqrt{\alpha/u}$. The final free energy looks like

$$F[\phi] = \frac{1}{2} \int \frac{d\mathbf{q}}{(2\pi)^3} \Gamma(q) \tilde{\phi}(\mathbf{q}) \tilde{\phi}(-\mathbf{q}) + \int d\mathbf{x} \left\{ \frac{\tau}{2} \phi(\mathbf{x})^2 - \frac{\gamma}{3!} \phi(\mathbf{x})^3 + \frac{1}{4!} \phi(\mathbf{x})^4 \right\}. \quad (2.16)$$

where the unprimed quantities F , τ and γ are related to the original quantities by

$$F[\phi] = (q_0^3 u / \alpha^2) F' \left[\sqrt{\alpha/u} \phi \right], \quad (2.17)$$

$$\tau = \tau' / \alpha, \quad (2.18)$$

$$\gamma = \gamma' / \sqrt{\alpha u}. \quad (2.19)$$

Equation (2.16) is the general form of the free energy functional that we will use throughout this work.

2.2 Ohta-Kawasaki and piecewise models

In the introductory chapter we reproduced the phase diagram that was created by Duncan McClenegan for the LB model. The diagram shows that the Frank-Kasper σ and A15 phases are stable in that model. Directly motivated by that result our first question is: do the complex phases appear in other Ginzburg-Landau theories for crystallization? Our starting point is the Ohta-Kawasaki (OK) model. This model was originally created to describe the formation of periodic ordered phases in diblock copolymers. In fact it was derived as an approximation to the Leibler theory which will be discussed in the next section. The original form of the free energy functional derived by Ohta and Kawasaki is,

$$F_{\text{OK}}[\varphi] = \int \frac{d\mathbf{q}}{(2\pi)^3} \left(\frac{A}{q^2} + Bq^2 \right) \tilde{\varphi}(\mathbf{q})\tilde{\varphi}(-\mathbf{q}) + \int d\mathbf{x} \left\{ \frac{\tau'}{2}\varphi(\mathbf{x})^2 - \frac{\gamma'}{3!}\varphi(\mathbf{x})^3 + \frac{u}{4!}\varphi(\mathbf{x})^4 \right\}. \quad (2.20)$$

When we apply the scaling that led us to equation (2.12) we find that the OK model can be written in the form of equation (2.16) with a scaled quadratic coefficient $\Gamma_{\text{OK}}(q)$ given by:

$$\Gamma_{\text{OK}}(q) = q^2 + \frac{1}{q^2} - 2. \quad (2.21)$$

We see that, like the LB model, the OK model depends on only two parameters, τ and γ .

Plots of the scaled quadratic coefficients $\Gamma_{\text{LB}}(q)$ and $\Gamma_{\text{OK}}(q)$ in equations (1.13) and (2.21) are shown in figure 2.1. We see that, relative to the LB model, $\Gamma_{\text{OK}}(q)$ is larger for wavevectors $q < 1$ and smaller values for $q > 1$. Any differences in the phase diagrams of the two theories must be caused by this difference in the quadratic coefficients. In order to investigate the relative importance of the short ($q > 1$) and long ($q < 1$) wavelength modes on the stability of the ordered phases we create a third model that interpolates between the two theories. We call this the piecewise (PW) model and define it as in equation (2.16) with quadratic coefficient $\Gamma_{\text{PW}}(q)$ given by:

$$\Gamma_{\text{PW}}(q; \lambda_1, \lambda_2) = \begin{cases} \lambda_1 \Gamma_{\text{OK}}(q) + (1 - \lambda_1) \Gamma_{\text{LB}}(q) & q < 1 \\ \lambda_2 \Gamma_{\text{OK}}(q) + (1 - \lambda_2) \Gamma_{\text{LB}}(q) & q > 1 \end{cases}. \quad (2.22)$$

The parameter λ_1 controls the free energy cost associated with the long wavelength ($q < 1$) modes, and λ_2 controls the cost of the short wavelength modes. We can vary these two parameters independently and observe their effect on the complex phases. Figure 2.2 shows

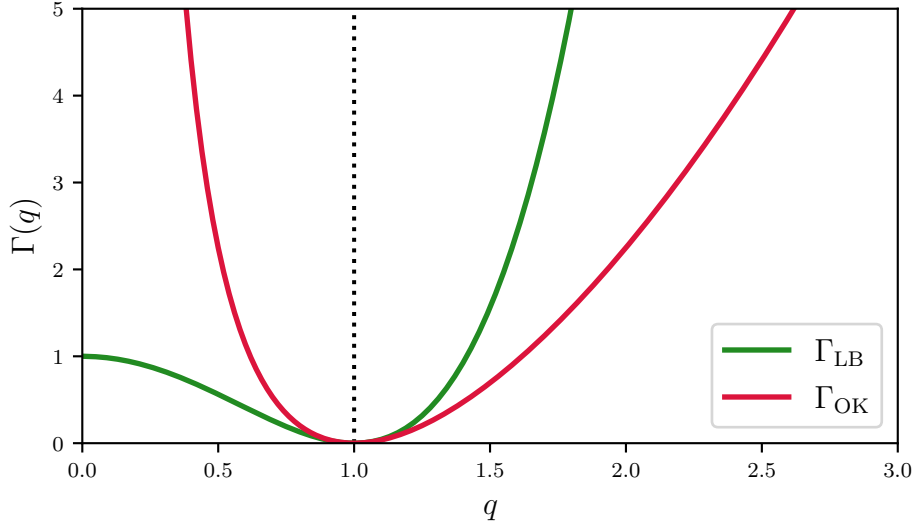


Figure 2.1: Plots of quadratic coefficients for the Landau-Brazovskii model and Ohta Kawasaki model, as defined in equations (1.13) and (2.21), respectively

the shape of Γ_{PW} compared against Γ_{LB} and Γ_{OK} for several different values of λ_1 and λ_2 , demonstrating how we can vary the small- and large- q values of the function independently.

2.3 Modified Leibler theory

An analysis of the OK and PW models presented in the last section will help us to understand what effect the quadratic coefficient $\Gamma(q)$ has on the stability of the complex spherical phases. In the work presented so far we have been interested in probing the universal properties of the complex phases and thus we have avoided discussions of any specific soft condensed matter system. Indeed both the LB and OK models are used to study the formation of ordered phases in many different contexts. We are now going to look at a Ginzburg-Landau theory that is derived for a specific system in which the complex phases are expected to appear. We will investigate how the microscopic parameters of this system influence the shape of the quadratic coefficient. We hope to use this result to connect the generic mechanisms uncovered by the PW theory to those at play in this specific case.

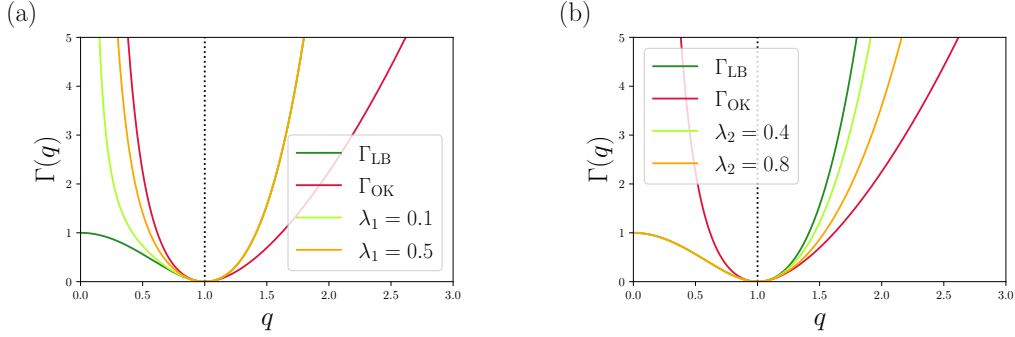


Figure 2.2: Plots of Γ_{PW} (a) λ_1 varied, changing the shape of the left branch of Γ , $\lambda_2 = 0$, fixed. (b) $\lambda_1 = 0$ fixed and λ_2 varied, changing the shape of the right branch. In both figures Γ_{LB} and Γ_{OK} are included for reference.

We have chosen to consider a modification of the theory developed by Ludwik Leibler to describe the formation of ordered phases in diblock copolymers [48]. We discussed block copolymers in some detail in the last chapter (section 1.2.5), where we mentioned that the complex phases sometimes appear. Experiments [29, 30, 31, 61] and self-consistent field theory calculations [61, 43] have shown that the behaviour of these systems depends on the *conformational asymmetry*, ϵ . This parameter is defined below for diblock copolymers, but for now we simply note that both SCFT and experiment show the complex phases only appear in diblock systems when the asymmetry is sufficiently large. Leibler's original calculation assumes there is *no* asymmetry. In this section we modify Leibler's calculation to incorporate conformational asymmetry between the two diblock species and investigate how the inclusion of the ϵ parameter impacts the shape of the quadratic coefficient in the resulting Ginzburg-Landau theory.

We consider a monodisperse system of M diblock copolymer chains with degree of polymerization N . The chains are all composed of two chemically distinct polymer species, A and B . The number of segments of type κ is denoted N_κ ($\kappa = A, B$), so that $\sum_\kappa N_\kappa = N$. A useful parameter in this theory is the composition fraction f , defined as $f = N_A/N$. In Leibler's calculation the Kuhn statistical segment lengths of the two polymer species are assumed to be the same, but here we relax that assumption. Let the Kuhn length of the κ -type polymer be b_κ and define the segment asymmetry parameter as the square of the ratios of the Kuhn lengths: $\epsilon = (b_A/b_B)^2$. Taking $b_B = b$, it follows that $b_A = \sqrt{\epsilon}b$.

Define the reduced number density of the κ segments as,

$$\rho_\kappa(\mathbf{x}) = \frac{\mathcal{V}}{MN} \sum_{\mathbf{x}_\kappa} \delta(\mathbf{x} - \mathbf{x}_\kappa), \quad (2.23)$$

where the system and the sum is over the centre-of-mass position of every κ -type polymer segment, of which there are MN_κ in total. The factor of volume, \mathcal{V} in this expression makes it into a dimensionless quantity. In the uniformly mixed (disordered) state, the thermal averages of the reduced densities of A and B are $\langle \rho_A(\mathbf{x}) \rangle = f$ and $\langle \rho_B(\mathbf{x}) \rangle = (1 - f)$, respectively. The system is assumed to be *incompressible*, which means that the thermal average of the local density must always be a constant value:

$$\langle \rho_A(\mathbf{x}) \rangle + \langle \rho_B(\mathbf{x}) \rangle = 1. \quad (2.24)$$

This incompressibility condition holds even when the system is not in the disordered state. Equation (2.24) means that a good choice of order parameter for this system is the thermal average of the *deviation* of the local density away from its value in the disordered state:

$$\phi'(\mathbf{x}) = \langle \rho_A(\mathbf{x}) \rangle - f. \quad (2.25)$$

Leibler's theory is applicable in the so-called weak-segregation limit. This refers to the region of the phase diagram close to the order-disorder transition line, where the local density of both A and B segments is assumed to be close to the average value. In this limit, we can assume that ϕ' is small and we can construct a Ginzburg-Landau theory by expanding the free energy functional in powers of ϕ' about the disordered state. This part of the calculation follows Leibler's procedure exactly, nevertheless it is presented in full in the first section of appendix A for the convenience of the interested reader. The result of this expansion is a free energy functional of the form,

$$\beta F'[\phi'] = \sum_{n=2}^{\infty} \frac{1}{n!} \int \frac{d\mathbf{q}_1}{(2\pi)^3} \cdots \int \frac{d\mathbf{q}_n}{(2\pi)^n} \delta(\mathbf{q}_1 + \cdots + \mathbf{q}_n) \tilde{G}_n(\mathbf{q}_1, \cdots, \mathbf{q}_n) \tilde{\phi}'(\mathbf{q}_1) \cdots \tilde{\phi}'(\mathbf{q}_n). \quad (2.26)$$

Here β is inversely proportional to the temperature T , $\beta = (k_B T)^{-1}$ where k_B is the Boltzmann constant. Equation (2.26) looks like the Fourier transform of equation (2.2) when translation invariance is assumed. Since we are interested in free energy functionals of the form in equation (2.16), we will truncate this series at quartic order and take the cubic and quartic coefficients to be constant (independent of \mathbf{q}). Leibler's derivation gives us the

following expression for the quadratic coefficient:

$$\tilde{G}_2(\mathbf{q}) = \frac{1}{\tilde{C}_2(\mathbf{q})}, \quad (2.27)$$

where $\tilde{C}_2(\mathbf{q})$ is the Fourier transform of the two point correlation function in the disordered phase:

$$C_2(\mathbf{x}_1 - \mathbf{x}_2) = \langle \delta\rho_A(\mathbf{x}_1)\delta\rho_A(\mathbf{x}_2) \rangle_{dis}. \quad (2.28)$$

Leibler demonstrates how an approximate expression for C_2 can be obtained using the random phase approximation (RPA). The RPA relies on the fact that closed form expressions, can be obtained for the two point correlation functions of *non-interacting* diblock copolymers. This is done using the Gaussian, or bead-spring model, which treats a polymer chain with degree of polymerization N as a string of $N + 1$ beads connected by springs. A good description of the model can be found in the textbook by T. Kawakatsu [62]. In particular the Kuhn length of each polymer species shows up in the spring constant of the segments, and so the non-interacting asymmetric diblock copolymer is modelled as a chain composed of two connected springs with different stiffness. There are three two-point correlation functions, S_{AA} , S_{BB} , and S_{AB} , that are needed to find C_2 using the RPA. Each of these is computed in section 2 of appendix A. The resulting expressions can be rescaled to find:

$$S_{AA}(q) = g(\epsilon q^2, f), \quad (2.29)$$

$$S_{BB}(q) = g(q^2, 1 - f), \quad (2.30)$$

$$S_{AB}(q) = h(\epsilon q^2, f) h(q^2, 1 - f), \quad (2.31)$$

where g (a modified version of the Debye function) and h are defined as

$$g(y, \alpha) = \frac{2}{y^2} (\alpha y + e^{-\alpha y} - 1), \quad (2.32)$$

$$h(y, \alpha) = \frac{1}{y} (1 - e^{-\alpha y}). \quad (2.33)$$

Note that by setting $\epsilon = 1$ we recover the expressions found by Leibler for the symmetric case. The details of the RPA are presented in section 3 of appendix A. The final expression for the quadratic coefficient of the modified Leibler theory is given by,

$$G_2(q) = \frac{S(q)}{W(q)} - 2\chi, \quad (2.34)$$

where χ (called the Flory parameter) is a measure of the interaction strength between A

and B segments, and,

$$S(q) = S_{AA}(q) + 2S_{AB}(q) + S_{BB}(q), \quad (2.35)$$

$$W(q) = S_{AA}(q)S_{BB}(q) - (S_{AB}(q))^2. \quad (2.36)$$

Equation (2.34) for the quadratic coefficient of the ML theory is the main result for this section. In order to draw comparisons between this theory and the models considered in section 2.2 we need to rescale the quadratic term so that it has the form of equation (2.12). We can compute the second derivative of $\tilde{G}_2(q)$ analytically, but we rely on a numerical root finding algorithm to calculate the minimum, q_0 .

2.4 SALR potential theories

In the introduction (section 1.4) we described some results that used the DFT to construct phase diagrams for systems of hard spheres with SALR pairwise interactions. Those results hinted to us that the complex phases might be stable in such systems. It is now interesting to see if we can predict the onset of the complex phases by comparing the form of these theories with the quadratic coefficients that we have considered so far. SALR systems are also interesting to investigate because the parameters that appear in these potentials are simple to interpret and can provide us with some intuition about the origin of the long and short wavelength modes of the quadratic coefficient.

In this section we describe how a Ginzburg-Landau theory can be derived from the classical DFT. We start with the expression for the free energy, which is a functional of the density of spheres, $\rho(\mathbf{x})$. One expression for the free energy functional consists of three contributions [59]:

$$F[\rho] = F_0[\rho] + F_{CS}[\rho] + F_2[\rho]. \quad (2.37)$$

Here $F_0[\rho]$ is the free energy of an ideal gas:

$$F_0[\rho] = k_B T \int d\mathbf{x} \rho(\mathbf{x}) (\ln \rho(\mathbf{x}) - 1). \quad (2.38)$$

The second term, $F_{CS}[\rho]$, is known as the Carnahan-Starling expression, it is an approxima-

tion that accounts for the hard-core repulsion of the spheres within the classical DFT:

$$F_{CS}[\rho] = k_B T \int d\mathbf{x} \frac{\eta(\mathbf{x})(4 - 3\eta(\mathbf{x}))}{(1 - \eta(\mathbf{x}))^2}, \quad (2.39)$$

where $\eta(\mathbf{x}) = \pi\sigma^3\rho(\mathbf{x})/6$, and σ is the diameter of the spheres. The last term in equation (2.37) is the pairwise interaction between the spheres:

$$F_2[\rho] = \frac{1}{2} \int \int d\mathbf{x} d\mathbf{x}' \rho(\mathbf{x}) w(\mathbf{x} - \mathbf{x}') \rho(\mathbf{x}'). \quad (2.40)$$

Here $w(\mathbf{r})$ is an interaction potential that captures the desired short-range attractive, long-range repulsive behaviour.

We could of course expand equation (2.37) in powers of $\rho(\mathbf{x})$ and truncate at quartic order to obtain our Ginzburg Landau theory. However for our purposes it is more efficient to simply note that only F_2 will contribute to the q -dependence of the quadratic coefficient in the series. Recall that we scale our theories to match equation (2.16). Therefore the particular expressions for the remaining coefficients will turn out to be irrelevant. Saving ourselves some time, then, we focus our attention on equation (2.40). We want systems with order parameters that satisfy equation (2.1), so we write the density of hard spheres at position \mathbf{x} as a deviation away from the average value, $\bar{\rho}$: $\rho(\mathbf{x}) = \bar{\rho} + \phi'(\mathbf{x})$. Then F_2 becomes

$$F_2 = \frac{1}{2} \int \int d\mathbf{x} d\mathbf{x}' \phi'(\mathbf{x}) w(\mathbf{x} - \mathbf{x}') \phi'(\mathbf{x}') + const. \quad (2.41)$$

Using the fact that $\int d\mathbf{x} \phi'(\mathbf{x}) = 0$ to eliminate the linear terms we see that the functional form of F_2 is unchanged. Comparing with equation (2.6), the connection between the classical DFT and the Ginzburg-Landau theory is clear. The quadratic coefficient $\Gamma(q)$ is obtained simply by scaling the SALR potential:

$$\Gamma(q) = \frac{8}{q_0^2 \tilde{w}''(q_0)} (\tilde{w}(q_0 q) - \tilde{w}(q_0)), \quad (2.42)$$

where $\tilde{w}(q)$ is the Fourier transform of the interaction potential and q_0 is the minimum of \tilde{w} : $\tilde{w}'(q_0) = 0$. We will next consider two specific expressions for $w(x)$.

2.4.1 The double-Gaussian potential

We consider a pair potential with the desired SALR behaviour and a simple functional form, the sum of two Gaussian functions:

$$w_{\text{DG}}(r) = -A \exp(-r^2/\sigma_1^2) + B \exp(-r^2/\sigma_2^2). \quad (2.43)$$

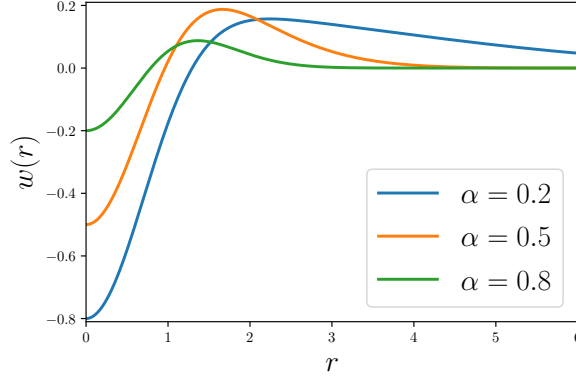


Figure 2.3: Plots of the real-space interaction potential $w_{\text{DG}}(r)$ for the double-Gaussian model, equation (2.44), with the WCA condition ($C = \alpha$) using various values of the parameter α .

Here σ_1 and σ_2 are the length scales of the attractive and repulsive parts of the potential, respectively, so $\sigma_1 < \sigma_2$. We can rescale the length r by σ_1 and the energy scale by A to obtain

$$w_{\text{DG}}(r) = -\exp(-r^2) + C \exp(-\alpha^2 r^2), \quad (2.44)$$

where $C = B/A$ and $\alpha = \sigma_1/\sigma_2 < 1$. In the DFT, a criterion known as the WCA (Weeks, Chandler, Anderson) condition is often used to determine the overall amplitude of the interaction potential. As described in [63], the WCA condition requires that the Fourier transform, $\tilde{w}_{\text{DG}}(q)$, passes through the origin when $q = 0$. Applied to our expression, this constraint yields $C = \alpha$.

Plots of the real-space potential, $w_{\text{DG}}(r)$, are shown in figure 2.3 for three different values of α . The plots show the SALR behaviour of this mode. Smaller values of α correspond to a longer range for the repulsive part of the potential and a deeper minimum.

Taking the Fourier transform of equation (2.44) with $C = \alpha$ gives,

$$\tilde{w}_{\text{DG}}(q) = -\frac{1}{\sqrt{2}}e^{-q^2/4} + \frac{1}{\sqrt{2}}e^{-q^2/4\alpha^2}. \quad (2.45)$$

The minimum of this potential can be found analytically:

$$q_0 = \left(\frac{8\alpha^2 \ln(\alpha)}{\alpha^2 - 1} \right)^{1/2}. \quad (2.46)$$

The second derivative of $\tilde{w}_{\text{DG}}(q)$ is also required to compute the quadratic coefficient for this theory.

$$\tilde{w}_{\text{DG}}''(q) = -\frac{1}{4\sqrt{2}}q^2 \left(e^{-q^2/4} - \frac{1}{\alpha^4}e^{-q^2/4\alpha^2} \right) + \frac{1}{2\sqrt{2}} \left(e^{-q^2/4} - \frac{1}{\alpha^2}e^{-q^2/4\alpha^2} \right). \quad (2.47)$$

The scaled quadratic coefficient for this theory, which we call Γ_{DG} , can be computed following equation (2.12), with $\tilde{G}(q) = \tilde{w}_{\text{DG}}(q)$ in equation (2.45), q_0 given by equation (2.46), and \tilde{G}'' given by equation (2.47).

2.4.2 The step potential

The Double-Gaussian SALR potential considered in the last section is appealing to work with because of its simple functional form. A drawback to that potential is that it depends only on a single parameter, α , which means we have limited control over its shape. In this section we will describe another SALR potential which has a more complex expression. This potential, which we call the generic step potential, was analysed by Zhuang and Charbonneau [59]. These authors used the DFT as well as numerical simulations to find a phase diagram for this model that included the fcc phase. The potential has the following functional form:

$$w_{\text{step}}(r) = \begin{cases} C & r < 1, \\ -A & 1 < r < 1 + \sigma_1, \\ \frac{B}{\sigma_2}(1 + \sigma_1 + \sigma_2 - r) & 1 + \sigma_1 < r < 1 + \sigma_1 + \sigma_2, \\ 0 & r > 1 + \sigma_1 + \sigma_2. \end{cases} \quad (2.48)$$

We can find the Fourier transform of w_{step} analytically, although the expression is a little messy:

$$\begin{aligned} \tilde{w}_{\text{step}}(q) = 4\pi & \left\{ C f(q) + A \left[f(q) - f((1 + \sigma_1)q) \right] + \right. \\ & + \frac{B}{\sigma_2 q^4} \left[(2 + q^2(1 + \sigma_1)\sigma_2) \cos((1 + \sigma_1)q) - 2 \cos((1 + \sigma_1 + \sigma_2)q) + \right. \\ & \left. \left. + q(1 + \sigma_1 - \sigma_2) \sin((1 + \sigma_1)q) - q \sin(\sigma + 1 + \sigma_2 + 1)q \right] \right\}, \end{aligned} \quad (2.49)$$

where

$$f(q) = \frac{-q \cos(q) + \sin(q)}{q^3}. \quad (2.50)$$

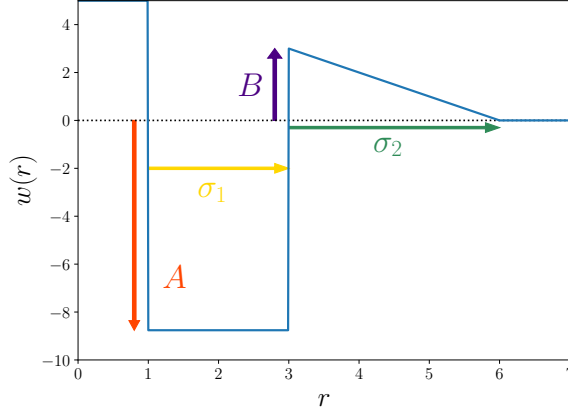


Figure 2.4: Plot of the step potential defined in equation (2.48) with $\sigma_1 = 2$, $\sigma_2 = 3$, $B = 3$, $C = 5$, and $A \approx 8.760$, as determined by the WCA condition, equation (2.51).

The parameter A can be set using the WCA condition described in the last section,

$$A = \frac{C + \frac{1}{4}B\sigma_2 (6 + 6\sigma_1^2 + 4\sigma_2 + 4\sigma_1(3 + \sigma_2))}{3\sigma_1 + 3\sigma_1^2 + \sigma_1^3}. \quad (2.51)$$

In order to find the scaled quadratic coefficient, $\Gamma_{step}(q)$ we will need to find the first minimum of equation (2.49). We do this numerically using a root finding algorithm. We also need the second derivative, which can be found analytically.

Plots of $w_{step}(r)$ are shown in figure 2.4. This model is appealing because we have a great deal of control over its shape. We can manipulate the free parameters in equation (2.48) and observe how they affect the shape of the scaled quadratic coefficient $\Gamma_{step}(q)$. We can then connect this change of shape with the physical interpretation of these parameters in order to gain more insight into what factors in the SALR potential control the relative stability of the spherical packing phases.

We have the Landau-Brazovskii (LB) and Ohta Kawasaki (OK) models, equations (1.13) and (2.21), as well as the piecewise (PW) model, (2.22), that interpolates between them. We will compare the behaviours of these three models in order to gain an understanding of the mechanisms that control the relative stabilities of the spherical packing phases. We will then look at the shape of the gamma functions for the modified Leibler (ML) theory, equation (2.34), and the double-Gaussian SALR potential, equation (2.45), (both scaled according

to equation (2.12)) and attempt to connect the parameters in those models with the onset of the complex spherical phases. In the next section we describe how this calculation is performed.

Chapter 3

Numerical methods

In this chapter we will describe the computational techniques used to obtain the phase diagrams presented in chapter 4 of this thesis. The goal of this chapter is to provide the reader with enough detail to reproduce these results. We start with a free energy functional, $F[\phi]$, of the form given in equation (2.16), and a set of candidate phases. We do not consider every possible ordered phase, we instead restrict ourselves to a smaller set of phases of interest. We will use the symbol \mathcal{P} to denote the set of phases under consideration and p to denote individual elements of this set. We use a subscript p to denote an order-parameter field that has symmetry consistent with the phase p : ϕ_p . For example $\phi_{bcc}(\mathbf{x})$ is a real-space field with the bcc symmetry and $\tilde{\phi}_{bcc}(\mathbf{q})$ is its Fourier transform. F will depend on multiple parameters, including the τ and γ variables of equation (2.16) and possibly others as well. For a given set of parameter values the goal is to determine which of the phases in \mathcal{P} is the most stable, i.e. has the lowest free energy. Since there are an infinite number of fields ϕ_p that are consistent with the phase p , and since each of these has a different free energy, we need to minimize $F[\phi_p]$ for each phase individually. This optimization is described in section 3.1. Once the minimum free energy has been determined for each p in \mathcal{P} , the stable phase can be determined at this point in the space of model parameters. By performing this calculation over a range of parameter values we can construct a phase diagram for the model. Section 3.2 describes how the phase diagrams are constructed.

3.1 Phase optimization

In this section we describe how a given phase p is optimized for the free energy functional of interest. We are looking for the particular field ϕ_p^* that minimizes the free energy while remaining consistent with the symmetries of p .

In this work we are interested in *periodic* phases. Any such phase can be divided into an infinite number of identical rectangular boxes, or unit cells. Thus, in order to find the optimal field for phase p it is sufficient for us to optimize ϕ_p over a single unit cell. Let l_x , l_y , and l_z be the dimensions of the unit cell, and $v_p = l_x l_y l_z$ be its volume. ϕ_p can be written as a sum of plane waves whose periodicity is commensurate with the unit cell size:

$$\phi_p(\mathbf{x}) = \sum_{ijk} \tilde{\phi}_p(\mathbf{q}_{ijk}) e^{i\mathbf{q}_{ijk} \cdot \mathbf{x}}, \quad (3.1)$$

where \mathbf{q}_{ijk} are the reciprocal lattice vectors associated with this unit cell:

$$\mathbf{q}_{ijk} = \frac{2\pi i}{l_x} \hat{\mathbf{x}} + \frac{2\pi j}{l_y} \hat{\mathbf{y}} + \frac{2\pi k}{l_z} \hat{\mathbf{z}}, \quad (3.2)$$

and i, j, k are integers. The coefficients $\tilde{\phi}_{ijk} \equiv \tilde{\phi}_p(\mathbf{q}_{ijk})$ are given by:

$$\tilde{\phi}_{ijk} = \frac{1}{v_p} \int_{v_p} d\mathbf{x} \phi_p(\mathbf{x}) e^{-i\mathbf{q}_{ijk} \cdot \mathbf{x}}, \quad (3.3)$$

where the integration is over a single unit cell.

Each phase will have a different unit cell size, so in order to make comparisons we need the minimum free-energy *density* for each phase, $f_p = F_p/v_p$, where F_p is the free energy integrated over the entire unit cell and v_p is the volume of that unit cell. Starting from the general expression for the free energy, the density is given by:

$$\begin{aligned} f_p &= \frac{1}{v_p} \int_{v_p} d\mathbf{x} \left[\frac{1}{2} \int d\mathbf{x}' \phi_p(\mathbf{x}) G(\mathbf{x} - \mathbf{x}') \phi_p(\mathbf{x}') + \left\{ \frac{\tau}{2} \phi_p(\mathbf{x})^2 - \frac{\gamma}{3!} \phi_p(\mathbf{x})^3 + \frac{1}{4!} \phi_p(\mathbf{x})^4 \right\} \right] \\ &= \frac{1}{2} \sum_{ijk} \Gamma(q_{ijk}) \left| \tilde{\phi}_{ijk} \right|^2 + \frac{1}{v_p} \int_{v_p} d\mathbf{x} \left\{ \frac{\tau}{2} \phi_p(\mathbf{x})^2 - \frac{\gamma}{3!} \phi_p(\mathbf{x})^3 + \frac{1}{4!} \phi_p(\mathbf{x})^4 \right\}. \end{aligned} \quad (3.4)$$

In order to minimize (3.4) for a given phase we must optimize the field ϕ_p and *also* the unit cell dimensions l_x, l_y, l_z . The minimization algorithm for the phase p is summarized in table 3.1.

Phase optimization algorithm
<ol style="list-style-type: none"> 1. Initialize a unit cell for the target phase. This involves choosing both box dimensions and a field ϕ with the required symmetry. Details on the initialization of each phase considered in this work are given in section 3.1.1. 2. Fix the box size and optimize the order parameter field ϕ_p so that it minimizes the free energy density, (3.4). Details of this optimization are given in section 3.1.2. 3. Fix the field and stretch or compress the box size until we find the optimal dimensions. This process is described in section 3.1.3. 4. Alternate between steps 2 and 3 until the resulting change in the free energy density is below some threshold error tolerance. Note that this tolerance should be much smaller than the difference between the free energy densities of the phases.

Table 3.1: Summary of the algorithm used to find the minimum free energy density for a each phase p in \mathcal{P} .

3.1.1 Initialization

The unit cell is a three dimensional box with one corner located at the origin and with dimensions l_x, l_y, l_z . Each axis is divided into N_α equal segments of length $\Delta\alpha = l_\alpha/N_\alpha$ ($\alpha = x, y, z$) so that the unit cell is discretized into $N = N_x N_y N_z$ boxes, each with volume $v = \Delta x \Delta y \Delta z$. We create a discrete approximation to the field $\phi(\mathbf{x})$ by treating its value within the $(ijk)^{\text{th}}$ box as a constant value equal to $\phi_{ijk} \equiv \phi(\mathbf{x}_{ijk})$. Here \mathbf{x}_{ijk} is the vector that points from the origin to the bottom corner of the $(ijk)^{\text{th}}$ box, and $i = 0, \dots, N_x - 1$, $j = 0, \dots, N_y - 1$, and $k = 0, \dots, N_z - 1$. The accuracy of this discretization depends on whether $\phi(\mathbf{x})$ changes sufficiently slowly relative to the grid spacing.

The discretization of the real-space field $\phi(\mathbf{x})$ also affects the discrete Fourier transform

(DFT). The reciprocal vectors \mathbf{q}_{lmn} have the same form as equation (3.2), but now the highest frequency mode is set by the grid spacing: $\nu_{\alpha, max} = \frac{2\pi}{\Delta\alpha}$. This means that the series expression, equation (3.1), is truncated. The assumption that $\phi(\mathbf{x})$ varies slowly means that these high-frequency modes which we ignore are not important to accurately describe the field.

For the remaining modes, the Fourier coefficients are computed using the discretization of equation (3.3):

$$\begin{aligned}\tilde{\phi}_{lmn} &\rightarrow \frac{1}{v_p} \sum_{lmn} \Delta x \Delta y \Delta z \phi_{lmn} \exp\{i\vec{q}_{ijk} \cdot \vec{x}_{lmn}\} \\ &= \frac{1}{N} \sum_{lmn} \phi_{lmn} \exp\{i\vec{q}_{ijk} \cdot \vec{x}_{lmn}\},\end{aligned}\quad (3.5)$$

with $(-\frac{N_x}{2} + 1) \leq l \leq \frac{N_x}{2}$, $(-\frac{N_y}{2} + 1) \leq m \leq \frac{N_y}{2}$, and $(-\frac{N_z}{2} + 1) \leq n \leq \frac{N_z}{2}$.

The free energy density of the discretized field is given by ,

$$f = \frac{1}{2} \sum_{ijk} \Gamma(q_{ijk}) \left| \tilde{\phi}_{ijk} \right|^2 + \frac{1}{N} \sum_{ijk} \left\{ \frac{\tau}{2} \phi_{ijk}^2 - \frac{\gamma}{3!} \phi_{ijk}^3 + \frac{1}{4!} \phi_{ijk}^4 \right\}, \quad (3.6)$$

where the first sum is over Fourier modes, $\tilde{\phi}_{ijk}$ and the second sum is over the discretized ϕ values in real-space. We should choose the N_α large enough that equation (3.6) is independent of them.

Now that we understand how the volume is discretized, we need to initialize the order parameter field for the phase of interest. Figure 3.1 shows the initial unit cell for each the nine phases considered in this work: the lamellar (lam), hexagonally close-packed cylindrical (hex), double gyroid (gyr), body-centred cubic (bcc), and face-centred cubic (fcc) phases, as well as the Frank Kasper A15, σ , C14, and C15 phases. The full details of each can be found in appendix B.

The optimization algorithm described in the next two sections can sometimes cause ϕ_p to evolve into a *different* phase. The final step in the initialization process is to choose a point somewhere in the phase space where the phase of interest is well behaved, optimize the field at that point, and then save the resulting order parameter. Using this pre-optimized field as an initial condition for the remaining points in the phase diagram is beneficial because it speeds up the convergence of the algorithm and decreases the frequency with which the

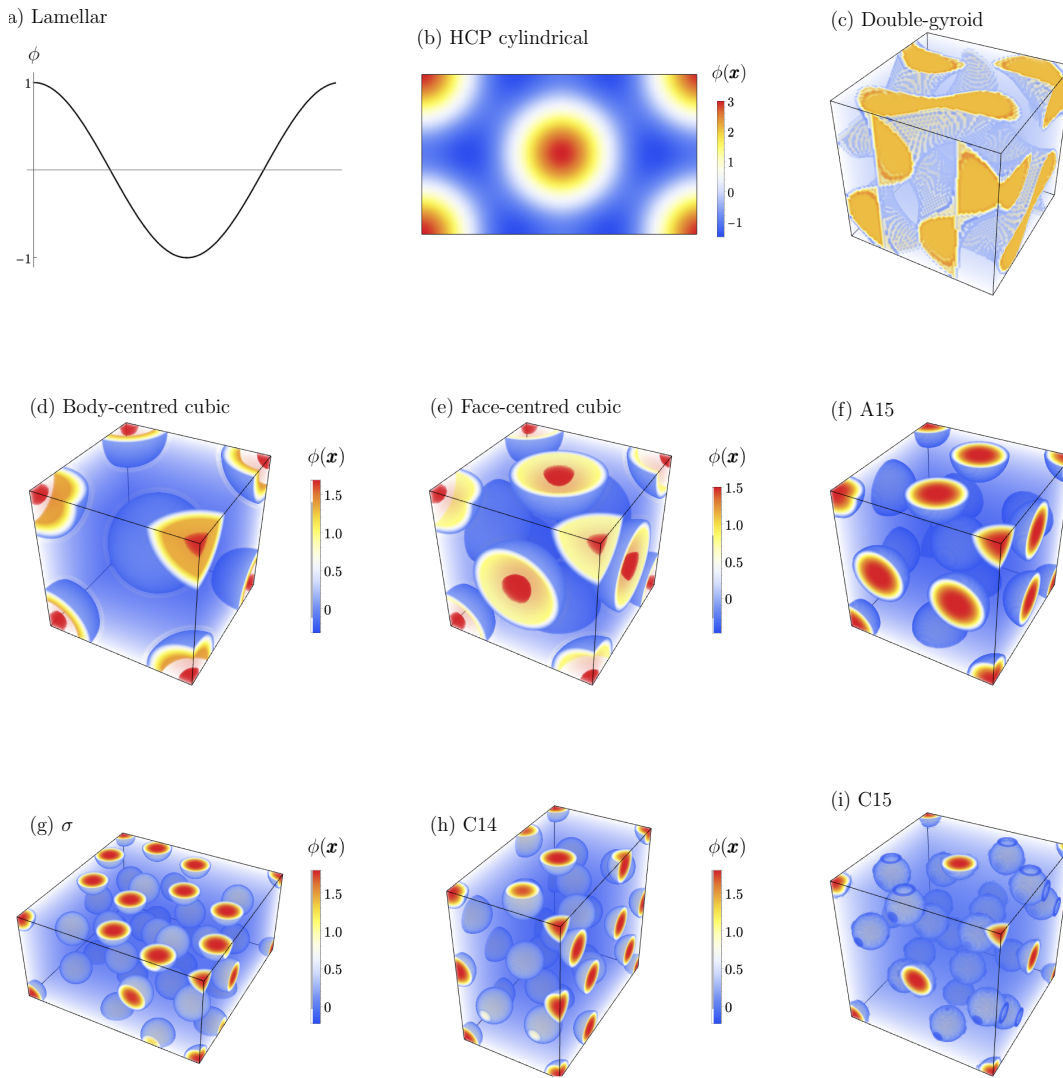


Figure 3.1: Initial unit cells for each of the nine phases considered in this work. Note that the lamellar phase, (a), is one-dimensional and the hcp cylindrical phase (b) is two-dimensional. The remaining phases are three dimensional.

field evolves away from the phase of interest.

3.1.2 Free energy optimization

In this section we describe how the order parameter field for a given phase p is optimized when the dimensions of the unit cell are fixed. We are looking for the optimized field ϕ_p^* which minimizes the free energy density in equation (3.4):

$$\left(\frac{\delta f}{\delta \phi}\right)_{\phi=\phi_p^*} = 0. \quad (3.7)$$

We can locate stationary states of $f[\phi]$ using a gradient descent algorithm, but recall this problem is subject to the constraint that the order parameter is *conserved*, meaning the integral of $\phi(\mathbf{x})$ over the entire system must be 0 (see equation (2.1)). For periodic ϕ , this conservation constraint must hold over a single unit cell:

$$\int_v d\mathbf{x} \phi_p(\mathbf{x}) = 0, \quad (3.8)$$

or, equivalently, $\tilde{\phi}_p(\mathbf{q} = 0) = 0$. If we start with an initial guess, ϕ_p^0 , that matches the symmetry of the target phase and satisfies equation (3.8), then we can ensure that the constraint is always satisfied by evolving ϕ_p according to the continuity equation:

$$\frac{\partial \phi_p(\mathbf{x})}{\partial t} = -\nabla \cdot \mathbf{j}(\mathbf{x}), \quad (3.9)$$

where $\mathbf{j}(\mathbf{x})$ is the current density:

$$\mathbf{j}(\mathbf{x}) = -D\nabla\mu(\mathbf{x}). \quad (3.10)$$

Here D is the diffusion coefficient, which we have assumed is a constant, and $\mu(\mathbf{x})$ is the chemical potential field, which is related to the order parameter field through the equation of state:

$$\mu(\mathbf{x}) = \frac{\delta f[\phi]}{\delta \phi(\mathbf{x})}. \quad (3.11)$$

Putting all of this together we get the following expression for the time evolution of ϕ_p ,

$$\frac{\partial \phi_p}{\partial t} = \nabla^2 \frac{\delta f[\phi_p]}{\delta \phi_p}. \quad (3.12)$$

We are not interested in dynamics here beyond ensuring equation (3.8) is satisfied, so we have scaled the time variable t to eliminate D from the expression. ϕ_p is evolved according

to equation (3.12) until a steady state solution is reached ($\partial_t \phi = 0$). This solution will be ϕ_p^* , the *local* minima of the free energy density subject to the constraint in equation (3.8). The algorithm used to find ϕ_p^* is based on the one described by Kai Jiang, et. al. [64]. Details of this algorithm can be found in section 2 of appendix B.

3.1.3 Unit cell optimization

In this section we describe how the size of the unit cell is determined for a given order parameter field ϕ_p . We can visualize fixing the density profile, stretching or compressing the box, and observing how the free energy changes. Referring back to equations (3.1) and (3.2), we hold the amplitudes, $\tilde{\phi}_{ijk}$ fixed and vary the \mathbf{q}_{ijk} vectors by varying the lengths l_x, l_y, l_z . First a quick bit of notation, define $b_\alpha \equiv 2\pi/l_\alpha$, $\alpha = x, y, z$, so that,

$$\vec{q}_{ijk} = ib_x \hat{\mathbf{x}} + jb_y \hat{\mathbf{y}} + kb_z \hat{\mathbf{z}}. \quad (3.13)$$

Consider again the expression for the free energy density, equation (3.4). We will make the dependence on the box size clear by writing f entirely in terms of the Fourier space representation of ϕ :

$$f[\phi] = \sum_{\mathbf{q}} \left(\frac{1}{2} \Gamma(q) |\hat{\phi}_p(\mathbf{q})|^2 + \frac{\tau}{2} |\hat{\phi}_p(\mathbf{q})|^2 - \frac{\gamma}{3!} \sum_{\mathbf{q}'\mathbf{q}''} \hat{\phi}_p(\mathbf{q}) \hat{\phi}_p(\mathbf{q}') \hat{\phi}_p(\mathbf{q}'') \cdots \right. \\ \left. + \frac{1}{4!} \sum_{\mathbf{q}'\mathbf{q}''\mathbf{q}'''} \hat{\phi}_p(\mathbf{q}) \hat{\phi}_p(\mathbf{q}') \hat{\phi}_p(\mathbf{q}'') \hat{\phi}_p(\mathbf{q}''') \right). \quad (3.14)$$

Here the sum over \mathbf{q} is shorthand for a sum over the integer coefficients i, j, k of equation (3.13). We see that only the first term will change when we vary any b_α with $\tilde{\phi}$ held fixed. Therefore we only need to minimize this *non-local* part of the free energy:

$$f_{nl} = \frac{1}{2} \sum_{ijk} \Gamma(q_{ijk}) |\tilde{\phi}_{ijk}|^2. \quad (3.15)$$

Taking the derivative of f_{nl} with respect to b_α :

$$\frac{\partial f_{nl}}{\partial b_\alpha} = \frac{1}{2} \sum_{ijk} |\tilde{\phi}_{ijk}|^2 \frac{\partial \Gamma(q_{ijk})}{\partial q_{ijk}} \frac{\partial q_{ijk}}{\partial b_\alpha} \\ = \sum_{ijk} \Gamma'(q_{ijk}) |\tilde{\phi}_{ijk}|^2 \frac{i_\alpha^2 b_\alpha}{q_{ijk}}, \quad (3.16)$$

where $i_\alpha = i, j, k$ when $\alpha = x, y, z$, respectively, and we have used the fact that the magnitude of q_{ijk} depends on the b_α :

$$q_{ijk} = (i^2 b_x^2 + j^2 b_y^2 + k^2 b_z^2)^{1/2}. \quad (3.17)$$

We therefore have three equations to solve in order to find the optimal b_x, b_y and b_z :

$$\sum_{ijk} \frac{i_\alpha^2}{q_{ijk}} \Gamma'(q_{ijk}) \left| \tilde{\phi}_{ijk} \right|^2 = 0, \quad (3.18)$$

for $\alpha = x, y, z$. Note that these equations depend on the values of the b_α through the reciprocal lattice vectors, equation (3.17). We use a conjugate gradient method like the one described in [65] to find the solutions to equation (3.18). The details of the algorithm can be found in section 3 of appendix B.

3.2 Constructing phase diagrams

In this section we describe how phase diagrams like the one shown in figure 1.7 are constructed. All of our free energy functionals depend on some set of parameters which includes the coefficients τ and γ , as well as any other parameters, ω , appearing in the quadratic coefficient $\Gamma = \Gamma(q; \omega)$. In general we are interested in how the minimum free energy density of each phase, $f_p^* = f_p(\phi_p^*)$, varies as a function of these parameters. Let us take τ and γ as an example. In order to compute the τ - γ phase diagram we begin by choosing a range for each parameter and then taking a discrete set of values within that range, so that we end up with a set of pairs (τ_i, γ_j) . We find the minimal free energy density for each phase in the set \mathcal{P} at each point in the set of pairs. By comparing each of these densities at the point (τ_i, γ_j) we can determine the phase that is stable at that point: $p^* = \{p \mid f_p^* = \min_{p' \in \mathcal{P}} f_{p'}^*\}$. This can be visualized in a diagram like figure 3.2, which shows how p^* varies as a function of τ and γ , and also shows how the calculation is first done over a discrete set of points.

Figure 3.3 shows how the free energy densities for each phase considered vary as a function of γ , with $\tau = -0.05$ fixed. In this plot we have zoomed into the region between $\gamma = 0.5$ and $\gamma = 0.8$. Comparison with the diagram in figure 3.2 shows that there is a transition point here between the hex and bcc phase. In order to determine the approximate value of γ at which this transition occurs, we first interpolate between the calculated points using a

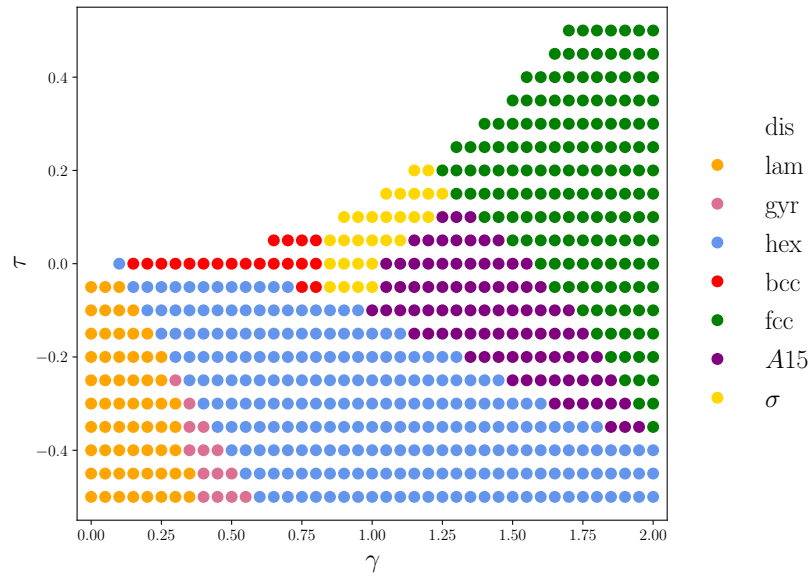


Figure 3.2: Preliminary phase diagram for the Landau Brazovskii model, coloured dots indicate which phase p in \mathcal{P} has the lowest free energy density at each value of the parameters τ and γ

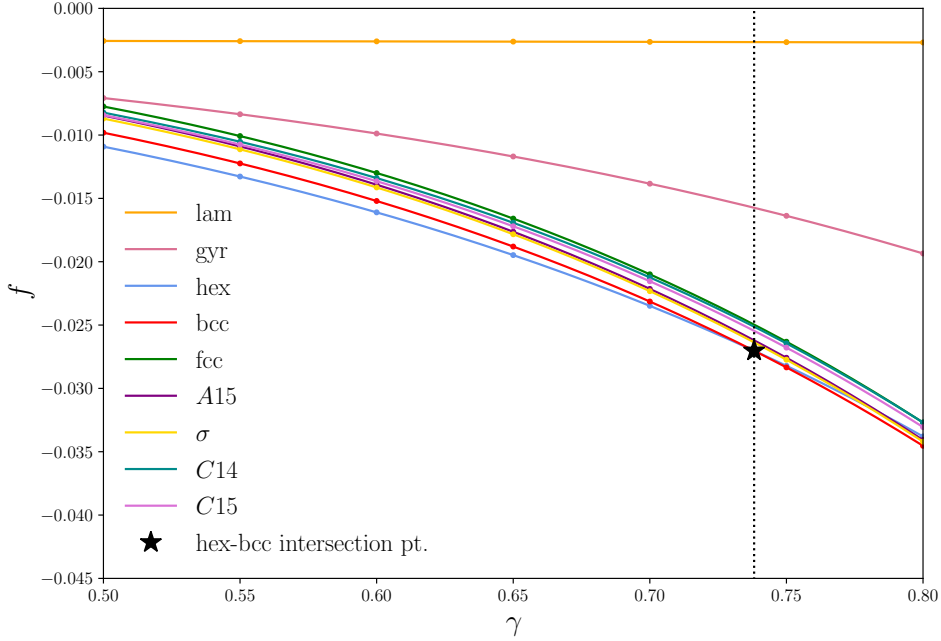


Figure 3.3: Plots of free energy densities f_p^* for each p in \mathcal{P} (points), computed at $\tau = -0.05$ using the algorithm described in section 3.1. Lines fit to numerical data using cubic spline interpolation algorithm. Intersection point (black star, dashed line) indicates the γ value where bcc becomes stable over hex, this point is calculated using a root finding algorithm.

cubic spline interpolation algorithm. We then compute the intersection point using a root finding algorithm. The calculated intersection point is indicated by a star in figure 3.3.

The final step is to interpolate between the set of boundary points in order to produce the final phase diagram. Figure 3.4 shows a small region of the phase diagram with γ between 0 and 0.5 and τ between -0.35 and 0. The set of intersection points between the lam and hex phases are shown, together with the boundary line between the two phases. This line is found using a cubic spline interpolation.

We can see from figure 3.4 that the lam-hex phase boundary line will intersect *either* the lam-gyr or hex-gyr boundary line at the bottom and the order-disorder transition line at the top. Once we've fitted lines to all of the boundaries in figure 3.2 we can find the intersection

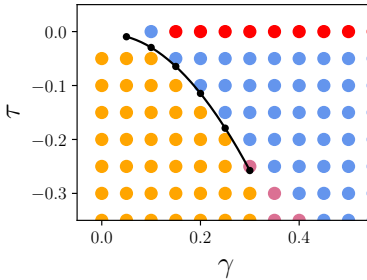


Figure 3.4: Close up of figure 3.2 showing intersection points and interpolated boundary line between lam and hex phases. Line is found using a cubic spline interpolation.

points between each line. We then choose the appropriate end points for each line. The reader may get the impression that this is a somewhat arbitrary choice. Indeed the precise location of triple points is difficult to obtain, and we can only ever approach it's precise location using the algorithm described here. For the purposes of this work, we accept this imprecision in the phase diagram. Once we have obtained all of the phase boundaries and their limits we can construct the phase diagram shown in figure 1.7.

We have explained how the minimum free energy associated with each phase in the set \mathcal{P} is calculated and described how that information is used to construct phase diagrams. In the next chapter we move onto a presentation of the results.

Chapter 4

Results and discussion

In this chapter we will analyse the phase diagram for Ginzburg-Landau theory with the form described in chapter 2, equation (2.16). In section 4.1 we begin by constructing the phase diagram for the Ohta-Kawasaki model and comparing that with the Landau-Brazovskii diagram. We then use the piecewise model to understand the differences between these diagrams, section 4.2. We discuss the modified Leibler model and the double-Gaussian SALR model in sections 4.3 and 4.4, respectively.

4.1 The Ohta-Kawasaki model

The phase diagram for the Ohta-Kawasaki model, equation (2.16) with quadratic coefficient (2.21), is shown in figure 4.1. We see immediately that none of the Frank-Kasper phases are present in this diagram. This is in contrast to the phase diagram for the Landau-Brazovskii model that was computed by McClenegan and Shi [53] (figure 1.7), in which the Frank-Kasper σ and A15 phases were both stable between the bcc and fcc phases.

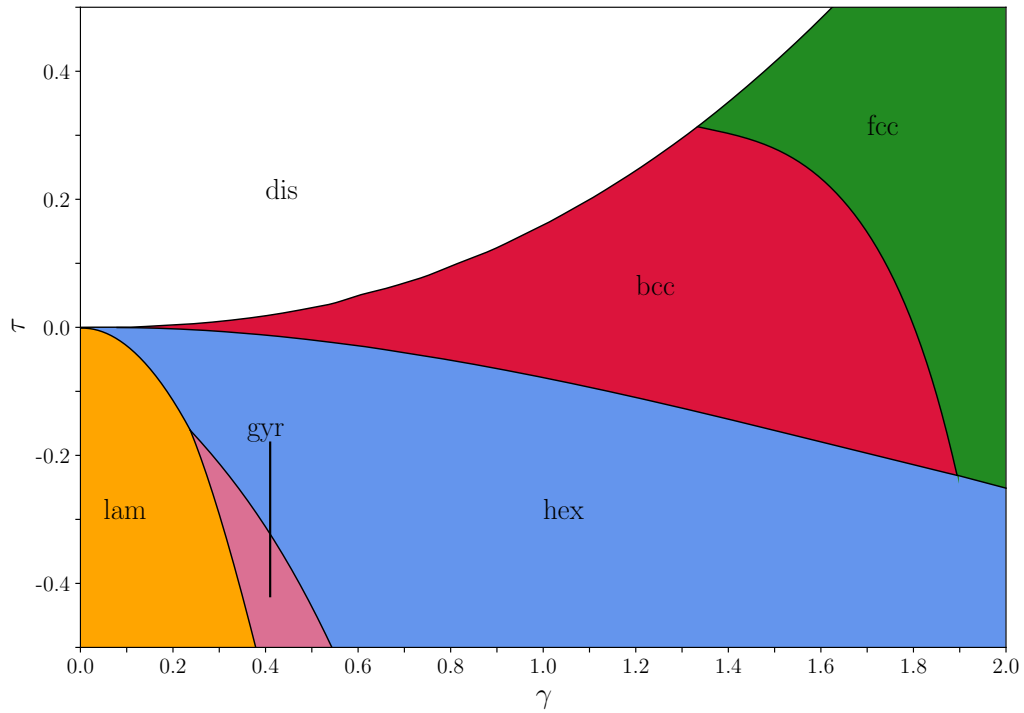


Figure 4.1: τ - γ phase diagram for the Ohta-Kawasaki model, equations (2.16) and (2.21). In this diagram the Frank-Kasper σ and a15 phases *do not* appear between the bcc and fcc phases, unlike the diagram computed by McClenagan and Shi [53] for the Landau-Brazovskii model, figure 1.7.

4.2 The piecewise interpolation model

We now use the piecewise interpolation (PW) model, equation (2.22), to help us understand the difference between the OK and LB phase diagrams. We begin by varying λ_1 in (2.22) while λ_2 is held fixed. This has the effect of changing the shape of $\Gamma_{\text{PW}}(q)$ for $q < 1$ only, and so we can isolate the effects of the *long wavelength* modes. These results are described in section 4.2.1. We then consider what happens when we hold λ_1 fixed and instead vary λ_2 , an analysis that allows us to understand the effects of the *short wavelength* ($q > 1$) modes. These results are discussed in section 4.2.2.

4.2.1 Effect of the long wavelength modes

We begin by isolating the effects of the long wavelength ($q < 1$) modes. Figure 4.2 shows three different λ_1 versus γ phase diagrams. The parameters τ and λ_2 are held constant in all of the diagrams, with $\tau = 0$ in all three and $\lambda_2 = 0$ (top), $\lambda_2 = 0.5$ (center), and $\lambda_2 = 1$ (bottom). λ_1 varies from 0 to 1 which leads to an *increase* in the free energy cost associated with the long wavelength modes as we move up the y -axis in each diagram.

The A15 phase is only stable in the top ($\lambda_2 = 0$) diagram. The σ phase is stable in some region of all three diagrams. The Frank-Kasper C14 and C15 phases were also included in the analysis but they were not found to be stable at any point. In all three diagrams we see that the region occupied by the complex σ and A15 phases *shrinks* as λ_1 increases. This suggests that increasing the free-energy cost associated with the long-wavelength modes *suppresses* the formation of these phases.

Figure 4.3 shows how the free energy densities of each of the spherical phases vary with λ_1 when all of the other parameters are held fixed: $\tau = 0.0$, $\gamma = 1.1$ and $\lambda_2 = 0$. The stable phase is indicated at each point by the background colour: purple for the A15 phase and yellow for σ . The x -axis correspond to the vertical line $\gamma = 1.1$ in the topmost plot of figure 4.2. The leftmost plot in figure 4.3 shows the *total* free energy density of each of the spherical phases, as defined in (3.4). The plot in the center shows the contribution from the non-local term, equation (3.15), and the rightmost plot shows the contribution from the

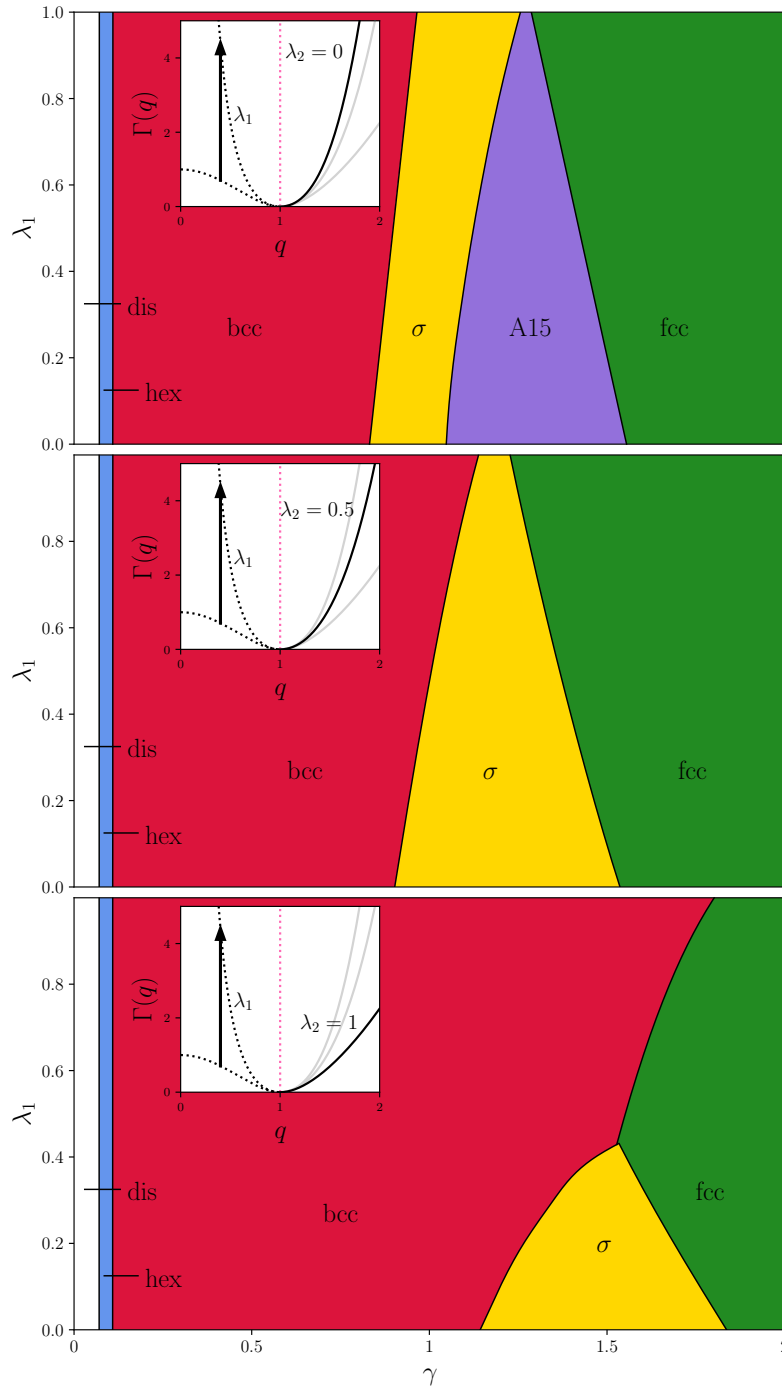


Figure 4.2: λ_1 versus γ phase diagram for the Piecewise model with $\tau = 0$ (all) and $\lambda_2 = 0$ (top), $\lambda_2 = 0.5$ (center), $\lambda_2 = 1$ (bottom). Inset shows how the shape of $\Gamma_{PW}(q)$ changes as λ_1 increases.

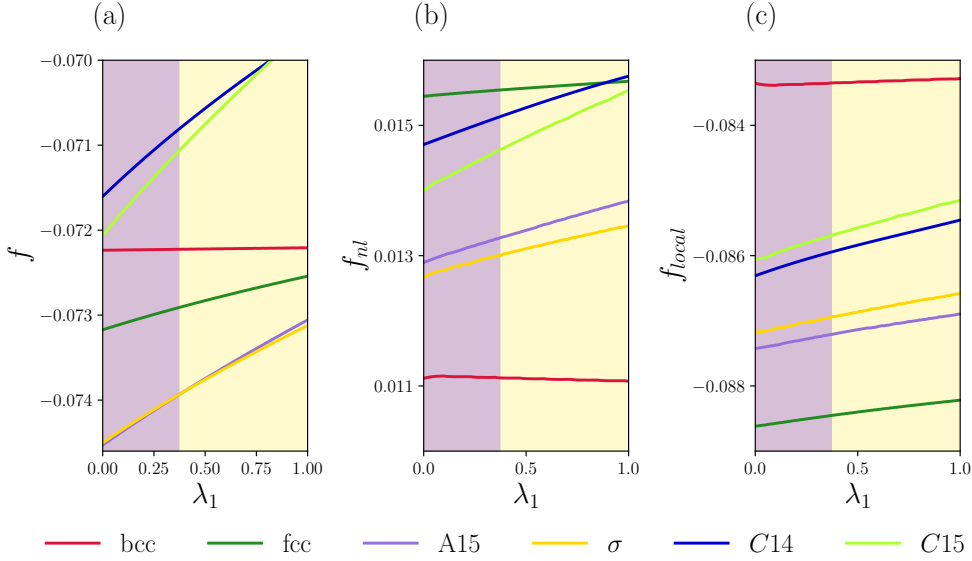


Figure 4.3: (a) Total free energy density, f , (b) non-local free energy density, f_{nl} , and (c) local free energy density f_{local} for each of the spherical candidate phases (bcc, fcc, A15, σ , C14 and C15), plotted against λ_1 , with $\tau = 0$, $\gamma = 1.1$, $\lambda_2 = 0$. In all plots the background colour indicates the phase that is stable in that region of phase space: a15 (purple), and σ (yellow).

local term, which is defined as:

$$f_{local} = \frac{1}{v} \int d\mathbf{x} \left\{ \frac{\tau}{2} \phi(\mathbf{x})^2 - \frac{\gamma}{3!} \phi(\mathbf{x})^3 + \frac{1}{4!} \phi(\mathbf{x})^4 \right\}. \quad (4.1)$$

In plot (a) we see that the slope of the free energy density of the bcc phase is almost flat, while the other phases have larger, positive slopes. This indicates that the bcc phase is relatively insensitive to the shape of $\Gamma(q)$ when $q < 1$. The free energy cost associated with the formation of the remaining phases increases as λ_1 increases, with the fcc phase less sensitive than the A15, σ , C14 and C15 phases. If we imagine extrapolating the lines shown in (a) out to larger λ_1 values, we might expect that the fcc and eventually the bcc phase would become stable. In plot (b) we see that the non-local part of the free energy density increases with λ_1 for the fcc, A15, σ , C14, and C15 phases, an unsurprising result. Plot (c) shows that the *local* part of the free energy density also increases for all of these phases.

Furthermore, (b) and (c) show that *both* terms are approximately flat for the bcc phase.

In order to understand the effect that the shape of $\Gamma(q)$ has on the free energy densities of the spherical phases, we next look at their Fourier spectra. These are shown in the top plots of figure 4.4. The height of the peak associated with wavevector q in these plots is given by:

$$I_q = \sum_{|\mathbf{q}|=q} \left| \tilde{\phi}(\mathbf{q}) \right|^2, \quad (4.2)$$

where $\tilde{\phi}_p(\mathbf{q})$ is the Fourier transform of the phase p that has been optimized at the point $\tau = 0$, $\gamma = 1.1$ in the LB model ($\lambda_1 = 0$, $\lambda_2 = 0$). The bottom plots in figure 4.4 show how each peak in the Fourier spectra contributes to the total non-linear free energy density:

$$f_{nl}(q) = \frac{1}{2} \Gamma(q) I(q). \quad (4.3)$$

Each peak in these bottom plots is normalized by the total non-linear free energy density for this phase, f_{nl} calculated at the point $\tau = 0$, $\gamma = 1.1$ in phase space.

Figure 4.4 can provide us with some insight into the relationships we saw in figure 4.3 between the free energy densities and λ_1 . Starting with the bcc phase, (a), the top plot reveals that the *longest* wavelength mode occurs at $q = 0.98$, very close to $q = 1$. The bottom plot shows that this main peak contributes only a small fraction (about a tenth) of the total non-local free energy density. It makes sense then that varying the free energy cost associated with the long-wavelength peaks would not have a significant impact on the bcc phase. Looking at fcc (b) next, we see that this phase has *two* peaks close to $q = 1$, at $q = 0.93$ and $q = 1.08$. Together these two peaks account for about 68% of the total non-local free energy density, which is in sharp contrast to the situation for the bcc phase. The minimization of the free energy density of the fcc phase is constrained by a competition between the positions of these two peaks. Increasing λ_1 may decrease the height of the first peak or cause it to move closer to $q = 1$, either way we can understand why the fcc is relatively more sensitive to λ_1 than the bcc phase was. Similarly, the Frank-Kasper A15 (c), σ (d), C14 (e), and C15 (f) phases all have multiple peaks around $q = 1$. It naturally follows that these phases have a stronger dependence on the long-wavelength part of $\Gamma(q)$. The short wavelength modes are relatively more important for the C15 phases than for the A15, σ , and C14 phases, and this accounts for the fact that C15 is the most sensitive of the four phases to changes in λ_1 .

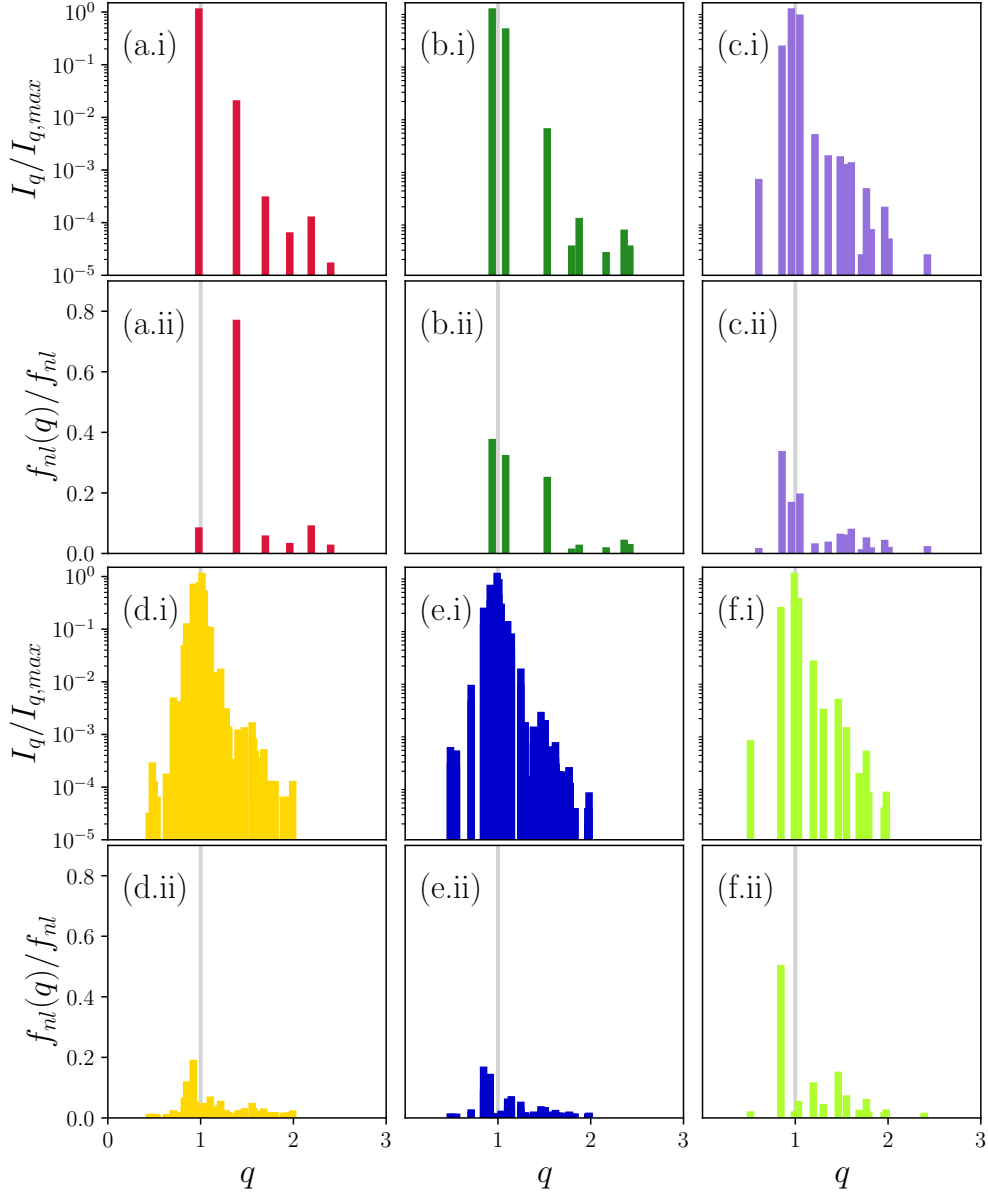


Figure 4.4: Plots of Fourier modes $I(q)$ defined in equation (4.2) (top plot, logarithmic axis), and the fractional contribution of each mode to the non-local free energy density (bottom plot) for the (a) bcc, (b) fcc, (c) A15, (d) σ , (e) C14, and (f) C15 phases. Each of the spectra represents the optimized order parameter field for its respective phase, computed using the LB model with $\tau = 0.0$ and $\gamma = 1.1$

The particular shape of the Fourier spectrum influences how sensitive each phase is to λ_1 . The complex phases in particular have *more* long-wavelength peaks, and so they are the most sensitive to changes in the shape of the quadratic coefficient for $q < 1$. The following argument may provide some intuition as to why: the *longest* wavelength mode that appears in each of the plots in figure 4.4 is associated with the *size of the unit cell*: $q_{min} = 2\pi/l$, where l is the largest dimension of the unit cell. Each phase must also have one or more peaks associated with the length scales of the spheres. In the case of the bcc phase we see from figure 4.4 that there is one dominant peak (note that the y -axis of the Fourier spectra plots uses a logarithmic scale). This indicates that the sphere sizes are roughly commensurate with the unit cell size. In contrast, the fcc phase and the Frank-Kasper phases all have multiple dominant peaks, indicating that the sphere sizes are smaller than the box size., and (in the case of the complex phases) that the spheres are not all the same size.

4.2.2 Effect of the short wavelength modes

We now turn our attention to the effects of the short-wavelength ($q > 1$) modes. Figure 4.5 shows three λ_2 versus γ phase diagrams constructed by holding τ and λ_1 fixed, with $\tau = 0$ in all three diagrams and $\lambda_1 = 0$ (top), $\lambda_2 = 0.5$ (center), and $\lambda_1 = 1.0$ (bottom). Note that an increase in λ_2 corresponds to a *decrease* in the free energy cost associated with the short-wavelength modes. This is illustrated by the insets in figure 4.5, and is different from the situation with λ_1 .

The A15 phase is stable in a small region in both the top and centre plots and nowhere in the bottom plot. The σ phase is stable in some region of all three plots. In each of the plots the bcc phase becomes more stable as λ_2 is increased. The behaviour of the σ phase is more complicated. In the top plot we observe that the σ region appears to overtake both the A15 and fcc regions as λ_2 is increased. Conversely, in the bottom plot the fcc appears to become favoured over σ as λ_2 increases. The centre plot demonstrates both behaviours.

Figure 4.6 shows plots of the total free energy density for all the spherical candidate phases, as well as contributions from the local and non-local terms.

In 4.6 (a) we see that *all* of the spherical phases are strongly dependent on the shape of

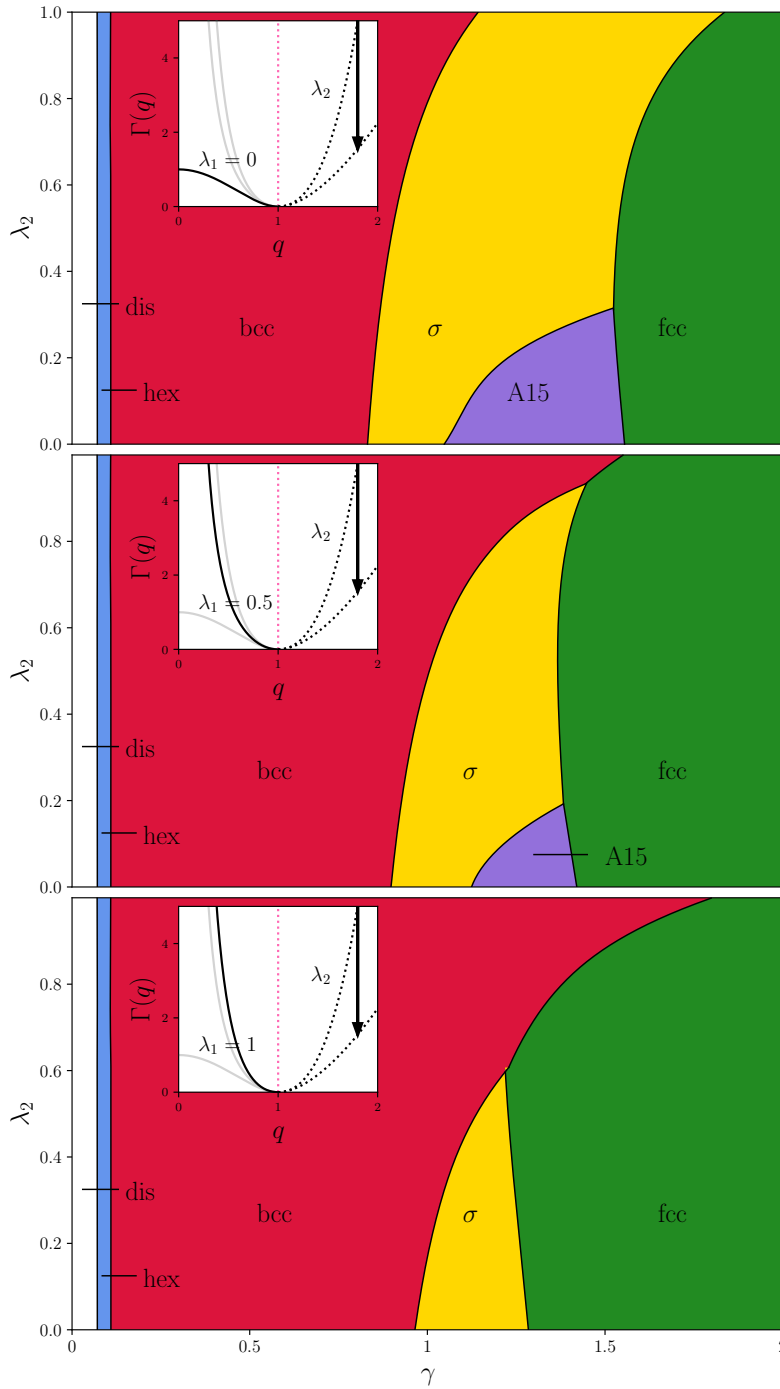


Figure 4.5: λ_2 versus γ phase diagram for the Piecewise model with $\tau = 0$ (all) and $\lambda_1 = 0$ (top), $\lambda_1 = 0.5$ (center), $\lambda_1 = 1$ (bottom). Inset shows how the shape of $\Gamma(q)$ changes as λ_2 increases.

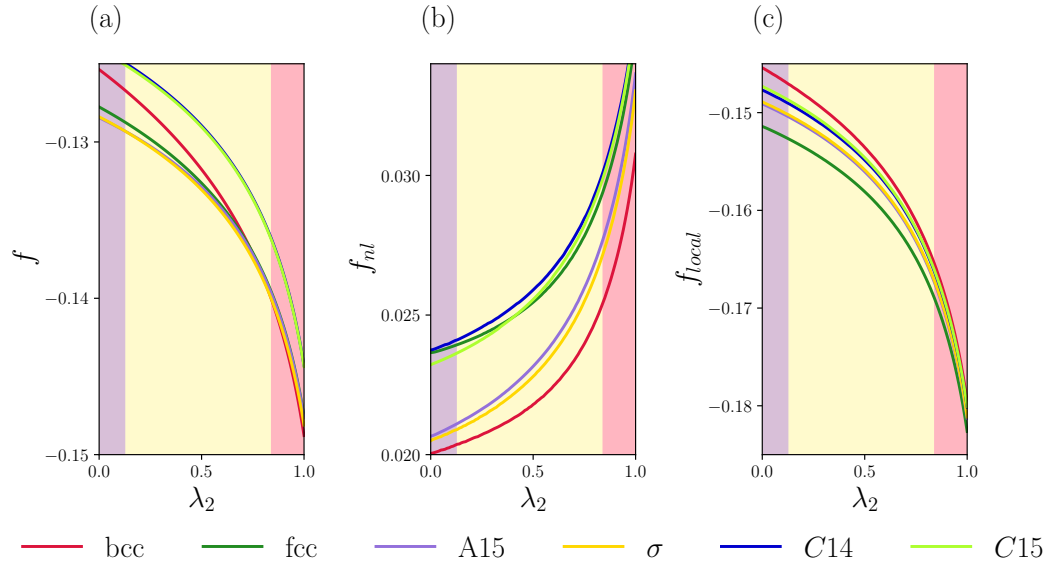


Figure 4.6: (a) Total free energy density, f , (b) non-local free energy density, f_{nl} , and (c) local free energy density f_{local} for each of the candidate spherical phases (bcc, fcc, A15, σ , C14, and C15) plotted against λ_2 , with $\tau = 0$, $\gamma = 1.25$, $\lambda_1 = 0.5$. In all plots the background colour indicates the phase that is stable in that region of phase space: bcc (red), A15 (purple), and σ (yellow).

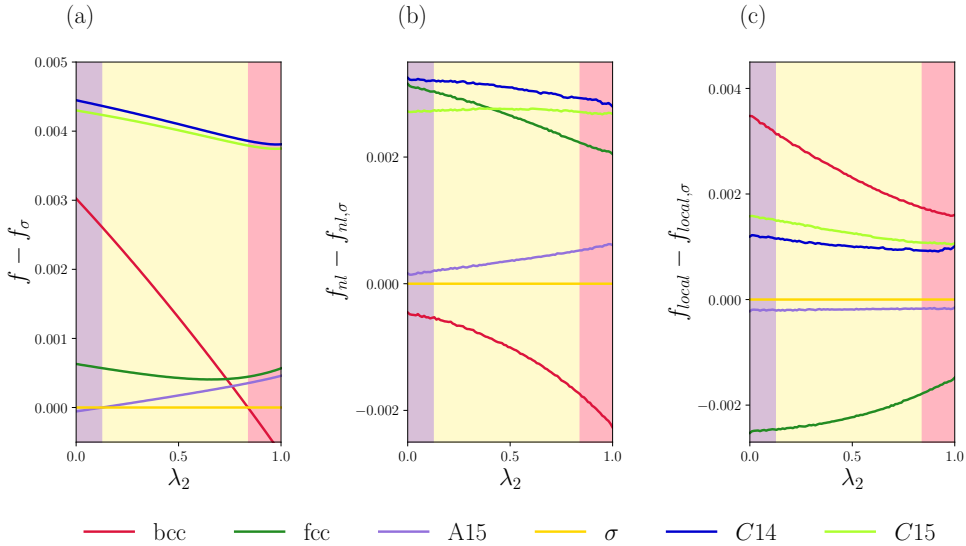


Figure 4.7: Plots of free energy densities shown in figure 4.6, with the σ -phase values subtracted off. All parameters are the same between the two figures.

the right-hand side of $\Gamma(q)$ ($q > 1$). The total free energy density always decreases as λ_2 increases. Surprisingly, the non-local free energy density (b) actually *increases* when we decrease the cost of the short-wavelength modes by increasing λ_2 . Plot (c) shows that the overall decrease in free energy density is driven by a decrease in the local term.

Figure 4.6 doesn't give us much information about the effect of λ_2 on the relative free energy densities of the various phases. The next plot, figure 4.7., shows the same free energy densities for the bcc, fcc, A15, C14, and C15 phases, this time calculated relative to their values in the σ phase.

Figure 4.7 (a) shows that the free energy density of the bcc phase decreases rapidly relative to that of the σ phase as λ_2 increases. Both f_{nl} , plot (b), and f_{local} , plot (c), contribute to this trend. An increase in λ_2 appears to *suppress* the A15 phase relative to the σ phase. This suppression appears to be driven primarily by the non-local free energy density shown in plot (b). On the other hand, increasing λ_2 appears to enhance both C14 and C15 relative to σ . Finally, the relationship between the free energy densities of the σ and fcc phases is more complicated. Plot (b) shows that f_{nl} for the fcc phase decreases relative to the σ phase, but

plot (c) shows that f_{local} increases. In plot (a) we see the effect of the competition between these two terms, the total free energy density of the fcc phase has a minimum that appears around $\lambda_2 = 0.7$. These trends agree qualitatively with the phase behaviour observed in figure 4.5.

Figure 4.8 shows how the Fourier spectra for the optimized spherical packing phases change when λ_2 is increased from $\lambda_2 = 0$ (top plots) to $\lambda_2 = 1$ (bottom plots). In all four plots the remaining parameters are fixed at $\tau = 0$, $\gamma = 1.25$ and $\lambda_1 = 0.5$. Plots therefore correspond to the bottom and top points of the vertical line $\gamma = 1.25$ in the middle phase diagram of figure 4.5.

Comparison of the top and bottom plots for each phase in figure 4.8 shows both the appearance of new peaks and an increase in the height of existing peaks with $q > 1$ when λ_2 is increased. This is the expected behaviour, of course, since an increase in λ_2 corresponds to a decrease in the free energy cost associated with the short wavelength modes.

We refer back to figure 4.6 where we observed that the total free energy density decreased with increasing λ_2 , and that this decrease was driven by the local term in f . We can get some insight into this trend by considering again the expressions for the different contributions to the total free energy density. It is clear that the non-local free energy density, equation (3.15), is always positive. This term always associates a free energy *cost* to any Fourier peak, $\tilde{\phi}(\mathbf{q})$ (unless $q = 1$). As for the local free energy density, let's write equation (4.1) in terms of the Fourier components $\tilde{\phi}_{ijk}$ and take $\tau = 0$:

$$f_{local} = \sum_{\mathbf{q}, \mathbf{q}', \mathbf{q}''} \left(-\frac{\gamma}{3!} + \frac{1}{4!} \sum_{\mathbf{q}'''} \tilde{\phi}_{\mathbf{q}'''} \right) \tilde{\phi}_{\mathbf{q}} \tilde{\phi}_{\mathbf{q}'} \tilde{\phi}_{\mathbf{q}''}. \quad (4.4)$$

Both the cubic and quartic terms pick out *combinations* of peaks. In other words, each of these terms will increase in magnitude when new peaks are added. The extent to which the cubic term (always negative) is able to 'win out' over both f_{nl} and the quartic term depends on the value of γ , but at any rate we can connect the increase in amplitude and number of short-wavelength peaks that we observed in figure 4.8 with the change in local free energy density that we saw in figure 4.6.

Our investigation of the short-wavelength modes reveals a couple of trends: decreasing the free energy cost of these modes promotes the formation of the bcc phase and suppresses the

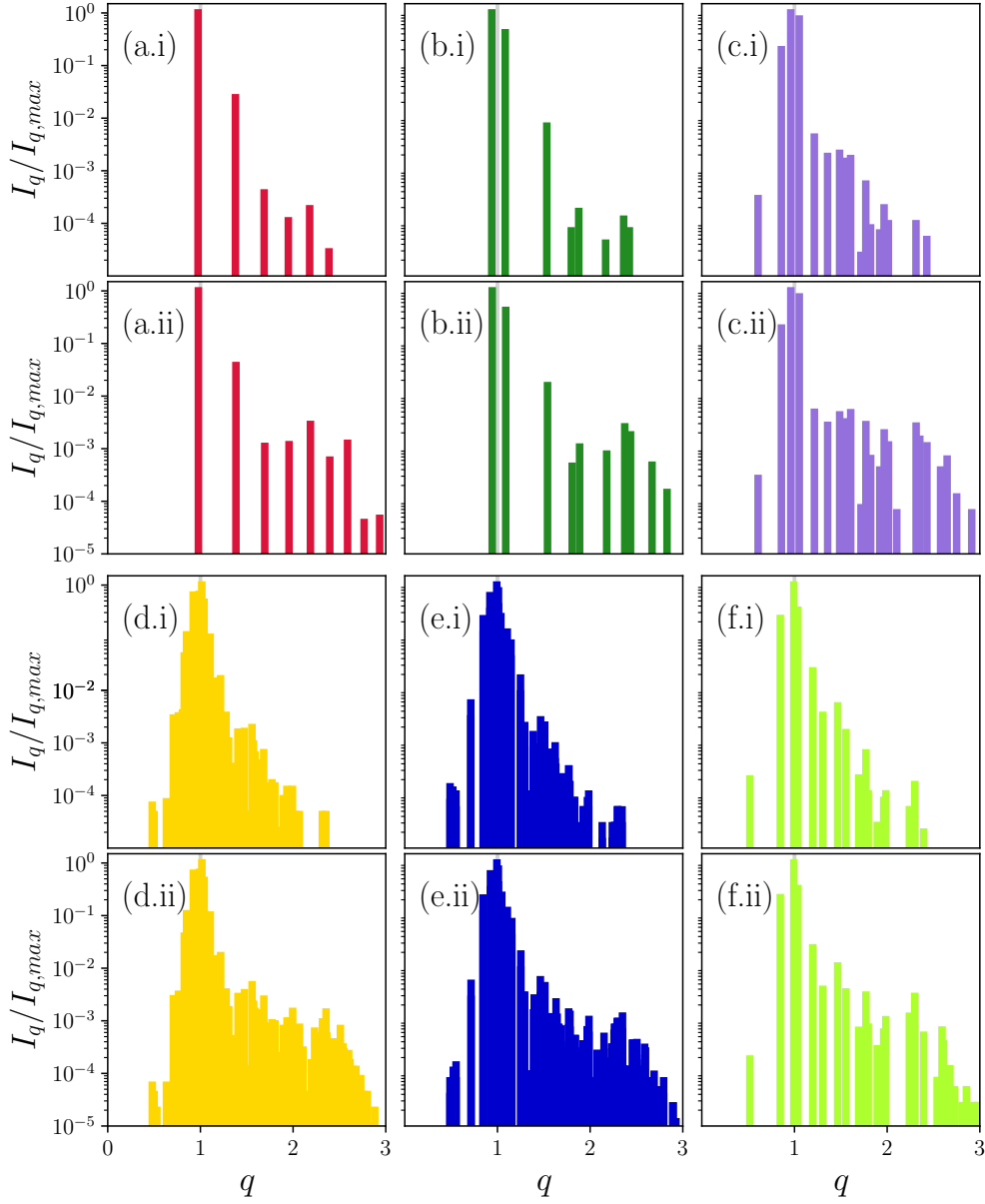


Figure 4.8: Plots of Fourier peaks for (a) bcc, (b) fcc, (c) A15, (d) σ , (e) C14, and (f) C15 phases. Top plot in each pair shows intensities at $\lambda_2 = 0$ and bottom plot shows intensities at $\lambda_2 = 1$. Other parameters are fixed: $\tau = 0.0$, $\gamma = 1.25$, $\lambda_1 = 0.5$.

a15 phase. Upon closer inspection our analysis reveals that the dependence of the phase diagram on the short-wavelength modes is the result of an interplay between the different terms in the free energy density.

4.3 Modified Leibler theory

We turn now to the modified Leibler (ML) model described in section 2.3. The functional form for the quadratic coefficient, $\Gamma_{\text{ML}}(q)$ is obtained by scaling equation (2.34) to match the expression given in equation (2.12). The parameter ϵ is a measure of the segment asymmetry of the diblocks. Increasing ϵ is expected to stabilize the Frank-Kasper σ and A15 phases based on the literature, see [43, 29, 30, 31]. Figure 4.9 shows how the shape of the coefficient Γ_{ML} that we derived depends on the two parameters, the composition fraction, f , and the asymmetry parameter, ϵ .

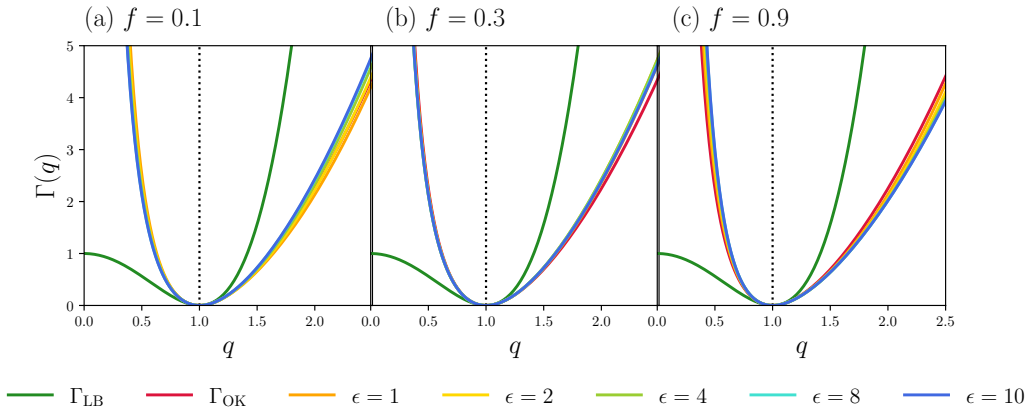


Figure 4.9: Plots showing how the shape of the quadratic coefficient for the modified Leibler theory, $\Gamma_{\text{ML}}(q)$, varies with ϵ when (a) $f = 0.1$, (b) $f = 0.3$, and (c) $f = 0.9$. The coefficients for the LB and OK models are included in all plots for comparison.

We see that the shape of $\Gamma_{\text{ML}}(q)$ changes very little in any of the three figures. We also see that the shape of this function looks very similar to the shape of Γ_{OK} , and here we note that the OK model was originally derived as an approximation to Leibler's original ($\epsilon = 1$) theory [50]. Looking at the shape of Γ_{ML} in figure 4.9 (a), we see that there is some dependence of the shape of ϵ . This plot shows that the free energy cost associated with the short-wavelength modes increases slightly and the cost associated with the long-wavelength modes decreases slightly when ϵ is increased and $f = 0.1$. In figure 4.9 (c), by contrast, we can make out the reverse behaviour.

What does the shape of Γ_{ML} tell us about the phase behaviour of our ML theory? Well the

shape is very similar to Γ_{OK} , and we saw in section 4.1 that this shape was associated with a suppression of the complex phases. For $f = 0.1$ we see that increasing ϵ does slightly alter the shape in a way that should correspond to increased stability for the complex phases per our analysis in sections 4.2.1 and 4.2.2. In a 2014 paper by Xie et. al. [43], for example, the authors found that increasing ϵ corresponded to an increased region of stability for the complex phases when $f < 0.5$, so our results are somewhat consistent with the literature. When $f = 0.9$ we see that increasing ϵ changes the shape of Γ_{ML} in a way that is expected to suppress the complex phases. This result is also consistent with Xie's result. However the change in shape that we observe is not large. The function still closely resembles the OK coefficient for all values of f and ϵ . Looking at the shape of Γ_{ML} that we derived, we can conclude that increasing the asymmetry parameter ϵ does not stabilize the complex phases within the ML theory.

Figure 4.10 shows the ϵ versus γ phase diagram constructed for the ML theory with $\tau = 0$ and $f = 0.1$ held fixed. These values are thought to be the most likely candidates for stabilizing the complex phases in this model based on the shape of the quadratic coefficient (figure 4.9).

We see that no complex phases appear between the fcc and bcc phases in this diagram. We can conclude that our ML theory does not successfully predict the onset of the complex phases as a function of the asymmetry parameter ϵ . Possible shortcomings of this theory are discussed in chapter 5.

4.4 The SALR potentials

The final set of quadratic coefficients considered in this work are those derived from the density functional theory for short-range attractive, long-range repulsive (SALR) pair potentials, as described in section 2.4. In this section we consider two such theories, the double-Gaussian (introduced in section 2.4.1) and the step potential (section 2.4.2). We also discuss work by Jiayu Xie and Cameron Burns [60], who used the DFT to construct phase diagrams for these potentials. We compare those results with the ones presented here.

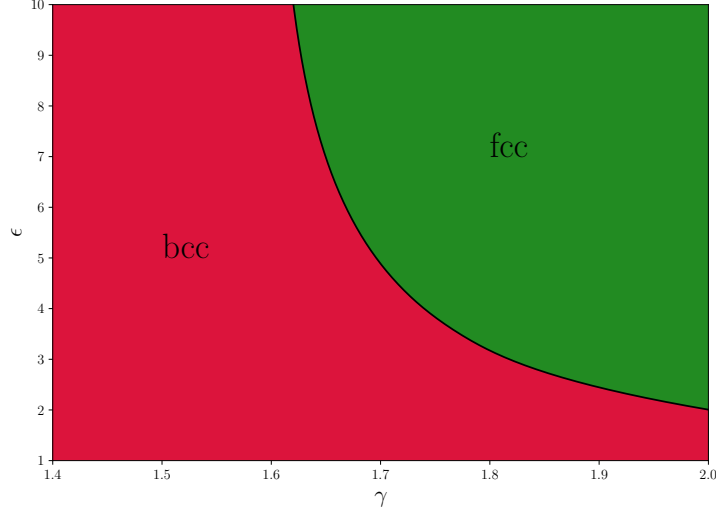


Figure 4.10: γ vs. ϵ phase diagram for the modified Leibler theory with $\tau = 0$ and $f = 0.1$. The Frank Kasper σ phase is expected to appear between the bcc and fcc phases when they are stable. In this diagram we see that these phases do not appear for this range of ϵ values.

4.4.1 The double-Gaussian potential

The functional form of the double-Gaussian coefficient is given by scaling equation (2.45) to match equation (2.42). Figure 4.11 shows how the shape of the scaled quadratic coefficient, $\Gamma_{\text{DG}}(q)$, varies with the ratio of length scales, α .

Beginning with an analysis of the long wavelength modes, we see from figure 4.11 that decreasing α has the effect of *suppressing* these modes. Increasing α therefore favours the formation of the complex phases, according to our analysis in 4.2.1. Of course, α also impacts the shape of Γ_{DG} for short wavelengths. Looking at the right hand ($q > 1$) side of figure 4.11, we see that increasing α also increases the cost of the short wavelength modes until $q \approx 2.5$, at which point there is a crossover. We see that increasing α causes the value of the quadratic coefficient to decrease past this point. Applying the results from section 4.2.2, that suppressing short-wavelength modes should promote the complex phases, is therefore more complicated. To summarize, increasing α should have the effect of promoting the formation of the complex phases based on the shape of the quadratic coefficient for $q \lesssim 2.5$. For larger

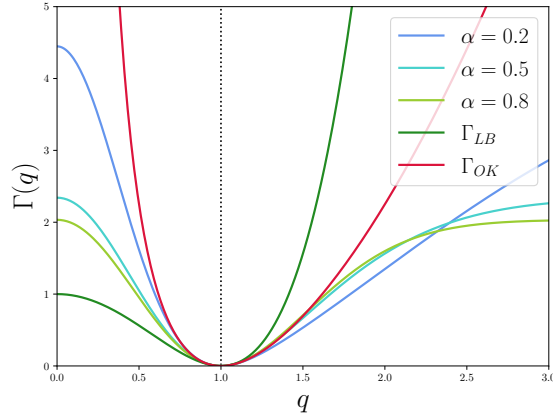


Figure 4.11: Shape of quadratic coefficient for the double-Gaussian SALR theory, Γ_{DG} , for different values of the parameter α . Plots of the LB and OK coefficients are included for comparison.

values of q , increasing α causes Γ_{DG} to decrease, an effect which we expect to suppress the complex phases. There is thus some ambiguity about the expected phase behaviour of this model based on the analysis we have done so far.

Figure 4.12 shows a γ vs. α phase diagram for the double-Gaussian model with $\tau = 0$ held fixed. This phase diagram reveals that increasing α has the effect of stabilizing the σ phase. The result that an increase in α stabilizes the complex phases means that the short wavelength modes close to $q = 1$ are more important for determining the phase behaviour of the theory than the larger values of q are. This makes sense based on the Fourier spectra from figures 4.4 and 4.8, which show that the spectrum rapidly decays as q increases.

We developed the Ginzburg-Landau theory based on the SALR model so that we could attempt to gain an intuition about the physical mechanisms that control the shape of the quadratic coefficient. Our DG model has a single parameter, α , that drives the formation of the complex σ phase and has a physical interpretation: α is the ratio of attractive to repulsive length scales in equation (2.44). Figure 2.3 shows how the real-space interaction potential, $w(r)$ in equation (2.44), varies as a function of α . We see that increasing the value of α effectively *flattens* this potential, making the attractive well shallower and causing the

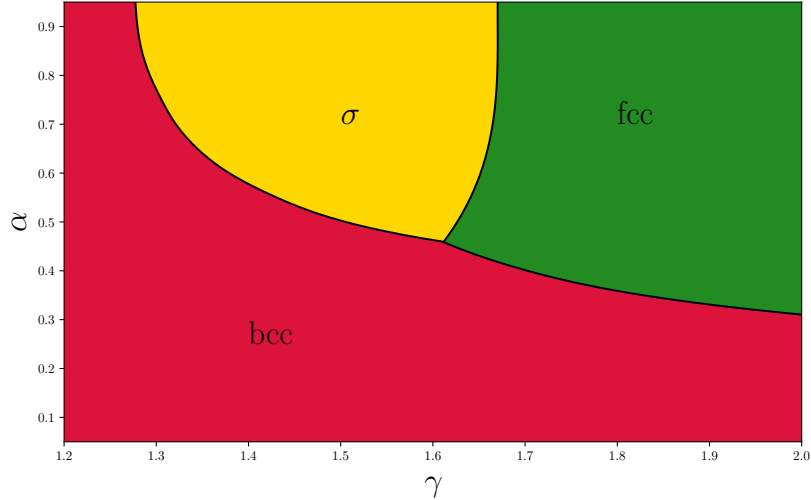


Figure 4.12: γ vs. α phase diagram for the DG model with $\tau = 0$ calculated using the Ginzburg-Landau theory.

function to flatten to zero more quickly. The results of this section show us that this flattening behaviour is connected with the formation of the Frank-Kasper σ phase.

4.4.2 The step potential

The quadratic coefficient for the step potential is given by equation (2.49), scaled using equation (2.42). Figure 4.13 shows how the shape of $\Gamma_{step}(q)$ changes with each of the parameters in the theory.

In plots 4.13 (a) and (b) we see that decreasing the range of the attractive part of the potential, σ_1 , changes the shape of Γ_{step} in a way that suggests the complex phases will be favoured. In (c) and (d) we see that decreasing the range of the long-range repulsive part of the potential, σ_2 , favours these phases. Lastly, in plots (e) and (f) we see that decreasing the maximum amplitude of the repulsive part of the potential, B , favours the complex phases. Overall, weaker interactions with a shorter-range are more favourable to the formation of the Frank-Kasper phases. This appears to agree with the results from the double-Gaussian potential. Figure 2.3 shows that increasing α in the DG model decreases both the magnitude

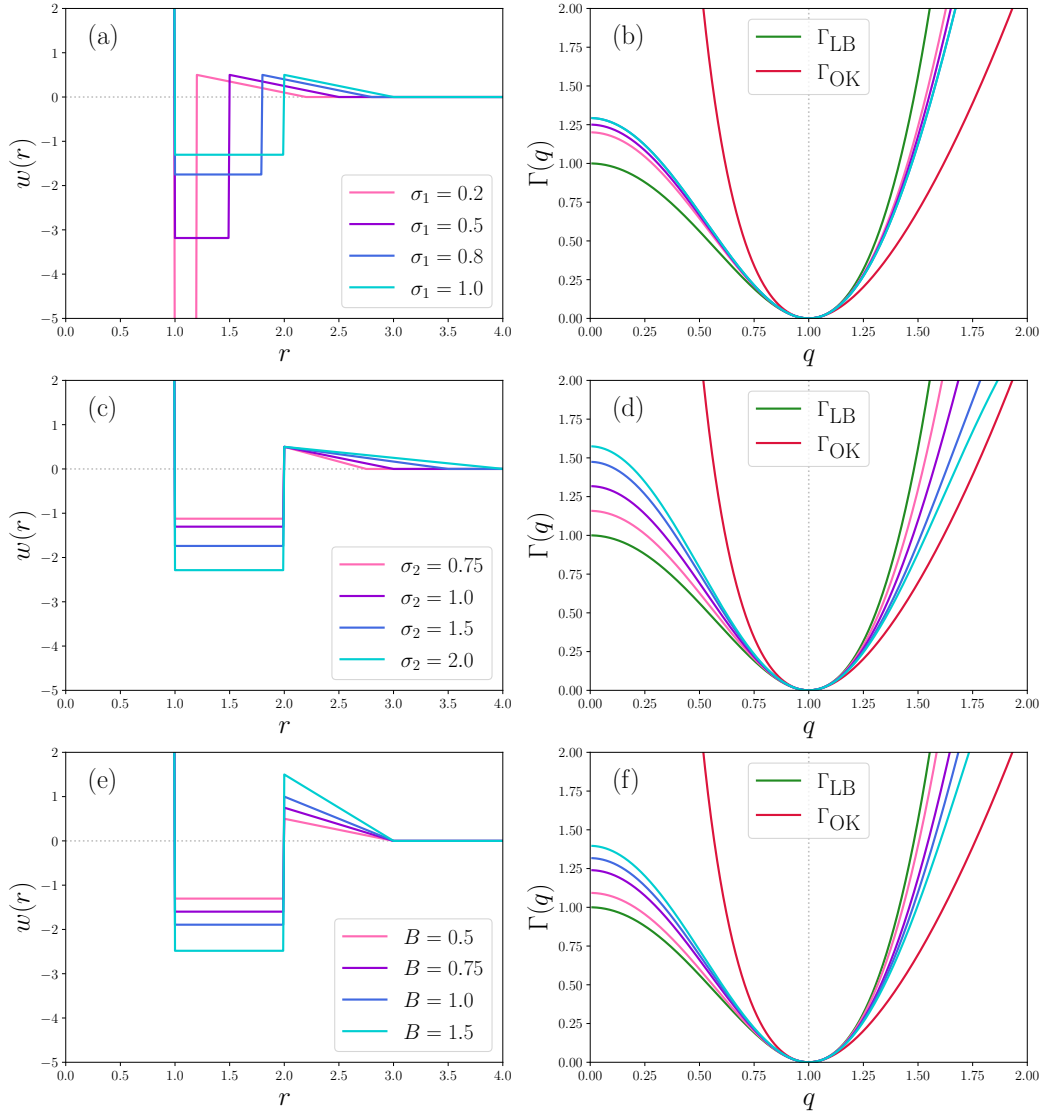


Figure 4.13: Plots of the real-space potential $w_{step}(r)$ (left column) and quadratic coefficient, $\Gamma_{step}(q)$ (right column). In (a) and (b) we vary σ_1 , keeping $\sigma_2 = 1$ and $B = 1$ fixed. In (c) and (d) we vary σ_2 , keeping $\sigma_1 = 1$ and $B = 1$ fixed. In (e) and (f) we vary B , keeping $\sigma_1 = 1$ and $\sigma_2 = 1$ fixed.

and range of the potential, and we saw in figure 4.12 that this favours the formation of the σ phase.

4.4.3 DFT results

As mentioned in the introduction, our colleagues Jiayu Xie and Cameron Burns, supervised by Dr. An-Chang Shi, performed DFT calculations to search for the σ , A15, C14, and C15 Frank Kasper phases using the free energy functional in equation (2.37). They considered three different SALR potentials. The first was the double-Yukawa (DY) potential used by Pini [58], the second was the double-Gaussian potential, equation (2.44), and the third was the step potential, equation (2.48). Figure 4.14 shows the phase diagrams they computed for each of these theories.

Xie and Burns found that no complex phases were stable in the double-Yukawa model, figure 4.14 (a). They observed the σ phase (orange) in diagrams (b) and (c) (the double-Gaussian potential) and (d) and (e) (the step potential). They also found that the A15 phase (lime green) was stable in diagram (e). The C14 and C15 phases were not stable in any of the models considered. Diagrams (b) and (c) were constructed using (b) $\alpha = 1/1.667 \approx 0.6$ and (c) $\alpha = 1/1.4 \approx 0.71$. The stability of the σ phase in both of these diagrams, and the fact that the region of stability is larger in the second diagram, is consistent with our results.

Figure 4.15 shows the shapes of the quadratic coefficients associated with each of the potentials considered by Xie and Burns, using the scaling described in equation (2.42).

The quadratic coefficients in this figure change shape in a way that has been demonstrated to favour the formation of the complex phases as we move from (a) to (e).x The Yukawa potential (diagram (a) in figure 4.14) has both the highest cost for the long-wavelength modes and the lowest cost for the short-wavelength modes, making it the most similar to the OK theory. The result of this is that no complex phases are stable in this theory. The second step potential, Step (2), is the most similar to the shape of the LB model. The phase diagram for this potential is shown in figure 4.14 (e). We see that both the σ and A15 phases are stable in this model. The calculation of Xie and Burns shows that the same mechanisms that stabilize the complex phases in the GL theory also work in the DFT model

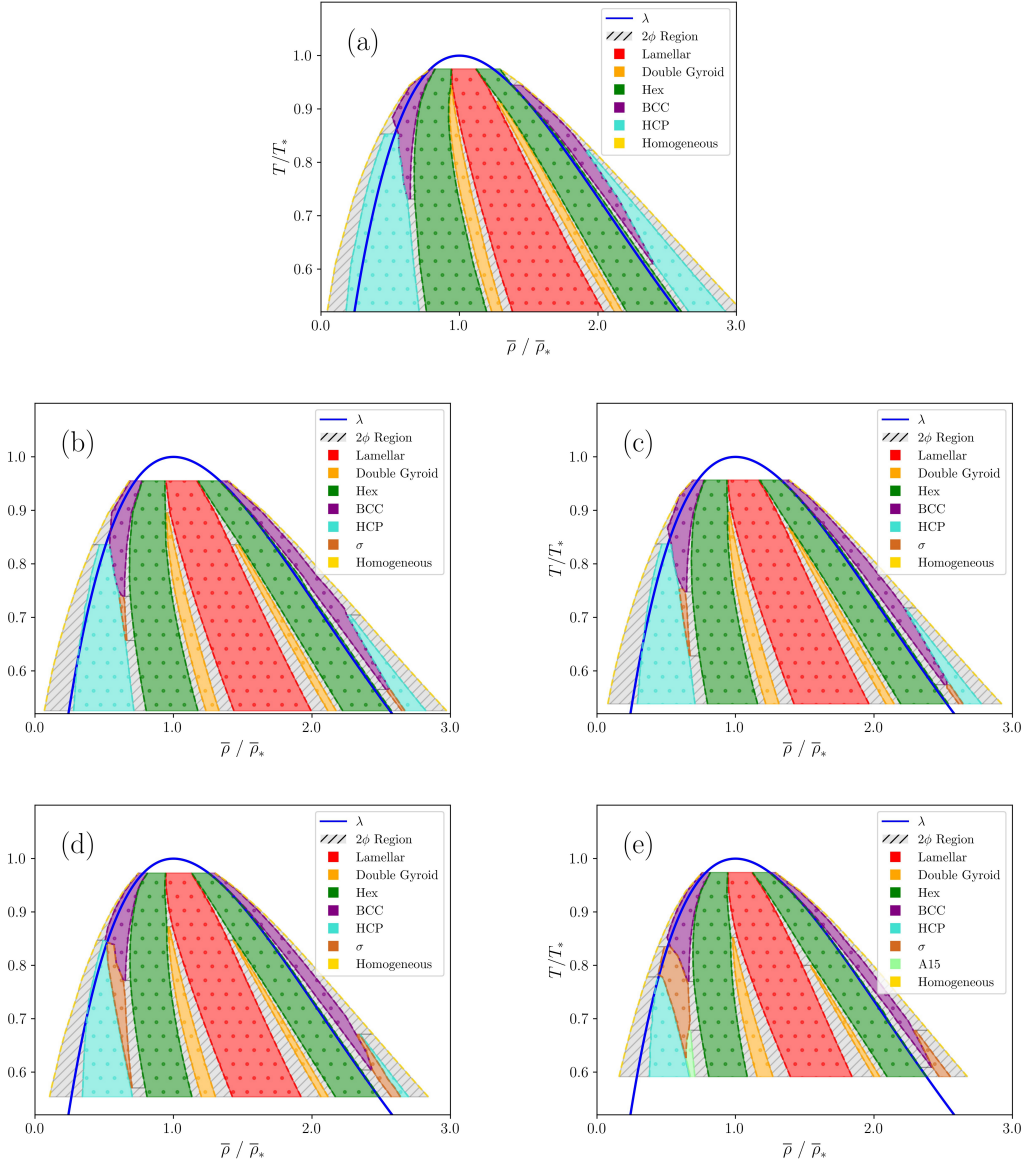


Figure 4.14: Phase diagrams computed by Xie, Burns, and Shi. Reprinted from [60]. Plot (a) shows the phase diagram computed for the double-Yukawa model used by Pini [58], with $B = 1.0$, $z_1 = 1.0$ and $z_2 = 0.5$. Diagrams (b) and (c) were computed using the double-Gaussian model considered in this work with (b) $\alpha = 0.6$ and (c) $\alpha = 0.71$. Diagrams (d) and (e) were constructed using the step potential described by Zhuang and Charbonneau with (d) $B = 1.0$, $\sigma_1 = 1.5$, $\sigma_2 = 3.0$ and (e) $B = 0.5$, $\sigma_1 = 1.0$, $\sigma_2 = 1.5$ [59].

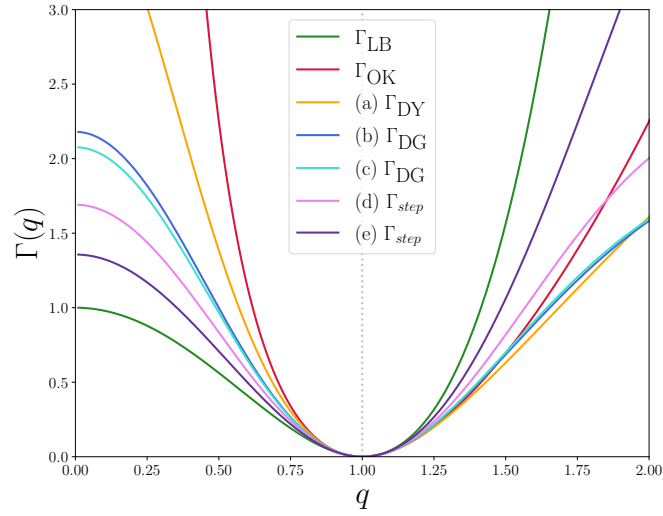


Figure 4.15: Quadratic coefficients corresponding to each of the 5 diagrams shown in figure 4.14. Yukawa (a), Gauss (1) (b), Gauss (2) (c), Step (1) (d) and Step 2 (e). Figure courtesy of Xie, Burns, and Shi [60].

of interacting spheres.

Chapter 5

Conclusion

In this work we studied the simplest Ginzburg-Landau theories that one can use to describe the formation of ordered phases. These theories have a generic form given by equation (1.8), with a local term always given by the quartic polynomial in equation (1.9) and a non-local term of the form presented in (1.10). We have thoroughly explored how the shape of the quadratic coefficient in equation (1.10) influences the stability of the Frank-Kasper spherical packing phases. Building on the work of McClenegan and Shi [53], which demonstrated the stability of the Frank-Kasper σ and A15 phases in the Landau-Brazovskii model, we showed that these phases *do not* appear in the Ohta-Kawasaki model. These models differ only in the shape of the quadratic coefficient. To understand why the phase diagrams look different we constructed our piecewise interpolation model and used it to isolate the effects of the long and short wavelength modes on the stability of the complex phases. We discovered that the formation of complex phases is suppressed relative to the other spherical phases when the free energy cost associated with the long wavelength modes increases. We found that decreasing the cost of the short wavelength modes also suppresses the complex phases.

Hoping to connect these results with a physical mechanism that is known to govern the formation of the complex phases in block copolymer systems, we derived a Ginzburg-Landau theory for diblock copolymers with segment asymmetry. Despite being responsible for the formation of the Frank-Kasper σ and A15 phases in both experimental systems and SCFT

calculations, we saw that the conformational asymmetry parameter in this theory did not cause the shape of the quadratic coefficient to change in a way that would be favourable to these phases in our model. This model failed to describe the onset of the complex phases. The reason for this must be that the approximations made in the derivation are too crude. The fact that the inclusion of conformational asymmetry into the derivation does not change the asymptotic behaviour of the quadratic coefficient means that this term on its own is not sufficient to account for the impact. In particular, relaxing the assumption that the cubic coefficient can be treated as a constant value could have a significant effect on the phase behaviour. Leibler's calculation uses a cubic term of the following form:

$$F_3[\phi] = \frac{1}{3!} \int \frac{d\mathbf{q}_1}{(2\pi)^3} \frac{d\mathbf{q}_2}{(2\pi)^3} \frac{d\mathbf{q}_3}{(2\pi)^3} \delta(\mathbf{q}_1 + \mathbf{q}_2 + \mathbf{q}_3) \tilde{G}^3(\mathbf{q}_1, \mathbf{q}_2, \mathbf{q}_3) \tilde{\phi}(\mathbf{q}_1) \tilde{\phi}(\mathbf{q}_2) \tilde{\phi}(\mathbf{q}_3), \quad (5.1)$$

Making the assumption that γ has no dependence on q means that we lose access to a lot of physically relevant effects that might stabilize the complex phases. One might consider a theory with a more complicated cubic term of the form in equation (5.1). However this term will make the numerical methods used in this work significantly more computationally intensive.

We considered two Ginzburg-Landau theories derived for a system of spheres interacting via a pairwise short-range attractive, long-range repulsive (SALR) potential. These were chosen to allow us to make comparisons with DFT results discussed in the introduction that showed the formation of the bcc and fcc spherical packing phases. First we considered a specific SALR potential which was the sum of two Gaussian functions. We saw that the free parameter in this theory is sufficient to stabilize the Frank-Kasper σ phase. This parameter, called α , is the ratio of length scales of the attractive and repulsive terms in the real-space potential. As this ratio approaches 1 the quadratic coefficient gets smaller for $q < 1$ and larger for $q > 1$, behaviours that are consistent with the factors needed to stabilize the complex phases. We then considered a SALR step-potential taken from a paper by Zhuang and Charbonneau [59]. We investigated how varying the parameters in this theory caused the shape of the quadratic coefficient to change. This result enabled us to develop some intuition for the relationship between the real-space interactions and the stability of the spherical packing phases. In particular, we observed that a weaker repulsion strength and a shorter range both stabilized the complex phases.

We described DFT calculations performed by Jiayu Xie and Cameron Burns, supervised by Dr. Shi, which showed that the same mechanisms that control the relative stability of the complex spherical packing phases in the Ginzburg-Landau theory are relevant in that model.

We set out to explore universal mechanisms that influence the formation and relative stability of the complex spherical packing phases in soft condensed matter systems. We discovered that a very simple Ginzburg-Landau theory is sufficient to explore this question, and we thoroughly probed the mechanisms that are available to this theory. Xie and Burns' result shows that these mechanisms extend beyond the GL theory and into the DFT as well. Ginzburg-Landau theories of the form considered in this work, and DFT theories of the form in equation (2.37) are ubiquitous in the literature. Our result has important consequences for any work that uses these theories to model the physics of a soft matter system. A natural next step for this project would be to include quasi-crystalline phases in the set \mathcal{P} of phases considered. Quasicrystal phases appear in many systems that also exhibit the complex phases, and might be stable in some of our models. Another promising extension could be to consider a two-field system with a free-energy functional of the form:

$$\begin{aligned}
 F[\phi, \psi] = & \frac{1}{2} \sum_{\mathbf{q}} \left(\Gamma_1(q) \left| \tilde{\phi}(\mathbf{q}) \right|^2 + \Gamma_2(q) \left| \tilde{\psi}(\mathbf{q}) \right|^2 + \Gamma_3(q) \tilde{\phi}(\mathbf{q}) \tilde{\psi}(-\mathbf{q}) \right) \\
 & + F_{local}[\phi] + F_{local}[\psi] + F_{coupling}[\phi, \psi].
 \end{aligned} \tag{5.2}$$

Such models appear for example in the study of binary blends. It is possible that the Frank-Kasper C14 and C15 phases might become stable in such a model. Both of these proposals will give us a more complete understanding of the phase behaviour exhibited by Ginzburg-Landau theories and allow us to better understand the universal mechanisms underlying self assembly in soft condensed matter systems.

Appendix A

Modified Leibler theory

This appendix contains the details of the modified Leibler calculation described in section 2.3.

A.1 Series expansion of the free energy functional

Here we will describe how the series expansion of the free energy functional, equation (2.26), is obtained. We want an expression for F expanded in powers of the order parameter field ϕ' , as defined in equation (2.25). To do this we first imagine that there is some external field $U(\mathbf{x})$ that couples to the density fluctuations $\delta\rho_A$ such that the system is disordered when $U = 0$. The full Hamiltonian for the system can be written:

$$\mathcal{H} = \mathcal{H}_{dis} + \int d\mathbf{x} U(\mathbf{x}) \delta\rho_A(\mathbf{x}), \quad (\text{A.1})$$

where \mathcal{H}_{dis} describes the system in the disordered state. The partition function for this Hamiltonian is a functional of U :

$$Z[U] = \text{Tr} \exp \left\{ -\beta \mathcal{H}_{dis} - \beta \int d\mathbf{x} U(\mathbf{x}) \delta\rho_A(\mathbf{x}) \right\} \quad (\text{A.2})$$

$$= Z_{dis} \left\langle \exp \left\{ -\beta \int d\mathbf{x} U(\mathbf{x}) \delta\rho_A(\mathbf{x}) \right\} \right\rangle_{dis}. \quad (\text{A.3})$$

In the second line Z_{dis} is the partition function of the disordered system and we have defined the thermal average with respect to the disordered Hamiltonian:

$$\langle f \rangle_{dis} = \frac{1}{Z_{dis}} \text{Tr} [f \exp \{-\beta \mathcal{H}_{dis}\}]. \quad (\text{A.4})$$

The Helmholtz free energy for this system is likewise a functional of U :

$$\begin{aligned} \beta F'[U] &= -\ln Z[U] \\ &= -\ln Z_{dis} - \ln \left\langle \exp \left\{ -\beta \int d\mathbf{x} U(\mathbf{x}) \delta \rho_A(\mathbf{x}) \right\} \right\rangle_{dis}. \end{aligned} \quad (\text{A.5})$$

The free energy functional that we are interested in, $F[\phi']$, is related to $F'[U]$ through a Legendre transform,

$$F[\phi'] = F'[U] - \int d\mathbf{x} U(\mathbf{x}) \phi'(\mathbf{x}). \quad (\text{A.6})$$

We will proceed first by expanding $F'[U]$ in powers of U and then by using equation (A.6) to relate that result to the one that we are actually interested in, the expansion of F in powers of ϕ' . The expansion of $F'[U]$ looks like,

$$\beta F'[U] = \beta F_{dis} - \sum_{n=1}^{\infty} \frac{(-\beta)^n}{n!} \int d\mathbf{x}_1 \cdots d\mathbf{x}_n C'_n(\mathbf{x}_1, \cdots, \mathbf{x}_n) U(\mathbf{x}_1) \cdots U(\mathbf{x}_n), \quad (\text{A.7})$$

where the n th coefficient C'_n is given by,

$$C'_n(\mathbf{x}_1, \cdots, \mathbf{x}_n) = -\frac{1}{(-\beta)^n} \left(\frac{\delta^n \beta F'[U]}{\delta U(\mathbf{x}_1) \cdots \delta U(\mathbf{x}_n)} \right)_{U=0}. \quad (\text{A.8})$$

In particular, note that the first coefficient is:

$$\begin{aligned} C'_1(\mathbf{x}) &= -\frac{1}{\beta} \left(\frac{1}{Z} \frac{\delta Z}{\delta U(\mathbf{x})} \right)_{U=0} \\ &= \langle \delta \rho_A(\mathbf{x}) \rangle_{dis} \\ &= 0. \end{aligned} \quad (\text{A.9})$$

Using the fact that the density fluctuations average to zero everywhere in the disordered state. The second coefficient is:

$$\begin{aligned} C'_2(\mathbf{x}_1, \mathbf{x}_2) &= \frac{1}{\beta^2} \left(\frac{1}{Z} \frac{\delta^2 Z}{\delta U(\mathbf{x}_1) \delta U(\mathbf{x}_2)} - \frac{1}{Z^2} \frac{\delta Z}{\delta U(\mathbf{x}_1)} \frac{\delta Z}{\delta U(\mathbf{x}_2)} \right)_{U=0} \\ &= \langle \delta \rho_A(\mathbf{x}_1) \delta \rho_A(\mathbf{x}_2) \rangle_{dis} - \langle \delta \rho_A(\mathbf{x}_1) \rangle_{dis} \langle \delta \rho_A(\mathbf{x}_2) \rangle_{dis} \\ &= \langle \delta \rho_A(\mathbf{x}_1) \delta \rho_A(\mathbf{x}_2) \rangle_{dis}. \end{aligned} \quad (\text{A.10})$$

In general the coefficients are related to the n -point correlation functions. For this work we only need the exact form of the quadratic coefficient.

At this point it is useful to take the Fourier transform of equation (A.7). We will do this term-by-term. Denote the n th term of (A.7) as F'_n . Just as in equation (2.5), translation invariance here means that for each coefficient C'_n ,

$$C'_n(\mathbf{x}_1, \dots, \mathbf{x}_n) = C'_n(\mathbf{x}_1 - \mathbf{y}, \dots, \mathbf{x}_n - \mathbf{y}). \quad (\text{A.11})$$

For any vector \mathbf{y} . Taking $\mathbf{y} = \mathbf{x}_n$, we can write:

$$\begin{aligned} C'_n(\mathbf{x}_1, \dots, \mathbf{x}_n) &= C'_n(\mathbf{x}_1 - \mathbf{x}_n, \dots, \mathbf{x}_{n-1} - \mathbf{x}_n, \mathbf{0}) \\ &\equiv C_n(\mathbf{x}_1 - \mathbf{x}_n, \dots, \mathbf{x}_{n-1} - \mathbf{x}_n), \end{aligned} \quad (\text{A.12})$$

where we are taking this as a definition for the un-primed coefficient C_n . We can replace C_n with the integral over its Fourier components:

$$\begin{aligned} C_n(\mathbf{x}_1 - \mathbf{x}_n, \dots, \mathbf{x}_{n-1} - \mathbf{x}_n) &= \\ &\int \frac{d\mathbf{q}_1}{(2\pi)^3} \dots \frac{d\mathbf{q}_{n-1}}{(2\pi)^3} \tilde{C}_n(\mathbf{q}_1, \dots, \mathbf{q}_{n-1}) e^{i\mathbf{q}_1 \cdot (\mathbf{x}_1 - \mathbf{x}_n)} \dots e^{i\mathbf{q}_{n-1} \cdot (\mathbf{x}_{n-1} - \mathbf{x}_n)}. \end{aligned} \quad (\text{A.13})$$

Putting this back into the expression for F'_n and rearranging the order of the integrals:

$$\begin{aligned} \beta F'_n[U] &= -\frac{(-\beta)^n}{n!} \int \frac{d\mathbf{q}_1}{(2\pi)^3} \dots \frac{d\mathbf{q}_{n-1}}{(2\pi)^3} \tilde{C}_n(\mathbf{q}_1, \dots, \mathbf{q}_{n-1}) \dots \\ &\int d\mathbf{x}_1 \dots d\mathbf{x}_n U(\mathbf{x}_1) \dots U(\mathbf{x}_n) e^{i\mathbf{q}_1 \cdot (\mathbf{x}_1 - \mathbf{x}_n)} \dots e^{i\mathbf{q}_{n-1} \cdot (\mathbf{x}_{n-1} - \mathbf{x}_n)}. \end{aligned} \quad (\text{A.14})$$

We can perform the integrals over \mathbf{x}_i for $i = 1, \dots, n-1$, each of which give us the Fourier transform of $U(\mathbf{x}_i)$:

$$\int d\mathbf{x}_i U(\mathbf{x}_i) e^{i\mathbf{q}_i \cdot \mathbf{x}_i} = \tilde{U}(\mathbf{q}_i). \quad (\text{A.15})$$

The integral over x_n looks a little bit different but gives the same result. We find:

$$\int d\mathbf{x}_n U(\mathbf{x}_n) e^{-i\mathbf{x}_n \cdot (\mathbf{q}_1 + \dots + \mathbf{q}_{n-1})} = \tilde{U}(-\mathbf{q}_1 - \dots - \mathbf{q}_{n-1}) \quad (\text{A.16})$$

We thus find that equation (A.14) becomes,

$$\begin{aligned} \beta F'_n[U] &= -\frac{(-\beta)^n}{n!} \int \frac{d\mathbf{q}_1}{(2\pi)^3} \dots \frac{d\mathbf{q}_{n-1}}{(2\pi)^3} \tilde{C}_n(\mathbf{q}_1, \dots, \mathbf{q}_{n-1}) \tilde{U}(\mathbf{q}_1) \dots \tilde{U}(\mathbf{q}_{n-1}) \tilde{U}(-\mathbf{q}_1 - \dots - \mathbf{q}_{n-1}) \\ &= -\frac{(-\beta)^n}{n!} \int \frac{d\mathbf{q}_1}{(2\pi)^3} \dots \frac{d\mathbf{q}_n}{(2\pi)^3} \delta(\mathbf{q}_1 + \dots + \mathbf{q}_n) \tilde{C}_n(\mathbf{q}_1, \dots, \mathbf{q}_{n-1}) \tilde{U}(\mathbf{q}_1) \dots \tilde{U}(\mathbf{q}_n). \end{aligned} \quad (\text{A.17})$$

The next step is to obtain an expression for $\tilde{U}(\mathbf{q})$ in terms of the order parameter $\tilde{\phi}'$. The order parameter in Fourier space, $\tilde{\phi}'(\mathbf{q}) = \langle \tilde{\delta}\rho_A(\mathbf{q}) \rangle$, is given by,

$$\begin{aligned}\tilde{\phi}'(\mathbf{q}) &= \frac{1}{Z} \text{Tr} \delta\rho_A(\mathbf{q}) \exp \left\{ -\beta\mathcal{H}_{dis} - \beta \int \frac{d\mathbf{q}'}{(2\pi)^3} \tilde{U}(-\mathbf{q}') \tilde{\delta}\rho_A(\mathbf{q}') \right\} \\ &= -\frac{1}{\beta} \frac{\delta \ln Z}{\delta \tilde{U}(-\mathbf{q})} \\ &= \frac{1}{\beta} \frac{\delta \beta F'[U]}{\delta \tilde{U}(-\mathbf{q})}.\end{aligned}\tag{A.18}$$

So by differentiating each term of equation (A.17) we find,

$$\begin{aligned}\tilde{\phi}'(\mathbf{q}) &= \sum_{n=2}^{\infty} \frac{(-\beta)^{n-1}}{(n-1)!} \int \frac{d\mathbf{q}_2}{(2\pi)^3} \cdots \frac{d\mathbf{q}_n}{(2\pi)^3} \delta(\mathbf{q} + \mathbf{q}_2 + \cdots + \mathbf{q}_n) \cdots \\ &\quad \tilde{C}_n(\mathbf{q}, \mathbf{q}_2, \cdots, \mathbf{q}_{n-1}) \tilde{U}(\mathbf{q}_2) \cdots \tilde{U}(\mathbf{q}_{n-1}) \tilde{U}(\mathbf{q}_n).\end{aligned}\tag{A.19}$$

Equation (A.19) can be inverted iteratively to obtain an expression for \tilde{U} in terms of $\tilde{\phi}'$. To do this we first write \tilde{U} as a series in powers of $\tilde{\phi}'$:

$$\tilde{U}(\mathbf{q}) = \tilde{U}_0(\mathbf{q}) + \tilde{U}_1(\mathbf{q}) + \cdots.\tag{A.20}$$

We can plug equation (A.20) into (A.19) and match powers of $\tilde{\phi}'$. Finding \tilde{U}_0 is simple, since there are no zeroth order terms on the left-hand side of (A.19):

$$\begin{aligned}0 &= -\beta \int \frac{d\mathbf{q}_2}{(2\pi)^3} \delta(\mathbf{q} + \mathbf{q}_2) \tilde{C}_2(\mathbf{q}) \tilde{U}_0(\mathbf{q}_2) \\ &\quad + \frac{\beta^2}{2!} \int \frac{d\mathbf{q}_2}{(2\pi)^3} \frac{d\mathbf{q}_3}{(2\pi)^3} \delta(\mathbf{q} + \mathbf{q}_2 + \mathbf{q}_3) \tilde{C}_3(\mathbf{q}, \mathbf{q}_2) \tilde{U}_0(\mathbf{q}_2) \tilde{U}_0(\mathbf{q}_3) + \\ &\quad + \cdots.\end{aligned}\tag{A.21}$$

This requires that $\tilde{U}_0 = 0$. For \tilde{U}_1 we find that the only term on the right-hand side of (A.19) that is linear in $\tilde{\phi}'$ comes from the $n = 2$ term:

$$\begin{aligned}\tilde{\phi}'(\mathbf{q}) &= -\beta \int \frac{d\mathbf{q}_2}{(2\pi)^3} \delta(\mathbf{q} + \mathbf{q}_2) \tilde{C}_2(\mathbf{q}) \tilde{U}_1(\mathbf{q}_2) \\ &= -\beta \tilde{C}_2(\mathbf{q}) \tilde{U}_1(-\mathbf{q}).\end{aligned}\tag{A.22}$$

Rearranging this result, we obtain,

$$\tilde{U}_1(-\mathbf{q}) = -\frac{1}{\beta} \frac{\tilde{\phi}'(\mathbf{q})}{\tilde{C}_2(\mathbf{q})}\tag{A.23}$$

In this way we can iterate to find \tilde{U}_n for any n , although the algebra does become messy. Mercifully, for our purposes it is adequate to stop here.

Returning to equation (A.6) and differentiating with respect to ϕ' , we find,

$$\frac{\delta F[\phi']}{\delta \tilde{\phi}'(\mathbf{q})} = -\tilde{U}(\mathbf{q}). \quad (\text{A.24})$$

Integrating equation (A.20) term-by-term allows us to easily obtain the series expression for $F[\phi']$ up to a constant factor,

$$\begin{aligned} \beta F[\phi'] = & \frac{1}{2} \int \frac{d\mathbf{q}_1}{(2\pi)^3} \frac{d\mathbf{q}_2}{(2\pi)^3} \delta(\mathbf{q}_1 + \mathbf{q}_2) \tilde{G}_2(\mathbf{q}_1) \tilde{\phi}'(\mathbf{q}_1) \tilde{\phi}'(\mathbf{q}_2) \cdots \\ & + \frac{1}{3!} \int \frac{d\mathbf{q}_1}{(2\pi)^3} \cdots \frac{d\mathbf{q}_3}{(2\pi)^3} \delta(\mathbf{q}_1 + \cdots + \mathbf{q}_3) \tilde{G}_3(\mathbf{q}_1, \mathbf{q}_2) \tilde{\phi}'(\mathbf{q}_1) \cdots \tilde{\phi}'(\mathbf{q}_3) \\ & + \cdots, \end{aligned} \quad (\text{A.25})$$

where consideration of equation (A.23) reveals that

$$G_2(\mathbf{q}) = \frac{1}{\tilde{C}_2(\mathbf{q})}. \quad (\text{A.26})$$

We have thus arrived at equations (2.26) and (2.27).

A.2 Ideal chain correlation functions

In this section we will derive the two-point correlation functions for a non-interacting, ideal diblock copolymer chain, equations (2.29), (2.30) and (2.31) in the text.

We start with a string of $N + 1$ beads connected by springs. Let \mathbf{x}_i be the position of the i th bead ($i = 0, \dots, N$) The Hamiltonian for a single chain is:

$$\mathcal{H}_0 = \frac{1}{2} \sum_{i=1}^N k_i (\mathbf{x}_i - \mathbf{x}_{i-1})^2. \quad (\text{A.27})$$

Note that we are using the subscript 0 to distinguish the Hamiltonian of the ideal system from that of the disordered system, \mathcal{H}_{dis} , discussed in the last section. Here k_i is the spring constant for the spring connecting the i^{th} bead to the $(i - 1)^{st}$. In this model the spring constants are related to the Kuhn lengths b_i of the polymers through:

$$k_i = \frac{3}{\beta b_i^2}. \quad (\text{A.28})$$

For the AB diblock $b_i = b_A = \sqrt{\epsilon}b$ for $i \leq fN$ and $b_i = b_B = b$ for $i > fN$. The partition function for this model is,

$$\begin{aligned} Z_0 &= \int d\mathbf{x}_0 \cdots d\mathbf{x}_N \exp\{-\beta\mathcal{H}_0(\{\mathbf{x}_i\})\} \\ &= \int d\mathbf{x}_0 \cdots d\mathbf{x}_N \exp\left\{-\sum_{i=1}^N \frac{3}{2b_i}(\mathbf{x}_i - \mathbf{x}_{i-1})^2\right\}. \end{aligned} \quad (\text{A.29})$$

Here the trace over system states becomes a series of $N + 1$ integrals over positions of each bead. We see how the quadratic functional form of \mathcal{H}_0 results in a Gaussian integral in the partition function. We can evaluate equation (A.29) exactly. First define the bond vectors $\mathbf{u}_i = \mathbf{x}_i - \mathbf{x}_{i-1}$. We will do a change of variables from $\mathbf{x}_0, \mathbf{x}_1, \dots, \mathbf{x}_N$ to $\mathbf{x}_0, \mathbf{u}_1, \dots, \mathbf{u}_N$. The determinant of the Jacobian for this transformation is 1, and so the partition function becomes,

$$\begin{aligned} Z_0 &= \int d\mathbf{x}_0 \int d\mathbf{u}_1 \cdots d\mathbf{u}_N \exp\left\{-\sum_{i=1}^N \frac{3}{2b_i}u_i^2\right\} \\ &= \mathcal{V} \prod_{i=1}^N \left(\frac{2\pi b_i^2}{3}\right)^{3/2} \\ &= \mathcal{V} \left(\frac{2\pi \epsilon^f b^2}{3}\right)^{3N/2}. \end{aligned} \quad (\text{A.30})$$

The integral over \mathbf{x}_0 gives us the factor of the system volume \mathcal{V} , this is a reflection of the translation invariance of the centre of mass of the system.

We can now move on to the main result of this section, which is the calculation of the two-point correlation functions,

$$S_{\mu\nu}(\mathbf{x}, \mathbf{x}') = \langle \delta\rho_\mu(\mathbf{x})\delta\rho_\nu(\mathbf{x}') \rangle_0, \quad (\text{A.31})$$

where $\delta\rho_\mu(\mathbf{x}) = \rho_\mu - \langle \rho_\mu \rangle_0$. From this we get the following expression for $S_{\mu\nu}(\mathbf{x}, \mathbf{x}')$:

$$S_{\mu\nu}(\mathbf{x}, \mathbf{x}') = \langle \rho_\mu(\mathbf{x})\rho_\nu(\mathbf{x}') \rangle_0 - \langle \rho_\mu(\mathbf{x}) \rangle_0 \langle \rho_\nu(\mathbf{x}') \rangle_0. \quad (\text{A.32})$$

We will begin by computing $\langle \rho_\mu(\mathbf{x}) \rangle_0$. Using the definition of ρ_μ in equation (2.23):

$$\langle \rho_\mu(\mathbf{x}) \rangle_0 = \frac{\mathcal{V}}{N} \sum_{i=1}^{N_\mu} \langle \delta(\mathbf{x} - \mathbf{x}_i) \rangle_0. \quad (\text{A.33})$$

We need the thermal average of the delta function:

$$\begin{aligned}
 \langle \delta(\mathbf{x} - \mathbf{x}_i) \rangle_0 &= \frac{1}{Z_0} \int d\mathbf{x}_0 \cdots d\mathbf{x}_N \delta(\mathbf{x} - \mathbf{x}_i) \exp \left\{ -\frac{1}{2} \sum_{j=1}^N \frac{3}{b_j^2} (\mathbf{x}_j - \mathbf{x}_{j-1})^2 \right\} \\
 &= \frac{1}{Z_0} \int \frac{d\mathbf{q}}{(2\pi)^3} \int d\mathbf{x}_0 \cdots d\mathbf{x}_N \exp \left\{ i\mathbf{q} \cdot (\mathbf{x} - \mathbf{x}_i) - \frac{1}{2} \sum_{j=1}^N \frac{3}{b_j^2} (\mathbf{x}_j - \mathbf{x}_{j-1})^2 \right\}.
 \end{aligned} \tag{A.34}$$

Using the fact that $\mathbf{x}_i = \mathbf{x}_0 + \mathbf{u}_1 + \cdots + \mathbf{u}_i$, we can perform the same change of variables trick that we used to compute Z_0 :

$$\begin{aligned}
 \langle \delta(\mathbf{x} - \mathbf{x}_i) \rangle_0 &= \frac{1}{Z_0} \int \frac{d\mathbf{q}}{(2\pi)^3} e^{i\mathbf{q} \cdot \mathbf{x}} \int d\mathbf{x}_0 e^{-i\mathbf{q} \cdot \mathbf{x}_0} d\mathbf{u}_1 \cdots d\mathbf{u}_N \exp \left\{ -i\mathbf{q} \cdot \sum_{j=1}^i \mathbf{u}_j - \frac{1}{2} \sum_{j=1}^N \frac{3}{b_j^2} u_j^2 \right\} \\
 &= \frac{1}{Z_0} \int \frac{d\mathbf{q}}{(2\pi)^3} (2\pi)^3 \delta(\mathbf{q}) e^{i\mathbf{q} \cdot \mathbf{x}} \int d\mathbf{u}_1 \cdots d\mathbf{u}_N \exp \left\{ -i\mathbf{q} \cdot \sum_{j=1}^N \mathbf{u}_j - \frac{1}{2} \sum_{j=1}^N \frac{3}{b_j^2} u_j^2 \right\} \\
 &= \frac{1}{Z_0} \int d\mathbf{u}_1 \cdots d\mathbf{u}_N \exp \left\{ -\frac{1}{2} \sum_{j=1}^N \frac{3}{b_j^2} u_j^2 \right\} \\
 &= \frac{1}{\mathcal{V}}.
 \end{aligned} \tag{A.35}$$

Putting this back into equation (A.33):

$$\langle \rho_\mu(\mathbf{x}) \rangle_0 = \frac{N_\mu}{N}. \tag{A.36}$$

This is an unsurprising result (see the discussion in section 2.3), but it is nevertheless comforting to see. Returning to equation (A.32), we still need to compute the two point density correlation functions:

$$\begin{aligned}
 T_{\mu\nu}(\mathbf{x}, \mathbf{x}') &\equiv \langle \rho_\mu(\mathbf{x}) \rho_\nu(\mathbf{x}') \rangle_0 \\
 &= \frac{\mathcal{V}^2}{N^2} \sum_{i=1}^{N_\mu} \sum_{j=1}^{N_\nu} \langle \delta(\mathbf{x} - \mathbf{x}_i) \delta(\mathbf{x}' - \mathbf{x}_j) \rangle_0.
 \end{aligned} \tag{A.37}$$

We will treat the two distinct cases, $\mu = \nu$ and $\mu \neq \nu$, separately. Let's start with the $\mu = \nu$ case:

$$\begin{aligned}
 T_{\mu\mu}(\mathbf{x}, \mathbf{x}') &= \frac{\mathcal{V}^2}{N^2} \sum_{i,j=1}^{N_\mu} \langle \delta(\mathbf{x} - \mathbf{x}_i) \delta(\mathbf{x}' - \mathbf{x}_j) \rangle_0 \\
 &= \frac{2\mathcal{V}^2}{N^2} \sum_{i < j} R_{ij}.
 \end{aligned} \tag{A.38}$$

In the second line $R_{ij} = \langle \delta(\mathbf{x} - \mathbf{x}_i) \delta(\mathbf{x}' - \mathbf{x}_j) \rangle_0$ Computing this quantity:

$$\begin{aligned}
 R_{ij} &= \frac{1}{Z_0} \int d\mathbf{x}_0 \cdots d\mathbf{x}_N \int \frac{d\mathbf{q}}{(2\pi)^3} \frac{d\mathbf{q}'}{(2\pi)^3} \cdots \\
 &\quad \exp \left\{ i\mathbf{q} \cdot (\mathbf{x} - \mathbf{x}_i) + i\mathbf{q}' \cdot (\mathbf{x}' - \mathbf{x}_j) - \frac{1}{2} \sum_{k=1}^N \frac{3}{b_k^2} (\mathbf{x}_k - \mathbf{x}_{k-1})^2 \right\} \\
 &= \frac{1}{Z_0} \int \frac{d\mathbf{q}}{(2\pi)^3} \frac{d\mathbf{q}'}{(2\pi)^3} e^{i\mathbf{q} \cdot \mathbf{x} + i\mathbf{q}' \cdot \mathbf{x}'} \int d\mathbf{x}_0 e^{-i(\mathbf{q} + \mathbf{q}') \cdot \mathbf{x}_0} \dots \\
 &\quad \int d\mathbf{u}_1 \cdots d\mathbf{u}_N \exp \left\{ -i(\mathbf{q} + \mathbf{q}') \cdot \sum_{k=1}^i \mathbf{u}_k - i\mathbf{q}' \cdot \sum_{k=i+1}^j \mathbf{u}_k - \frac{1}{2} \sum_{k=1}^N \frac{3}{b_k^2} u_k^2 \right\} \\
 &= \frac{1}{Z_0} \int \frac{d\mathbf{q}}{(2\pi)^3} e^{i\mathbf{q} \cdot (\mathbf{x} - \mathbf{x}')} \int d\mathbf{u}_1 \cdots d\mathbf{u}_N \exp \left\{ i\mathbf{q} \cdot \sum_{k=i+1}^j \mathbf{u}_k - \frac{1}{2} \sum_{k=1}^N \frac{3}{b_k^2} u_k^2 \right\} \\
 &= \frac{1}{\mathcal{V}} \int \frac{d\mathbf{q}}{(2\pi)^3} \exp \left\{ i\mathbf{q} \cdot (\mathbf{x} - \mathbf{x}') - \frac{1}{2} \sum_{k=i+1}^j \frac{b_k^2}{3} q^2 \right\} \\
 &= \frac{1}{\mathcal{V}} \left(\frac{3}{2\pi \sum_k b_k^2} \right)^{3/2} \exp \left\{ -\frac{3}{2 \sum_k b_k^2} (\mathbf{x} - \mathbf{x}')^2 \right\}. \tag{A.39}
 \end{aligned}$$

At this point we can note that $T_{\mu\nu}$ is a function of the distance between \mathbf{x} and \mathbf{x}' only: $T_{\mu\nu}(\mathbf{x}, \mathbf{x}') = T_{\mu\nu}(\mathbf{x} - \mathbf{x}')$. This is a reflection of the translation invariance of the system. We should evaluate the sum in this expression. Noting that $b_k = b_\mu$ for all terms:

$$\sum_{k=i+1}^j b_k^2 = b_\mu^2 (j - i), \tag{A.40}$$

equation (A.39) becomes:

$$R_{ij} = \frac{1}{\mathcal{V}} \left(\frac{3}{2\pi b_\mu^2 (j - i)} \right)^{3/2} \exp \left\{ -\frac{3}{2b_\mu^2 (j - i)} (\mathbf{x} - \mathbf{x}')^2 \right\}. \tag{A.41}$$

We can now compute $T_{\mu\mu}(\mathbf{x} - \mathbf{x}')$, equation (A.38)

$$T_{\mu\mu}(\mathbf{x} - \mathbf{x}') = \frac{2\mathcal{V}}{N^2} \sum_{i < j} \left(\frac{3}{2\pi b_\mu^2 (j - i)} \right)^{3/2} \exp \left\{ -\frac{3}{2b_\mu^2 (j - i)} (\mathbf{x} - \mathbf{x}')^2 \right\}. \tag{A.42}$$

We will make the assumption that the chains are very long relative to the length of an individual segment ($N_\mu b_\mu \gg b_\mu$ or $N_\mu \gg 1$) and replace the sums with integrals,

$$\sum_{i=0}^{N_\mu-1} \sum_{j=i+1}^{N_\mu} \rightarrow \int_0^{f_\mu N} ds \int_s^{f_\mu N} ds', \tag{A.43}$$

where s_i and s_j are dimensionless parameters that measure the distance travelled along the chain and $f_\mu = N_\mu/N$. The sum in equation (A.42) becomes an integral,

$$T_{\mu\mu}(\mathbf{x} - \mathbf{x}') \equiv \frac{2\mathcal{V}}{N^2} \int_0^{f_\mu N} ds \int_s^{f_\mu N} ds' \left(\frac{3}{2\pi b_\mu^2 (s' - s)} \right)^{3/2} \exp \left\{ -\frac{3}{2b_\mu^2 (s' - s)} (\mathbf{x} - \mathbf{x}')^2 \right\}. \tag{A.44}$$

To evaluate this integral we will first take the Fourier transform,

$$\begin{aligned}
 \tilde{T}_{\mu\mu}(\mathbf{q}) &= \int d\mathbf{y} T_{\mu\mu}(\mathbf{y}) e^{-i\mathbf{y}\cdot\mathbf{q}} \\
 &= \frac{2\mathcal{V}}{N^2} \int_0^{f_\mu N} ds \int_s^{f_\mu N} ds' \exp \left\{ -\frac{b_\mu^2 (s-s')}{6} q^2 \right\} \\
 &= \frac{2\mathcal{V}}{N^2} \left(\frac{6}{b_\mu^2 q^2} \right)^2 \left(\frac{f_\mu N b_\mu^2}{6} q^2 + \exp \left\{ -\frac{N_\mu b_\mu^2}{6} q^2 \right\} - 1 \right). \quad (\text{A.45})
 \end{aligned}$$

Let $x = \frac{1}{6} N b^2 q^2$. The Fourier transform of the two-point $\mu\mu$ density correlation function is:

$$\tilde{T}_{\mu\mu}(q) = 2\mathcal{V} \left(\frac{1}{\epsilon_\mu x} \right)^2 (f_\mu \epsilon_\mu x + \exp \{-f_\mu \epsilon_\mu x\} - 1), \quad (\text{A.46})$$

where $\epsilon_\mu = b_\mu/b$. The Fourier transform of the full scattering function (equation (A.32)) is,

$$\tilde{S}_{\mu\mu}(\mathbf{q}) = \tilde{T}_{\mu\mu}(\mathbf{q}) - (2\pi)^3 f_\mu^2 \delta(\mathbf{q}). \quad (\text{A.47})$$

From this we get equations (2.29) and (2.30) in section 2.3.

Next up we repeat the calculation for $\mu \neq \nu$. In this case $T_{\mu\nu} = T_{AB}$ and equation (A.37) becomes,

$$T_{AB}(\mathbf{x}, \mathbf{x}') = \frac{\mathcal{V}^2}{N^2} \sum_{i=0}^{fN} \sum_{j=fN+1}^N R_{ij}. \quad (\text{A.48})$$

The calculation of R_{ij} in this case is the same as above up until equation (A.39), at which point we need to compute the sum over Kuhn lengths. This time we note that $i < fN$ and $j > fN$, so:

$$\begin{aligned}
 \sum_{k=i+1}^j b_k^2 &= \sum_{k=i+1}^{fN} \epsilon b^2 + \sum_{k=fN+1}^j b^2 \\
 &= (fN - i)\epsilon b^2 + (j - fN)b^2. \quad (\text{A.49})
 \end{aligned}$$

Putting this back into equation (A.48) we are left to compute the sum:

$$\begin{aligned}
 T_{AB}(\mathbf{x} - \mathbf{x}') &= \frac{\mathcal{V}}{N^2} \sum_{i=0}^{fN} \sum_{j=fN}^N \dots \\
 &\quad \left(\frac{3}{2\pi b^2 ((fN - i)\epsilon + (j - fN))} \right)^{3/2} \exp \left\{ -\frac{3(\mathbf{x} - \mathbf{x}')^2}{2b^2 ((fN - i)\epsilon + (j - fN))} \right\}. \quad (\text{A.50})
 \end{aligned}$$

As before we convert this into an integral:

$$\begin{aligned}
 T_{AB}(\mathbf{x} - \mathbf{x}') &\rightarrow \frac{\mathcal{V}}{N^2} \int_0^{fN} ds \int_{fN}^N ds' \dots \\
 &\quad \left(\frac{3}{2\pi b^2 ((fN - s)\epsilon + (s' - fN))} \right)^{3/2} \exp \left\{ -\frac{3(\mathbf{x} - \mathbf{x}')^2}{2b^2 ((fN - s)\epsilon + (s' - fN))} \right\}. \quad (\text{A.51})
 \end{aligned}$$

Taking the Fourier transform and evaluating, we arrive at the two-point AB density correlation function:

$$\begin{aligned}
 \tilde{T}_{AB}(\mathbf{q}) &= \frac{\mathcal{V}}{N^2} \int_0^{fN} ds \int_{fN}^N ds' \exp \left\{ -\frac{b^2((fN-s)\epsilon + (s'-fN))}{6} q^2 \right\} \\
 &= \frac{\mathcal{V}}{\epsilon N^2} \left(\frac{6}{b^2 q^2} \right)^2 \left(1 - \exp \left\{ -\frac{\epsilon b^2 f N}{6} \right\} \right) \left(1 - \exp \left\{ -\frac{b^2(1-f)N}{6} q^2 \right\} \right) \\
 &= \mathcal{V} \frac{1}{\epsilon x^2} (1 - e^{-f\epsilon x}) (1 - e^{-(1-f)x}), \tag{A.52}
 \end{aligned}$$

where x has the same definition as before. The Fourier transform of the full AB scattering function is,

$$\tilde{S}_{AB}(\mathbf{q}) = \tilde{T}_{AB}(\mathbf{x}) - (2\pi)^3 f(1-f)\delta(\mathbf{q}). \tag{A.53}$$

This gives us equation (2.31) in section 2.3.

A.3 Random phase approximation

In this section we will show how the random phase approximation (RPA) can be used to get an expression for the two point correlation function $\tilde{C}_2(\mathbf{q})$. We begin by considering the two point $\mu\nu$ -correlation function in real space:

$$C_2^{\mu\nu}(\mathbf{x} - \mathbf{x}') = \langle \delta\rho_\mu(\mathbf{x})\delta\rho_\nu(\mathbf{x}') \rangle_{dis}, \tag{A.54}$$

where μ and $\nu = A, B$. Recall the incompressibility condition requires that $\delta\rho_A + \delta\rho_B = 0$. This means that there is actually only one correlation function $C_2^{AA} = C_2^{BB} = -C_2^{AB}$. Elsewhere we have called this function C_2 . We imagine applying external fields U_μ ($\mu = A, B$) to produce density fluctuations ϕ'_μ . The relationship between the density at \mathbf{x} and a field applied at position \mathbf{x}' is determined by the correlation functions. Since we are only interested in an expression for the two-point correlation function it is sufficient to consider a linear response:

$$\phi'_\mu(\mathbf{x}) = -\beta \sum_\nu \int d\mathbf{x}' C_2^{\mu\nu}(\mathbf{x} - \mathbf{x}') U_\nu(\mathbf{x}'). \tag{A.55}$$

Actually it will be useful to work in reciprocal space for this work:

$$\tilde{\phi}'_\mu(\mathbf{q}) = -\beta \sum_\nu \tilde{C}_2^{\mu\nu}(\mathbf{q}) \tilde{U}_\nu(\mathbf{q}). \tag{A.56}$$

The RPA assumes that the interaction terms in the Hamiltonian \mathcal{H}_{dis} are small so that the response of the system to the applied fields \tilde{U}_μ is the same as the response of the *ideal* system to two effective fields $\tilde{U}_\mu^{\text{eff}}$:

$$\tilde{\phi}'_\mu(\mathbf{q}) = -\beta \sum_\nu \tilde{S}_2^{\mu\nu}(\mathbf{q}) \tilde{U}_\nu^{\text{eff}}(\mathbf{q}), \quad (\text{A.57})$$

where $\tilde{S}_2^{\mu\nu}$ is the Fourier transform of the response function for the ideal system:

$$S_2^{\mu\nu} = \langle \delta\rho_\mu(\mathbf{x}) \delta\rho_\nu(\mathbf{x}') \rangle_0. \quad (\text{A.58})$$

$\tilde{U}_\nu^{\text{eff}}$ accounts for the applied field \tilde{U}_ν and the interactions between the *A* and *B* segments. We also include a Lagrange multiplier, λ , that is used to enforce the incompressibility condition $\phi'_A + \phi'_B = 0$:

$$\tilde{U}_\nu^{\text{eff}}(\mathbf{q}) = \tilde{U}_\nu(\mathbf{q}) + \tilde{U}_\nu^{\text{int}}(\mathbf{q}) + \lambda(\mathbf{q}). \quad (\text{A.59})$$

The standard interaction term is a contact interaction between the *A* and *B* segments, $\tilde{U}_\nu^{\text{int}} = \sum_\gamma V^{\nu\gamma} \tilde{\phi}'_\gamma$, where,

$$V^{\nu\gamma} = \begin{cases} 0 & \nu = \gamma \\ \frac{1}{\beta}\chi & \nu \neq \gamma \end{cases}. \quad (\text{A.60})$$

χ is the strength of the interaction between segments, called the Flory interaction parameter. See for example discussions in [62] and [66]. The RPA can be summarized in the following matrix equation,

$$\begin{pmatrix} \tilde{\phi}'_A \\ \tilde{\phi}'_B \end{pmatrix} = -\beta \begin{pmatrix} \tilde{S}_2^{AA} & \tilde{S}_2^{AB} \\ \tilde{S}_2^{AB} & \tilde{S}_2^{BB} \end{pmatrix} \left[\begin{pmatrix} \tilde{U}_A \\ \tilde{U}_B \end{pmatrix} + \begin{pmatrix} 0 & \chi/\beta \\ \chi/\beta & 0 \end{pmatrix} \begin{pmatrix} \tilde{\phi}'_A \\ \tilde{\phi}'_B \end{pmatrix} + \lambda \begin{pmatrix} 1 \\ 1 \end{pmatrix} \right], \quad (\text{A.61})$$

where we have suppressed the \mathbf{q} dependence. We begin by calculating λ from the incompressibility condition. A bit of algebra yields the following result:

$$\lambda = c_A \tilde{U}_A + c_B \tilde{U}_B, \quad (\text{A.62})$$

with constants c_A and c_B defined by,

$$c_A = \frac{\tilde{S}_2^{AA} + \tilde{S}_2^{AB} - \chi W}{2\chi W - S}, \quad (\text{A.63})$$

$$c_B = \frac{\tilde{S}_2^{BB} + \tilde{S}_2^{AB} - \chi W}{2\chi W - S}. \quad (\text{A.64})$$

W is the determinant of the correlation matrix in equation (A.61),

$$W = S_2^{AA} S_2^{BB} - (S_2^{AB})^2, \quad (\text{A.65})$$

and S is a linear combination of the correlation functions,

$$S = S_2^{AA} + S_2^{BB} - 2S_2^{AB}. \quad (\text{A.66})$$

These are the definitions that appear in equations (2.35) and (2.36). Putting equation (A.62) back into equation (A.61) and rearranging the terms yields this expression:

$$A \begin{pmatrix} \tilde{\phi}'_A \\ \tilde{\phi}'_B \end{pmatrix} = -\beta B \begin{pmatrix} \tilde{U}_A \\ \tilde{U}_B \end{pmatrix}, \quad (\text{A.67})$$

where the matrices A and B are,

$$A = \begin{pmatrix} 1 + \chi \tilde{S}_2^{AB} & \chi \tilde{S}_2^{AA} \\ \chi \tilde{S}_2^{BB} & 1 + \chi \tilde{S}_2^{AB} \end{pmatrix}, \quad (\text{A.68})$$

$$B = \begin{pmatrix} \tilde{S}_2^{AA} & \tilde{S}_2^{AB} \\ \tilde{S}_2^{AB} & \tilde{S}_2^{BB} \end{pmatrix} \begin{pmatrix} 1 + c_A & c_B \\ c_A & 1 + c_B \end{pmatrix}. \quad (\text{A.69})$$

We can rewrite equation (A.67) so that it is in the form of (A.56):

$$\begin{pmatrix} \tilde{\phi}'_A \\ \tilde{\phi}'_B \end{pmatrix} = \beta \begin{pmatrix} \tilde{C}_2^{AA} & \tilde{C}_2^{AB} \\ \tilde{C}_2^{AB} & \tilde{C}_2^{BB} \end{pmatrix} \begin{pmatrix} \tilde{U}_A \\ \tilde{U}_B \end{pmatrix}, \quad (\text{A.70})$$

and read off the expression for the correlation function: $\tilde{C}_2 = \tilde{C}_2^{AA} = (A^{-1}B)_{11}$. Again working through the algebra we find,

$$\tilde{C}_2^{AA}(\mathbf{q}) = \frac{W(\mathbf{q})}{S(\mathbf{q}) - 2\chi W(\mathbf{q})}. \quad (\text{A.71})$$

This is equation (2.34) in the text.

Appendix B

Numerical details

B.1 Initializations

Each phase is initialized using a function $f_p(\mathbf{x})$, and then adjusted so that it satisfies

$$\sum_{i=1}^N \phi_p(\mathbf{x}_i) = 0, \quad (\text{B.1})$$

where $N = N_x N_y N_z$ is the total number of grid points. This condition is guaranteed by defining the initial density profile as

$$\phi_p(\mathbf{x}) = f_p(\mathbf{x}) - \frac{1}{N} \sum_{i=1}^N f(\mathbf{x}_i). \quad (\text{B.2})$$

B.1.1 Spherical phases

All of the spherical phases are initialized using equation (B.2) with a function $f_p(\mathbf{x})$ of the following form:

$$f_p(\mathbf{x}) = \sum_{\mathbf{x}_i} g_r(\mathbf{x} - \mathbf{x}_i), \quad (\text{B.3})$$

where the sum is over the locations of the centres of each of the spheres and $g_r(\mathbf{x} - \mathbf{x}_i)$ defines a sphere with radius r centred at \mathbf{x}_i :

$$g(\mathbf{x}) = \exp \left\{ 1 - \left(1 - (\mathbf{x} - \mathbf{x}_i)^2 / r^2 \right)^{-1} \right\}. \quad (\text{B.4})$$

phase	grid size(s)	unit cell dimension(s)	initialization function, $f_p(\mathbf{x})$
lamellar (lam)	$N_x = 64$	$l_x = 2\pi$	$\phi_{lam}(x) = \cos\left(\frac{2\pi}{l_x}x\right)$
hcp cylindrical (hex)	$N_x = 64$ $N_y = 64$	$l_x = 4\pi/\sqrt{3}$ $l_y = 4\pi$	$\phi_{hex}(x, y) = \cos\left(\frac{4\pi}{l_y}y\right)$ $+ 2 \cos\left(\frac{2\pi}{l_x}x\right) \cos\left(\frac{2\pi}{l_y}y\right)$
double gyroid (gyr)	$N_x = 64$ $N_y = 64$ $N_z = 64$	$l_x = 15$ $l_y = 15$ $l_z = 15$	$\phi_{gyr}(x, y, z) = \begin{cases} 1 - \frac{\bar{\phi}}{v} & r(x, y, z) > 1 \\ -\frac{\bar{\phi}}{v} & r(x, y, z) < 1 \end{cases}$ <p>where</p> $r(x, y, z) = \sin\left(\frac{2\pi}{l_x}x\right) \cos\left(\frac{2\pi}{l_x}x\right)$ $+ \sin\left(\frac{2\pi}{l_y}y\right) \cos\left(\frac{2\pi}{l_y}y\right)$ $+ \sin\left(\frac{2\pi}{l_z}z\right) \cos\left(\frac{2\pi}{l_z}z\right)$

Table B.1: Initialization functions, $f_p(\mathbf{x})$, and parameters for non-spherical phases.

Figure B.1 shows a one-dimensional cross section of the spherical profile created by $g_r(\mathbf{x})$.

Table B.2 contains a list of coordinates for all of the spheres in the unit cell of each spherical phase, as well as the radius r of the spheres and the grid sizes and initial unit cell dimensions. Together with equation (B.3), this provides the information needed to initialize the spherical phases. Note that the unit cell is assumed to have opposite corners located at the coordinates $(0, 0, 0)$ and (l_x, l_y, l_z) , and that the coordinates given in the table should be interpreted as *fractions* of their respective dimensions, so for example the coordinate $(1, 1, 0.5)$ should be interpreted as the point $(l_x, l_y, l_z/2)$ in the unit cell.

phase	grid size(s)	unit cell dimension(s)	sphere coordinate list	sphere radius, r
body-centred cubic (bcc)	$N_x = 64$ $N_y = 64$ $N_z = 64$	$l_x = 2\sqrt{2}\pi$ $l_y = 2\sqrt{2}\pi$ $l_z = 2\sqrt{2}\pi$	$(1/2, 1/2, 1/2), (0, 0, 0),$ $(1, 0, 0), (0, 1, 0),$ $(0, 0, 1), (1, 1, 0),$ $(1, 0, 1), (0, 1, 1),$ $(1, 1, 1)$	$r_{bcc} = 2\sqrt{2}\pi$
face-centred cubic (fcc)	$N_x = 64$ $N_y = 64$ $N_z = 64$	$l_x = 2\sqrt{3}\pi$ $l_y = 2\sqrt{3}\pi$ $l_z = 2\sqrt{3}\pi$	$(0, 0, 0), (1, 0, 0),$ $(0, 1, 0), (0, 0, 1),$ $(1, 1, 0), (1, 0, 1),$ $(0, 1, 1), (1, 1, 1),$ $(1/2, 1/2, 0), (1/2, 0, 1/2),$ $(0, 1/2, 1/2), (1/2, 1/2, 1),$ $(1/2, 1, 1/2), (1, 1/2, 1/2)$	$r_{fcc} = 2\sqrt{3}\pi$
a15	$N_x = 64$ $N_y = 64$ $N_z = 64$	$l_x = 2\sqrt{5}\pi$ $l_y = 2\sqrt{5}\pi$ $l_z = 2\sqrt{5}\pi$	$(1/2, 1/2, 1/2), (0, 0, 0),$ $(1, 0, 0), (0, 1, 0),$ $(0, 0, 1), (1, 1, 0),$ $(1, 0, 1), (0, 1, 1),$ $(1, 1, 1), (0, 1/2, 1/4),$ $(0, 1/2, 3/4), (1, 1/2, 1/4),$ $(1, 1/2, 3/4), (1/2, 1/4, 0),$ $(1/2, 3/4, 0), (1/2, 1/4, 1),$ $(1/2, 3/4, 1), (1/4, 0, 1/2),$ $(3/4, 0, 1/2), (1/4, 1, 1/2),$ $(3/4, 1, 1/2)$	$r_{a15} = \sqrt{5}\pi$

σ	$N_x = 128$ $N_y = 128$ $N_z = 64$	$l_x = 9\pi$ $l_y = 9\pi$ $l_z = 9\pi/2$	$(1/2, 1/2, 1/2), (0, 0, 0),$ $(1, 0, 0), (0, 1, 0),$ $(0, 0, 1), (1, 1, 0),$ $(1, 0, 1), (0, 1, 1),$ $(1, 1, 1),$ $(0.3684, 0.9632, 1/2),$ $(0.9632, 0.3684, 1/2),$ $(0.0368, 0.6316, 1/2),$ $(0.6316, 0.0368, 1/2),$ $(0.1019, 0.8981, 1/2),$ $(0.8981, 0.1019, 1/2),$ $(0.5653, 0.7624, 1/2),$ $(0.7624, 0.5653, 1/2),$	$r_\sigma = 9\pi/4$
----------	--	--	--	---------------------

			<p>(0.2376, 0.4347, 1/2), (0.4347, 0.2376, 1/2) (0.5368, 0.8684, 0), (0.8684, 0.5368, 0), (0.5368, 0.8684, 1), (0.8684, 0.5368, 1), (0.1316, 0.4632, 0), (0.4632, 0.1316, 0), (0.1316, 0.4632, 1), (0.4632, 0.1316, 1), (0.0653, 0.7376, 0), (0.7376, 0.0653, 0), (0.0653, 0.7376, 1), (0.7376, 0.0653, 1), (0.2624, 0.9347, 0), (0.9347, 0.2624, 0), (0.2624, 0.9347, 1), (0.9347, 0.2624, 1) (0.3981, 0.3981, 0), (0.6019, 0.6019, 0), (0.3981, 0.3981, 1), (0.6019, 0.6019, 1), (0.3177, 0.6823, 0.2476), (0.6823, 0.3177, 0.2476), (0.3177, 0.6823, 0.7524), (0.6823, 0.3177, 0.7524), (0.1823, 0.1823, 0.2524), (0.8177, 0.8177, 0.2524), (0.1823, 0.1823, 0.7476), (0.8177, 0.8177, 0.7476)</p>	
--	--	--	--	--

c14	$N_x = 64$ $N_y = 128$ $N_z = 128$	$l_x = 5\pi$ $l_y = 5\sqrt{3}\pi$ $l_z = 8\pi$	$(1/2, 1/2, 1/2), (0, 0, 0),$ $(1, 0, 0), (0, 1, 0),$ $(0, 0, 1), (1, 1, 0),$ $(1, 0, 1), (0, 1, 1),$ $(1, 1, 1), (1/2, 1/2, 0),$ $(1/2, 1/2, 1), (0, 0, 1/2),$ $(0, 1, 1/2), (1, 0, 1/2),$ $(1, 1, 1/2),$ $(0, 0.1695, 3/4),$ $(1, 0.1695, 3/4),$ $(0, 0.8305, 1/4),$ $(1, 0.8305, 1/4)$ $(0, 1/3, 1/16),$ $(1, 1/3, 1/16),$ $(0, 1/3, 7/16),$ $(1, 1/3, 7/16),$ $(0, 2/3, 9/16),$ $(1, 2/3, 9/16),$ $(0, 2/3, 15/16),$ $(1, 2/3, 15/16),$ $(1/2, 1/6, 9/16),$ $(1/2, 1/6, 0.938),$ $(1/2, 5/6, 1/16),$ $(1/2, 5/6, 7/16),$ $(1/2, 0.3305, 1/4),$ $(1/2, 0.6695, 3/4),$ $(0.25425, 0.08475, 1/4),$ $(0.74575, 0.08475, 1/4),$ $(0.25425, 0.91525, 3/4),$ $(0.74575, 0.91525, 3/4)$	$r_{c14} = 5\pi/2$
-----	--	--	--	--------------------

			(0.24575, 0.41525, 3/4), (0.75425, 0.41525, 3/4), (0.24525, 0.58475, 1/4), (0.75425, 0.58475, 1/4)	
c15	$N_x = 64$ $N_y = 64$ $N_z = 64$	$l_x = 20$ $l_y = 20$ $l_z = 20$	(0, 0, 0), (1, 0, 0), (0, 1, 0), (0, 0, 1), (1, 1, 0), (1, 0, 1), (0, 1, 1), (1, 1, 1), (0, 1/2, 1/2), (1, 1/2, 1/2), (1/2, 0, 1/2), (1/2, 1, 1/2), (1/2, 1/2, 0), (1/2, 1/2, 1), (1/4, 1/4, 1/4), (1/4, 3/4, 3/4), (3/4, 1/4, 3/4), (3/4, 3/4, 1/4), (1/8, 1/8, 5/8), (1/8, 3/8, 7/8), (1/8, 5/8, 1/8), (1/8, 7/8, 3/8), (3/8, 1/8, 7/8), (3/8, 3/8, 5/8), (3/8, 5/8, 3/8), (3/8, 7/8, 1/8), (5/8, 1/8, 1/8), (5/8, 3/8, 3/8), (5/8, 5/8, 5/8), (5/8, 7/8, 7/8), (7/8, 1/8, 3/8), (7/8, 3/8, 1/8), (7/8, 5/8, 7/8), (7/8, 7/8, 5/8)	$r_{c15} = 5$

Table B.2: Parameters and list of coordinate points used with equation (B.3) to initialize spherical phases.

B.2 Field optimization algorithm

Here we present the details of the algorithm used to find the order-parameter field that optimizes the free energy density, equation (3.4), subject to the conservation constraint, equation (3.8). We begin with the time-evolution equation, (3.12). Fourier transforming both sides, we obtain,

$$\begin{aligned} \frac{\partial \tilde{\phi}_p(\mathbf{q})}{\partial t} &= -q^2 \int d\mathbf{x} \frac{\delta f}{\delta \phi(\mathbf{x})} e^{-i\mathbf{q}\cdot\mathbf{x}} \\ &= -q^2 \Gamma(\mathbf{q}) \tilde{\phi}(\mathbf{q}) - q^2 \mathcal{F} \left[\frac{\delta f_{local}(\phi(\mathbf{x}))}{\delta \phi(\mathbf{x})} \right], \end{aligned} \quad (\text{B.5})$$

where we use \mathcal{F} to denote the Fourier transform, i.e.,

$$\mathcal{F}[f(\mathbf{x})] \equiv \int d\mathbf{x} f(\mathbf{x}) e^{-i\mathbf{q}\cdot\mathbf{x}}, \quad (\text{B.6})$$

and $f_{local}(\phi)$ refers to the local part of the free energy density, which is the same for all models considered in this work. Define $g(\phi)$ as the functional derivative of f_{local} , given by:

$$\begin{aligned} g(\phi(\mathbf{x})) &= \frac{\delta f_{local}}{\delta \phi(\mathbf{x})} \\ &= \tau \phi(\mathbf{x}) - \frac{\gamma}{2} \phi(\mathbf{x})^2 + \frac{1}{3!} \phi(\mathbf{x})^3. \end{aligned} \quad (\text{B.7})$$

We discretize equation (B.5) into timesteps of length α using a semi-implicit scheme:

$$\frac{1}{\alpha} \left(\tilde{\phi}^{n+1} - \tilde{\phi}^n \right) = -q^2 \Gamma(\mathbf{q}) \tilde{\phi}^{n+1} - q^2 \mathcal{F}[g(\phi^n)], \quad (\text{B.8})$$

from which we obtain the following update step,

$$\tilde{\phi}^{n+1} = (1 + q^2 \alpha)^{-1} \left(\tilde{\phi}^n - q^2 \alpha \mathcal{F}[g(\phi^n)] \right). \quad (\text{B.9})$$

We could simply iterate equation (B.9) until convergence was reached, however to improve the speed of convergence we follow [64] and use a damped Nesterov acceleration technique.

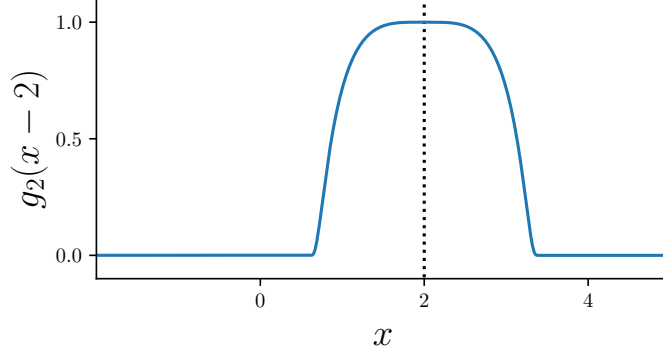


Figure B.1: Plot of $g_r(\mathbf{x} - \mathbf{x}_0)$, equation (B.4), with $r = 2$ and $x_0 = 2$.

We define a second field, $\psi(\mathbf{x})$, which is initially equal to $\phi(\mathbf{x})$. We update ϕ using the Nesterov field:

$$\tilde{\phi}^{n+1} = (1 + q^2\alpha)^{-1} \left(\tilde{\phi}^n - q^2\alpha\mathcal{F}[g(\psi^n)] \right). \quad (\text{B.10})$$

The Nesterov field is then updated using a Nesterov coefficient β^n , which is initialized to 0. The update step for ψ is:

$$\tilde{\psi}^{n+1}(\mathbf{q}) = (1 + \beta^n)\tilde{\phi}^{n+1}(\mathbf{q}) - \beta^n\tilde{\phi}^n(\mathbf{q}). \quad (\text{B.11})$$

The Nesterov coefficient is also updated using a series that approaches 1 as n gets large:

$$\beta^{n+1} = \frac{\theta^n(1 - \theta^n)}{(\theta^n)^2 + \theta^{n+1}}, \quad (\text{B.12})$$

where,

$$\theta^{n+1} = -\frac{1}{2}(\theta^n)^2 + \sqrt{\frac{1}{4}(\theta^n)^4 + (\theta^n)^2}, \quad (\text{B.13})$$

and $\beta^0 = 0$, $\theta^0 = 1$. The Nesterov acceleration technique can produce fluctuations in the solution, to avoid this we implement a simple restart - setting $\theta^{n+1} = 1$, and $\beta^{n+1} = 0$ if the free energy ever increases. Table B.3 contains a summary of the field optimization technique.

Field optimization algorithm
<ol style="list-style-type: none"> 1. Start with an initial field $\phi^0(\mathbf{x})$ and its Fourier transform $\tilde{\phi}^0(\mathbf{q})$. The initial Nesterov field is given by $\tilde{\psi}^0 = \tilde{\phi}^0$. 2. Use the Nesterov field to compute the derivative of the local free energy density, $g(\psi^n)$, using equation (B.7). Find its Fourier transform, $\mathcal{F}[g(\psi^n)]$. 3. Update the order parameter field using equation (B.10). 4. Update the Nesterov field using equation (B.11) and then update the Nesterov coefficients using equations (B.12) and (B.13) and the restart condition. 5. Compute the inverse Fourier transform of the Nesterov field. 6. Iterate steps 2 to 5 until the change in the free energy density over successive iterations is below the threshold error tolerance (10^{-7} for this work).

Table B.3: Summary of the algorithm used to find the optimal order parameter field ϕ_p for phase p .

B.3 Unit cell optimization algorithm

In this section we describe how a conjugate gradient method is used to find the optimal unit cell dimensions. More details about the conjugate gradient method can be found in reference [65]. Here we simply describe the specific algorithm used in this work. Define the vector $\mathbf{b} = (b_x, b_y, b_z)^T$. In a regular gradient descent method, we would compute the solution \mathbf{b}^* to equation (3.18) by iterating:

$$\mathbf{b}^{n+1} = \mathbf{b}^n + \alpha \mathbf{r}^n, \tag{B.14}$$

where \mathbf{r}^n is the residual vector (so called because of equation (B.14)):

$$\mathbf{r}^n = -\frac{\partial f_{nl}}{\partial \mathbf{b}^n}, \quad (\text{B.15})$$

and α is the timestep. In the conjugate gradient method, the update step is instead replaced with,

$$\mathbf{b}^{n+1} = \mathbf{b}^n + \alpha \mathbf{s}^n, \quad (\text{B.16})$$

where \mathbf{s}^n is a linear combination of the last two residual vectors:

$$\mathbf{s}^n = \mathbf{r}^n + \beta^n \mathbf{r}^{n-1}, \quad (\text{B.17})$$

and β^n is called the conjugate coefficient. It is initialized to 0 and then updated using the Fletcher-Reeves formula:

$$\beta^n = \left(\frac{r^n}{r^{n-1}} \right)^2, \quad (\text{B.18})$$

with $r = |\mathbf{r}|$. If the free energy of the system ever increases then we reset the conjugate coefficient to 0. In this algorithm we also use an *adaptive* time step, $\alpha \rightarrow \alpha^n$ in equation (B.16). We start with some initial guess α^n . We then find \mathbf{b}^{n+1} using equation (B.16) and compute the change in the non-local part of the free-energy. We accept our value of α^n if the following inequality holds:

$$f_{nl}(\mathbf{b}^{n+1}) - f_{nl}(\mathbf{b}^n) \geq c \alpha^n r^n, \quad (\text{B.19})$$

where c is some constant value chosen at the start. If the inequality does not hold then α^n is shrunk by some factor ρ ($\alpha^n \rightarrow \rho \alpha^n$) and the process is repeated. This algorithm is summarized in table B.4. The full unit cell optimization algorithm is described in table B.5.

Timestep update algorithm
<ol style="list-style-type: none"> 1. Start with constants c and ρ ($c = 0.1$ and $\rho = 0.9$ in this work), some minimum value α_{min}, and some initial guess α^n (in this work, $\alpha^n = 1$). 2. Compute \mathbf{b}^{n+1} using equation (B.16). 3. If the inequality in equation (B.19) is satisfied, or if $\alpha^n < \alpha_{min}$ then stop and return $\min(\alpha^n, \alpha_{min})$. 4. If neither condition is satisfied, then take $\alpha^n \rightarrow \rho\alpha^n$ and repeat steps 2 and 3.

Table B.4: Summary of the algorithm used to find the timestep α^n used in equation (B.16).

Unit cell optimization algorithm
<ol style="list-style-type: none"> 1. Start with some \mathbf{b}^n. Compute the residual \mathbf{r}^n using equation (B.15) with the components of $\partial f_{nl}/\partial \mathbf{b}^n$ given in equation (3.1.3). 2. Compute the conjugate vector \mathbf{s}^n using equation (B.17), where the coefficient β^n computed using equation (B.18) (Note $\beta^0 = 0$). 3. Find the timestep, α^n using the algorithm described in table B.4. 4. Find \mathbf{b}^{n+1} using equation (B.16). 5. Repeat steps 1 through 4 until the change in the non-local free energy density is smaller than the threshold error tolerance (10^{-7} in this work).

Table B.5: Summary of the algorithm used to find the optimal unit cell sizes $\mathbf{b} = (b_x, b_y, b_z)^T$.

Bibliography

- [1] R. A. L. Jones. *Soft condensed matter*, volume 6. Oxford University Press, 2002.
- [2] D. Frenkel. Soft condensed matter. *Physica A: statistical mechanics and its applications*, 313(1-2):1–31, 2002.
- [3] M. Seul and D. Andelman. Domain shapes and patterns: the phenomenology of modulated phases. *Science*, 267(5197):476–483, 1995.
- [4] J. Wang C. Hsu L. Wang M. Huang, K. Yue and S. Cheng. Frank-kasper and related quasicrystal spherical phases in macromolecules. *Science China Chemistry*, 61(1):33–45, 2018.
- [5] A. Arora F. Bates K. Dorfman A. Reddy, M. B. Buckley and G. Grason. Stable frank–kasper phases of self-assembled, soft matter spheres. *Proceedings of the National Academy of Sciences*, 115(41):10233–10238, 2018.
- [6] C. F. Gauß. Besprechung des buchs von la seeber: Untersuchungen uber die eigenschaften der positiven ternaren quadratischen formen usw. *Gotttingensche Gelehrte Anzeigen*, 2:188–196, 1876.
- [7] J. Kepler. Vom sechseckigen schnee (strena seu de nive sexangula, published in 1611), translation with introduction and notes by dorothea goetz. *Ostwalds Klassiker der exakten Wissenschaften*, 273.
- [8] T. C. Hales. The kepler conjecture. *arXiv preprint math.MG/9811078*, 1998.
- [9] V. Baranau and U. Tallarek. Random-close packing limits for monodisperse and polydisperse hard spheres. *Soft Matter*, 10(21):3826–3841, 2014.

- [10] J. Percus, editor. *The many body problem*. Wiley Interscience, 1963.
- [11] B. J. Alder and T. E. Wainwright. Phase transition for a hard sphere system. *The Journal of chemical physics*, 27(5):1208–1209, 1957.
- [12] W. W. Wood and J. D. Jacobson. Preliminary results from a recalculation of the monte carlo equation of state of hard spheres. *The Journal of Chemical Physics*, 27(5):1207–1208, 1957.
- [13] P. N. Pusey and W. Van Megen. Phase behaviour of concentrated suspensions of nearly hard colloidal spheres. *Nature*, 320(6060):340–342, 1986.
- [14] S.-C. Mau R. G. Bolhuis, D. M. S. C. Frenkel and D. A. Huse. Entropy difference between crystal phases. *Nature*, 388(6639):235–236, 1997.
- [15] B. J. Ackerson. When order is disordered. *Nature*, 365(6441):11–12, 1993.
- [16] D. Frenkel. Order through disorder: entropy strikes back. *Physics world*, 6(2):24, 1993.
- [17] F. C. Frank. Supercooling of liquids. *Proceedings of the Royal Society of London. Series A. Mathematical and Physical Sciences*, 215(1120):43–46, 1952.
- [18] F. C. Frank and J. S. Kasper. Complex alloy structures regarded as sphere packings. i. definitions and basic principles. *Acta Crystallographica*, 11(3):184–190, 1958.
- [19] F. C. Frank and J. S. Kasper. Complex alloy structures regarded as sphere packings. ii. analysis and classification of representative structures. *Acta Crystallographica*, 12(7):483–499, 1959.
- [20] D. P. Shoemaker and C. B. Shoemaker. Concerning the relative numbers of atomic coordination types in tetrahedrally close packed metal structures. *Acta Crystallographica Section B: Structural Science*, 42(1):3–11, 1986.
- [21] M. De Graef and M. E. McHenry. *Structure of materials: an introduction to crystallography, diffraction and symmetry*. Cambridge University Press, 2012.
- [22] J. A. P. Plateau. *Statique expérimentale et théorique des liquides soumis aux seules forces moléculaires*, volume 2. Gauthier-Villars, 1873.

- [23] W. Thomson. Lxiii. on the division of space with minimum partitional area. *The London, Edinburgh, and Dublin Philosophical Magazine and Journal of Science*, 24(151):503–514, 1887.
- [24] D. Weaire and R. Phelan. A counter-example to kelvin’s conjecture on minimal surfaces. *Philosophical Magazine Letters*, 69(2):107–110, 1994.
- [25] V. S. K. Balagurusamy, G. Ungar, V. Percec, and G. Johansson. Rational design of the first spherical supramolecular dendrimers self-organized in a novel thermotropic cubic liquid-crystalline phase and the determination of their shape by x-ray analysis. *Journal of the American Chemical Society*, 119(7):1539–1555, 1997.
- [26] Y. Liu V. Percec A. E. Dulcey X Zeng, G. Ungar and J. K. Hobbs. Supramolecular dendritic liquid quasicrystals. *Nature*, 428(6979):157–160, 2004.
- [27] M. J. Bluemle S. Lee and F. S. Bates. Discovery of a frank-kasper σ phase in sphere-forming block copolymer melts. *Science*, 330(6002):349–353, 2010.
- [28] J. Zhang S. Lee A. Arora K. D. Dorfman K. T. Delaney G. H. Fredrickson S. Chanpuriya, K. Kim and F. S. Bates. Cornucopia of nanoscale ordered phases in sphere-forming tetrablock terpolymers. *ACS nano*, 10(5):4961–4972, 2016.
- [29] C. Leighton S. Lee and F. S. Bates. Sphericity and symmetry breaking in the formation of frank–kasper phases from one component materials. *Proceedings of the National Academy of Sciences*, 111(50):17723–17731, 2014.
- [30] A. Arora R. M. Lewis M. A. Hillmyer K. D. Dorfman K. Kim, M. W. Schulze and F. S. Bates. Thermal processing of diblock copolymer melts mimics metallurgy. *Science*, 356(6337):520–523, 2017.
- [31] J. H. Lettow R. J. Hickey T. M. Gillard M. A. Hillmyer M. W. Schulze, R. M. Lewis III and F. S. Bates. Conformational asymmetry and quasicrystal approximants in linear diblock copolymers. *Physical review letters*, 118(20):207801, 2017.
- [32] S. M. Gruner B.-K. Cho, A. Jain and U. Wiesner. Mesophase structure-mechanical and ionic transport correlations in extended amphiphilic dendrons. *Science*, 305(5690):1598–1601, 2004.

- [33] J. Wang S. Mei X. Dong Y. Li M. Li H. Liu W. Zhang T. Aida et. al. M. Huang, C.-H. Hsu. Selective assemblies of giant tetrahedra via precisely controlled positional interactions. *Science*, 348(6233):424–428, 2015.
- [34] R. L. Marson J. He J. Huang Z. Zhou J. Wang C. Liu X. Yan K. Wu et. al. K. Yue, M. Huang. Geometry induced sequence of nanoscale frank–kasper and quasicrystal mesophases in giant surfactants. *Proceedings of the National Academy of Sciences*, 113(50):14195–14200, 2016.
- [35] J.-F. Sadoc S. Hajiw, B. Pansu. Evidence for a c14 frank–kasper phase in one-size gold nanoparticle superlattices. *ACS Nano*, 9(8):8116–8121, 2015.
- [36] A. Yethiraj S. A. Kim, K.-J. Jeong and M. K. Mahanthappa. Low-symmetry sphere packings of simple surfactant micelles induced by ionic sphericity. *Proceedings of the National Academy of Sciences*, 114(16):4072–4077, 2017.
- [37] C. M. Baez-Cotto and M. K. Mahanthappa. Micellar mimicry of intermetallic c14 and c15 laves phases by aqueous lyotropic self-assembly. *ACS nano*, 12(4):3226–3234, 2018.
- [38] A.-C. Shi. Frustration in block copolymer assemblies. *Journal of Physics: Condensed Matter*, 2021.
- [39] W. Li F. Qiu M. Liu, Y. Qiang and A.-C. Shi. Stabilizing the frank-kasper phases via binary blends of ab diblock copolymers. *ACS Macro Letters*, 5(10):1167–1171, 2016.
- [40] K. D. Dorfman. Frank–kasper phases in block polymers. *Macromolecules*, 2021.
- [41] P. D. Olmsted and S. T. Milner. Strong-segregation theory of bicontinuous phases in block copolymers. *Physical review letters*, 72(6):936, 1994.
- [42] P. D. Olmsted and S. T. Milner. Strong segregation theory of bicontinuous phases in block copolymers. *Macromolecules*, 31(12):4011–4022, 1998.
- [43] N. Xie, W. Li, F. Qiu, and A.-C. Shi. σ phase formed in conformationally asymmetric ab-type block copolymers. *ACS Macro Letters*, 3(9):906–910, 2014.
- [44] L. D. Landau. On the theory of phase transitions. i. *Zh. Eksp. Teor. Fiz.*, 11:19, 1937.
- [45] L. D. Landau. On the theory of phase transitions. ii. *Zh. Eksp. Teor. Fiz.*, 11:627, 1937.

- [46] S. A. Brazovskii. Phase transition of an isotropic system to a nonuniform state. *Soviet Journal of Experimental and Theoretical Physics*, 41:85, 1975.
- [47] S. Alexander and J. McTague. Should all crystals be bcc? Landau theory of solidification and crystal nucleation. *Physical Review Letters*, 41(10):702, 1978.
- [48] L. Leibler. Theory of microphase separation in block copolymers. *Macromolecules*, 13(6):1602–1617, 1980.
- [49] G. H. Fredrickson and E. Helfand. Fluctuation effects in the theory of microphase separation in block copolymers. *The Journal of chemical physics*, 87(1):697–705, 1987.
- [50] T. Ohta and K. Kawasaki. Equilibrium morphology of block copolymer melts. *Macromolecules*, 19(10):2621–2632, 1986.
- [51] V. V. Lebedev, E. I. Kats and A. R. Muratov. Weak crystallization theory. *Physics reports*, 228(1-2):1–91, 1993.
- [52] J. Pekalski, A. Ciach and W. T. Gózdź. Origin of similarity of phase diagrams in amphiphilic and colloidal systems with competing interactions. *Soft Matter*, 9(27):6301–6308, 2013.
- [53] D. McClenegan. Landau theory of complex ordered phases. Master’s thesis, Hamilton, ON, 2019.
- [54] S. U. Egelhaaf, H. Sedgwick and W. C. K. Poon. Clusters and gels in systems of sticky particles. *Journal of Physics: Condensed Matter*, 16(42):S4913, 2004.
- [55] R. Sanchez and P. Bartlett. Equilibrium cluster formation and gelation. *Journal of Physics: Condensed Matter*, 17(45):S3551, 2005.
- [56] J. S. van Duijneveldt, A. I. Campbell, V. J. Anderson and P. Bartlett. Dynamical arrest in attractive colloids: The effect of long-range repulsion. *Physical review letters*, 94(20):208301, 2005.
- [57] S. Sennato, F. Bordi, C. Cametti and M. Diociaiuti. Direct evidence of multicompartment aggregates in polyelectrolyte-charged liposome complexes. *Biophysical journal*, 91(4):1513–1520, 2006.

- [58] D. Pini and A. Parola. Pattern formation and self-assembly driven by competing interactions. *Soft Matter*, 13(48):9259–9272, 2017.
- [59] Y. Zhuang and P. Charbonneau. Recent advances in the theory and simulation of model colloidal microphase formers. *The Journal of Physical Chemistry B*, 120(32):7775–7782, 2016.
- [60] C. Burns J. Xie and A.-C. Shi. Complex spherical packing phases formed in hard sphere cluster crystals. unpublished, 2021.
- [61] S. M. Barbon R. M. Lewis M K. T. Delaney A. Anastasaki J. C. Hawker G. H. Fredrickson M. W. Bates, J. Lequeieu and C. M. Bates. Stability of the a15 phase in diblock copolymer melts. *Proceedings of the National Academy of Sciences*, 116(27):13194–13199, 2019.
- [62] T. Kawakatsu. *Statistical physics of polymers: an introduction*. Springer, 2004.
- [63] J.-P. Hansen and I. R. McDonald. *Theory of simple liquids*. Elsevier, 1990.
- [64] W. Si K. Jiang and C. Bao. An efficient method for computing stationary states of phase field crystal models. *arXiv preprint arXiv:1909.00305*, 2019.
- [65] W. W. Hager and H. Zhang. A survey of nonlinear conjugate gradient methods. *Pacific journal of Optimization*, 2(1):35–58, 2006.
- [66] M. Rubenstein and R. H. Colby. *Polymer physics*. Oxford University Press, 2003.